CurateND

UNIVERSITY OF NOTRE DAME | HESBURGH LIBRARIES

Multi-Scale Modeling for Ionic Liquid Enabled Separation Systems

Alejandro Garciadiego Del Rio

Publication Date

02-08-2022

License

This work is made available under a All Rights Reserved license and should only be used in accordance with that license.

Citation for this work (American Psychological Association 7th edition)

Garciadiego Del Rio, A. (2022). *Multi-Scale Modeling for Ionic Liquid Enabled Separation Systems* (Version 1). University of Notre Dame. https://doi.org/10.7274/1j92g735c2d

This work was downloaded from CurateND, the University of Notre Dame's institutional repository.

For more information about this work, to report or an issue, or to preserve and share your original work, please contact the CurateND team for assistance at curate@nd.edu.

MULTI-SCALE MODELING FOR IONIC LIQUID ENABLED SEPARATION SYSTEMS

A Dissertation

Submitted to the Graduate School
of the University of Notre Dame
in Partial Fulfillment of the Requirements
for the Degree of

Doctor of Philosophy

by

Alejandro Garciadiego Del Rio

Alexander W. Dowling, Director

Graduate Program in Chemical and Biomolecular Engineering
Notre Dame, Indiana

August 2022

MULTI-SCALE MODELING FOR IONIC LIQUID ENABLED SEPARATION SYSTEMS

Abstract

by

Alejandro Garciadiego Del Rio

Humanity's energy consumption is enormous, accompanied by high costs and CO_2 emissions. Separation processes account for 45-55% of industrial energy consumption in the United States. There exists ample opportunity for reducing and replacing high-energy separation processes with innovative separation agents. This thesis explores methods to aid the search for novel materials integrating data science and process systems engineering tools to find property targets for separation agents and contemplate which data is more valuable to screen these separation agents. Two frameworks are proposed in this thesis:

1. Molecular design targets and optimization framework of low-temperature thermal desalination systems. The framework focuses on finding molecular design targets for directional solvents for water desalination.
2. Measuring what data are most valuable to screen ionic liquid entrainers for extractive distillation. The framework focuses on screening ILs as entrainers for separating high Global Warming Potential (GWP) mixtures of hydrofluorocarbons (HFCs).

Multi-scale optimization frameworks are proposed to facilitate and accelerate solvent discovery. Using molecular-systems engineering, the proposed frameworks aim to identify properties that significantly influence the cost of the separation process. Once the impactful properties are identified, the framework can be used to study

which data is more valuable for multi-scale modeling and what accuracy in the data is necessary for entrainer screening. Finally, an added value metric is included to understand the economics of a separation process.

CONTENTS

FIGURES

TABLES

SYMBOLS

Sets and Elements

$\mathcal{C}$	Components
D	Data sets
$d \in \mathcal{C}$	Directional solvent
$s \in \mathcal{C}$	Salt
$w \in \mathcal{C}$	Water
$\mathcal{G}$	Functional Groups
$CH_2 \in \mathcal{G}$	CH_2 functional group
$CH_3 \in \mathcal{G}$	CH_3 functional group
$COOH \in \mathcal{G}$	Carboxylic acid functional group
$H_2O \in \mathcal{G}$	Water
$\mathcal{N}$	Fatty Acid Directional Solvents
$6 \in \mathcal{N}$	Hexanoic acid
$7 \in \mathcal{N}$	Heptanoic acid
$8 \in \mathcal{N}$	Octanoic acid
$9 \in \mathcal{N}$	Nonanoic acid
$10 \in \mathcal{N}$	Decanoic acid
$\mathcal{S}$	Streams in Process (See Figure 2.1 for stream numbers)
$\mathcal{I} \subset \mathcal{S}$	Inlet streams (for a specific unit operation)
$\mathcal{O} \subset \mathcal{S}$	Outlet streams (for a specific unit operation)
$\mathcal{P} \subset \mathcal{S}$	Pinch candidates
$\mathcal{S}_\mathcal{C} \subset \mathcal{P}$	Cold streams

$\mathcal{S}_{\mathcal{H}} \subset \mathcal{P}$	Hot streams

Indices

$i, j \in \mathcal{C}$	Component
$d \in D$	Data set
$k \in \mathcal{G}$	Functional group
$in \in \mathcal{I}$	Equipment inlet stream
$l, out \in \mathcal{O}$	Equipment outlet stream
liq	Liquid phase
$N_c \in \mathcal{N}$	Number of carbon atoms in fatty acid DS
$o_1 \in \mathcal{O}$	Solvent phase
$o_2 \in \mathcal{O}$	Aqueous/salty phase
vap	Vapor phase

Variables

$\alpha_{i,j}$	Volatility of component i relative to component j
A	Solubility of the solvent in water at a reference temperature
a_m	a unlike-interaction parameter
B	Thermoresponsiveness of the solubility of the solvent
b_m	b unlike-interaction parameter
C_{anm}	Annualized capital cost \$/year
C_p	Heat capacity (J/mol-K)
CRF	Capital recovery factor
F	Molar flow (kmol/s)
i	Real discount rate
P	Pressure (MPa)
$\hat{P}$	Calculated obtained pressure (MPa)

$\Phi_{phase,i}$	Fugacity of component i
Q	heat duty in the heat exchanger (kW)
QA_C^p	heat content bellow pinch temperature (kW)
QA_H^p	heat content above pinch temperature (kW)
Q_S	Heat from hot utility (kW)
Q_W	Heat from cold utility (kW)
T	Temperature (K)
T_1	Intermediate temperature variable (K)
T_{bubble}	Bubble temperature (K)
T_{eq}	Equilibrium temperature (K)
T_{dew}	Dew temperature (K)
T^p	Pinch candidate temperature (K)
V	Volume
x	Liquid molar composition
y	Vapor molar composition

Parameters

a	Attraction between molecules
b	Volume occupied by molecules
κ	Binary interaction parameter
κ_d	Solubility of DS in the aq. phase (mol/mol)
κ_s	Solubility of salt in the solvent phase (mol/mol)
ΔT_{min}	Heat recovery approach temperature (K)
C_{NPC}	Net present cost
ϵ_1	Smoothing parameter 1
ϵ_2	Smoothing parameter 2
f	Expected inflation rate

i'	Nominal discount rate
N_C	Number of carbon atoms
N_k	Number of functional groups
P_c	Critical pressure (MPa)
R	Ideal gas constant
T_c	Critical temperature (K)
T_{max}	Maximum allowable temperature of the process (°C)
T_{min}	Minimum allowable temperature of the process (°C)

Abbreviations

CRF	Capital Recovery Factor
DS	Directional Solvent
DSE	Directional Solvent Extraction
EoS	Equation of State
EPA	Enviromental Protection Agency
GWP	Global Warming Potential
HFC	Hydrofluorocarbon
IDAES	Institute for the Design of Advanced Energy Systems
IL	Ionic Liquid
LCOW	Levelized Cost of Water
MED	Multi-Effect Distillation
MAPE	Mean absolute percentage error
MSF	Multi-Stage Flash
MVC	Mechanical Vapor Compression
RO	Reverse Osmosis
OARO	Osmotically Assisted Reverse Osmosis
TDS	Total Dissolved Solids

VLE Vapor-Liquid Equilibrium

ACKNOWLEDGMENTS

I would like to start by thanking my advisor Prof. Alexander Dowling. His guidance, input, and patience have been invaluable these past five years. He has pushed me to be a better researcher and a better mentor. I would also like to thank the members of my thesis committee, Prof. Edward Maginn, Prof. Tengfei Luo, and Prof. Jeffrey Kantor, for their insights, advice, and time, as collaborators and instructors, were critical to the completion of this thesis.

I want to acknowledge collaborators who helped with my work. The work shown in Chapter 3 and Chapter 4 was made in collaboration which Bridgette Befort, Mozammel Mazumder, Gabriela Franco, and Tipton Lichtenstein. The CISTAR and open-source software development was made in collaboration with Kanishka Ghosh, Samuel De La Paz, and Caroline Lubbe.

I would also like to acknowledge the members of the Dowling Lab and especially Dr. Elvis Eugene, Xian Gao, Kanishka Ghosh, Bridgette Befort and Jialu Wang, for invaluable for their valuable insights and their friendship, as well as Dr. Jerry Crum and Dr. Justin Easa as their frienship was a huge pillar in my time as a graduate student.

I would like to thank my parents for their unconditional support and for teaching me how important education is in one's life. As well as my sister for all the love and care she has given me. I want to thank my extended family and friends back home for their friendship, love, and support. Finally, I want to help Santiago De Carcer, as a mutual promise pushed me to graduate school.

Finally, I would like to acknowledge the funding of the University of Notre Dame

and the U.S. National Science Foundation under grant CBET-1917474.

CHAPTER 1

INTRODUCTION

1.1 Society Needs Inexpensive Sustainable Separation

Growing human population and industrialization have caused increased greenhouse gas atmospheric concentrations[126], global temperature increase[136] and water scarcity for over 50% of the world population[78]. Separation proceses demands account for 45-55% of all industrial energy requirements in the U.S.[135]. The solution to such problems relies on viable separation processes such as CO_2 capture, high GWP mixture separation, water decontamination, and desalination, to name a few. However, separation processes, in general, are energy-intensive, and they account for 10-15% of the energy consumed in the world[135]. There exists ample opportunity for reducing and replacing high-energy separation processes with innovative separation agents and sustainable technologies[107].

Developing new separation solvents is crucial to reducing the energy intensity and environmental footprint of modern society. This thesis studies two separation methods that require new separation agents. Azeotropic distillation and extraction have been assessed as technologies that can be integrated with novel materials to reduce energy intensity[107]. Extractive systems reduce energy intensity by utilizing a solvent that changes the solubilities of the mixture's components. However, the energy requirements can be dramatically impacted by the thermophysical properties of the separation agents.

1.1.1 Directional Solvent Extraction (DSE)

Directional solvent extraction is an emerging membrane-free liquid-liquid extraction process to desalinate water using low-grade heat. Several unique features make DSE a potentially disruptive desalination technology: 1) it is thermally driven and utilizes low-grade heat; 2) it does not require the use of membranes; 3) there are opportunities to intensify, modularize and customize the process; 4) there is a vast solvent molecular design space. However, the energy intensity of DSE depends entirely on the solvent. Even though carboxylic acids have been explored for the separation[18, 9], the separation's Levelized Cost of Water (LCOW) is higher than competing technologies, which requires new solvents to be explored. Chapter 2 explores the thermophysical limitations of carboxylic acids and provides a framework to analyze the properties a new solvent would require to make DSE an economically competitive technology.

1.1.2 Separation of high global warming potential HFCs

Hydrofluorocarbon (HFC) mixtures are commonly used as refrigerants. Unfortunately, some pure HFCs and HFC mixtures exhibit high global warming potentials (GWP)[50]. To reduce the impact of these mixtures, in recent years, several international and national mandates[142, 52] have sought to reduce the use of these types of refrigerants. However, some refrigerants are azeotropic or near-azeotropic. Separating these mixtures is complex and energy-intensive as the components condense and evaporate simultaneously at a constant temperature[95]. Separating azeotropic mixtures of hydrofluorocarbons (HFCs) for reuse and recycling is environmentally and economically imperative. However, an entrainer that breaks the azeotrope and reduces energy demands for the separation is necessary. Chapter 3 explores which data is most important and what data accuracy the data is needed for entrainer screening.

1.2 Ionic Liquids (IL) Are Compelling Designer Solvents

Ionic liquids are a promising group of separation agents[127]. ILs are organic salts with asymmetric size and shape of ions which weakens their mutual electrostatic interactions[150]. These weaker interactions result in lower melting points than inorganic salts and good thermal stability and extremely low volatility, allowing them to be operated at ambient conditions[115, 66]. Some ILs make for ideal separation agents, as they can change mixture solubilities, and their properties can be tailored [129, 115, 132, 27]. ILs are broadly applicable in other processes such as refrigerant separation, liquid-liquid extraction, and CO_2 capture, to name a few. Designing optimal fit-for-use ionic liquids for these separations will reduce energy intensity. However, the vast space of possibilities for molecular design space (10^6 estimated possible ionic liquids)[128] makes optimizing systems and solvents simultaneously an intensive problem.

1.3 Computer-Aided Molecular Design (CAMD) for Molecular-systems Modeling for IL

To bridge molecular and systems design, CAMD leverages the advancements in chemical and process modeling to reverse engineer molecular structure for an optimal material for a process. CAMD is a collection of tools developed over the past 30 years[14] for designing tailored molecules depending on the optimal properties for a specific application. CAMD extends process-scale optimization[26] as it can simultaneously optimize molecular composition, operating conditions, equipment design, and process topology.

CAMD requires property models to obtain solubility predictions in separation methods, heat capacities for energy requirements, and densities, among other properties. The effectiveness of CAMD depends on the suitability of the thermodynamic

model employed[123]. Most CAMD studies use group contribution methods[77] to find a combination of structural groups that satisfies a required property specification. UNIversal QUAsiChemical (UNIQUAC) Functional-group Activity Coefficients (UNIFAC) models have been used for almost two decades[77, 123, 35]. In recent years, commercial tools employed equations based on Statistical Associating Fluid Theory (SAFT)[75, 70] and COnductor like Screening Model for Real Solvents (COSMO-RS)[23]. Superstructure optimization is also used to find the combination of ions in ionic-liquid design[35] by evaluating all possible pairing of specific ions to obtain a required property.

Different CAMD tools have been utilized to design ILs for over two decades[151, 33]. These tools include characterization-based reverse design[40], using property clustering and decomposition techniques[63], and by coming Quantitative structure-property relationships (QSPRs) with structural feasibility constraints in a combinatorial optimization problem [96] solid-liquid equilibria model[117]. Additionally CAMD has been used for extractive separations such as desulfurization [137, 110] and extractive distillation of n-hexane-methylcyclopentane[32].

However, the large process design decision space and an even larger space for molecular design decisions make CAMD problems computationally challenging to solve, often even after employing model simplifications. Additionally, optimizing process design and molecules involve discrete and continuous choices, which adds complexity to the problem. Even though superstructure optimization is commonly used to mitigate the size of the problem[156, 8], the amount of possible ILs makes CAMD for ILs a complex and computationally expensive task. Additionally, the accuracy of thermophysical property predictions limits all CAMD approaches.[7]. However, CAMD in ILs has been slowed by a lack of accurate models in estimating ionic liquid properties. This problem increases in novel materials due to scarcity of data. Group contribution models require extensive data sets to parametrize interac-

tion parameters, which is not readily available.

To facilitate the use of CAMD tools for IL separation solvents in systems with data scarcity, this thesis proposes to: i) study which properties are the most important in a separation process that would reduce energy intensity and overall costs, ii) analyze which data is more important to represent the thermodynamics accurately, iii) inform experimental design on the accuracy of the data required, and iv) evaluate the added value of the separation.

1.4 Setting Molecular Design Targets for ILs

Chapter 2 establishes a technoeconomic modeling framework to simultaneously optimize and heat integrate the DSE process. Rapid bottom-up screening is performed to predict the energy intensity and levelized cost of water (LCOW) of organic acid and ionic liquid directional solvents (DS) in an optimized DSE process. Likewise, top-down analysis is performed to set continuous solvent property targets necessary to realize a LCOW of less than $\$0.5/m^3$. LCOW is most sensitive to the solubility of the DS in water and thermoresponsive ability (a.k.a., yield) of the solvent, i.e., the change in the solubility of water in the DS with temperature. Despite their lower cost, organic acids have a small thermoresponsive ability and LCOW of at least $\$1.3/m^3$. Setting modest quantitative thermophysical property targets for ionic liquid DS to achieve below $\$0.5/m^3$ LCOW.

1.5 Defining Data and Accuracy Necessary for Multi-scale Modeling and IL Screening

In Chapter 3, an open-source equation-oriented modeling framework is proposed to rapidly translate HFC/IL solubility data into regressed thermodynamic models, which can be used for process design under uncertainty and rapid IL screening. Moreover, using data science and process systems engineering tools to contemplate which

data are the most valuable for IL screening. Finding that binary solubility data collected at multiple temperatures is adequate for separation process design, and newly available ternary solubility measurements should be reserved for validation. Additionally, uncertainty quantification analyses are used to show that up to 10% experimental error is acceptable for IL screening decisions. These results recommend a multi-step workflow for IL screening.

1.6 Open-Source Software Development

In all aspects of this thesis, we strive to implement open-source software in creating the frameworks and allowing for easy extension of the framework to other separation processes. Open-source software also facilitates validation, reproducibility, and accountability of the research developed. The work in this thesis is done in the Python Optimization Modeling Objects (Pyomo) and IDAES-PSE. Pyomo is an open-source software package for modeling and solving mathematical programs[68] which supports the formulation models for complex optimization applications[31]. The Institute for the Design of Advanced Energy Systems Process Systems Engineering (IDAES-PSE) is an extensible, equation-oriented process model Python library based on Pyomo[82]. This endeavor has been achieved with several undergraduate students to encourage the use of optimization and its tools and expose students to research. These goals were:

- The work shown in Chapter 2 was originally developed in Julia. However, it has been translated into Pyomo[1] to make it more accessible and mantainable.
- To develop the work shown in the thesis, during a three month-long internship at NETL, IDAES-PSE utilities were expanded, such as bubble and dew temperature phase plotting. Furthermore, helped in testing key features of the infrastructure needed for the frameworks with an air separation and a CO_2-IL

[1] https://github.com/dowlinglab/pyomo-directional-solvents

absorption property packages[2].

- The Duran-Grossmann heat integration formulation[45] was included in order to expand the capabilities of the IDAES-PSE library[3]. This formulation locates the minimum driving force of the heat exchanger. It solves the optimization of the process and the heat integration simultaneously, anticipating in the optimization that the problem will be heat integrated, adding the flow rates, temperatures, and compositions as degrees of freedom (the detailed formulation can be found in Chapter 2 Section 2.3.3). A repository with the formulations of the heat integration network to minimize energy and pairing of heat exchangers was also created[4].
- Finally, utilizing IDAES-PSE, contributing to the National Science Foundation (NSF) Center for Innovative and Strategic Transformation of Alkane Resources (CISTAR). CISTAR works on transforming light hydrocarbons in shale gas into liquid fuels. A property package was created with the necessary equations and models to calculate the thermodynamic properties of the components of shale gas and light liquid fuels. Additionally, a packed bed reactor in IDAES-PSE was included to explore the property targets for new catalysts for transforming light hydrocarbons. These models are being used to prepare a collaborative paper and are not discussed further in this thesis.

1.7 Thesis Organization

Chapter 2 presents a technoeconomic analysis for molecular design targets and optimization of DSE. The DSE system is optimized, heat integrated simultaneously utilizing decanoic acid, and validated with data from Altoabi *et al.* [9]. Following the validation, different carboxylic acids are compared as directional solvents. Next the analysis is conducted utilizing [emim][Tf_2N]. Finally, with [emim][Tf_2N] as a benchmark, properties are set as continuous variables and find molecular design targets for future ILs.

Chapter 3 proposes an eight-step framework to screen ILs as entrainers and inform experimental design over experimental conditions and data accuracy. HFC-

[2]https://github.com/IDAES/examples-pse/pull/27

[3]https://github.com/IDAES/idaes-pse/pull/348

[4]https://github.com/dowlinglab/heat-integration

IL solubility data is compiled and introduced in the 8-step open-source framework. Thermodynamic binary parameters are calibrated, and the quality of fit is assessed. Utilizing the binary parameters, early process design calculations are performed and screen different ILs as entrainers for separating HFC mixtures. Finally, uncertainty is propagated through the thermodynamic models and informs experiments over which data is more valuable and the necessary data accuracy.

Chapter 4 studies the economic viability of HFC separation over the present and future prices of pure HFCs and ILs. The HFC-IL separation process is simulated in Aspen Plus and performs a sensitivity analysis over seven variables in the flowsheet. Next, economic calculations of the process for five different HFC mixtures are shown. Finally, an added value of the separation metric is used to inform the required price of the HFC mixtures and pure HFC for the separation to be economically viable.

CHAPTER 2

MOLECULAR DESIGN TARGETS AND OPTIMIZATION OF LOW-TEMPERATURE THERMAL DESALINATION SYSTEMS

This chapter is based on previously published work:

A. Garciadiego, T. Luo, A. W. Dowling. Molecular design targets and optimization of low-temperature thermal desalination systems, *Desalination*, 504: 114941, 2021. doi:10.1016/j.desal.2021.114941.

2.1 Introduction

Water consumption is critical to modern society; the average American family uses approximation 1140 liters of municipal water per day [52], and 130 million Americans face severe water scarcity at least part of the year [97]. Globally, 3.8 billion people currently experience water scarcity [78], and it is estimated that 66% of the world's population could be living under water-stressed conditions by 2025 [143]. Although the costs of water obtained from desalination have fallen in the last decade, they are higher than obtaining freshwater from rivers, groundwater, or water recycling. In 2019, less than one percent of the water consumed globally was produced by desalination [146, 73, 120].

The expansion of oil and gas extraction in the US has created new water and environmental challenges [52]. In 2012, 3.57 billion m^3 of produced water was extracted in the US. In the Delaware Basin, up to 4 barrels of water are produced per barrel of oil [13]; to put this number in perspective, around 0.50 liters of produced water may

be generated to supply energy for one hour in an average American household. The salinity of produced water is typically 35,000 ppm to 300,000 ppm, which may be up to eight times higher than seawater salinity (35,000 ppm) [98]. Unfortunately, current desalination technologies are unpractical to treat such high salinity brines [47]. Large water volumes (about 20,000 m^3 on average per well) from oil and gas production also remain challenging, even after water supply chain optimization. [154, 155]. There is a pressing need and opportunity for new technologies to treat produced water.

There is no one-size-fits-all technology for water treatment, including desalination. Instead, there is a growing emphasis on fit-for-purpose treatment in decentralized networks [166]. In this paradigm, water is treated to only the specifications needed for specific end uses. Table 2.1 highlights different water quality levels (salinity), appropriate end uses, and candidate desalination technologies. While evaporative and reverse osmosis desalination technologies are commonly deployed, they remain energy-intensive and unable to treat high salinity water sources. In the context of fit-for-purpose water, there is a great need for new technologies to treat a wide range of water quality levels in distributed networks while using renewable energy.

TABLE 2.1

NATURAL AND MAN MADE SOURCES OF WATER RANGE FROM FRESHWATER TO BRINY WATER[52].

Water classification	Salinity (weight%)	Salinity (ppm)	Use	MSF	MED	RO	DSE
Freshwater	0-0.10%	0-1,000	Human consumption, livestock and irrigation	✓	✓	✓	✓
Slightly saline water	0.10-0.16%	1,000-1,600	Livestock, may require special treatment for irrigation	✓	✓	✓	✓
	0.16-0.30%	1,600-3,000	Poultry and pigs	✓	✓	✓	✓
Moderately saline water	0.30-1.00%	3,000-10,000	Suitable for cattle or sheep and for flushing toilets	✓	✓	✓	✓
Very saline water	1.00-3.50%	10,000-35,000	Industrial usage(2%), thermoelectric power plants (95%)	✗	✗	✓ (partially)	✓
Briny water	>3.50%	>35,000	and mining (3%)	✗	✗	✗	✓

Salinity requirements vary widely depending on end use. For example, low salinity water is used for human and livestock consumption. But high salinity water with more than 35,000 ppm is suitable for industrial uses including power plant cooling and mining. While well-established technologies including Multi-stage Flash (MSF), Multi-effect Desalination (MED) and Reverse Osmosis (RO) have greatly advanced desalination industry [72], there remains a need for sustainable and energy efficient process to treat high salinity water

Directional solvent extraction (DSE) uses a thermoresponsive solvent to facilitate treatment over a wide salinity range [92]. DSE does not require membranes, which often foul at high salinities, and can utilize low-grade heat, including waste or renewable (solar) sources. Prior work in DSE includes characterization of molecular phenomena, bench-scale demonstrations, and limited process analysis [17, 18, 92, 9, 91, 10]. This paper presents a technoeconomic optimization framework with two new capabilities: first, we perform simultaneous process optimization and heat integration to rapidly screen directional solvent candidates in seconds. Second, we perform a sensitivity analysis to identify the necessary solvent properties to enable cost-effective DSE processes for treating high salinity water, which is difficult/impossible to desalinate with other technologies. We emphasize these advances in process-scale models can rapidly accelerate DSE development by reducing the need for expensive experiments and guiding (computational) molecular design. To our knowledge, this is the first application of equation-oriented process optimization to facilitate bottom-up and top-down analysis of the DSE process.

The remainder of this paper is organized as follows. Section 2 reviews literature on desalination and DSE, with an emphasis on the scope for optimization. Section 3 describes the optimization framework and mathematical models. Section 4 studies the impact of heat source temperature and solvent properties on the optimized process's minimum specific energy. Section 5 presents quantitative solvent property goals to achieve \$0.50/m^3 levelized cost of water (LCOW) target for two classes of molecules: carboxylic acids and ionic liquids. Finally, Section 6 summarizes conclusions, limitations, and future work.

2.2 Literature Review

2.2.1 Desalinaton technologies

Modern desalination technologies, including evaporative and reverse osmosis systems, are energy-intensive and not suitable to treat high salinity water. Evaporative systems such as multi-stage flash (MSF) and multi-effect distillation (MED) utilize thermal energy (typically 90°C and 55°C, respectively) to evaporate and condensate water [98]. These systems require highly corrosion-resistant and costly materials [2] and are heat-intensive (26.29-83.06 kW/m^3); they require three or four times the theoretical minimum energy of separation [47, 98]. In contrast, membrane-based technologies such as reverse osmosis (RO) use mechanical work to overcome the osmotic pressure across a membrane. Membrane-based technologies use significant electricity inputs, need frequent membrane replacement, and have limited effectiveness when treating concentrated brines [47]. New technologies, including electrodialysis and forward osmosis, show promise to reduce energy consumption and lower costs. For example, osmotically assisted reverse osmosis (OARO) and mechanical vapor compression (MVC) are suitable to treat high salinity brines (140,000 ppm and 150,000 ppm respectively) [21, 20, 140]. Nevertheless, MVC energy consumption is high (single-effect MVC 23–42 kW/m^3, double-effect MVC 20 kW/m^3) [140]. OARO, RO, and other membrane-based technologies are often susceptible to membrane fouling at high salt concentrations [138]. While hybrid desalination systems paired with renewable energy sources are well-studied [90, 104, 46], there is limited work of technologies suitable for high salinity brines.

TABLE 2.2

COMPARISON OF ENERGETICS, COSTS, AND LIMITATIONS OF COMMON DESALINATION TECHNOLOGIES [98, 138]

Technology	Multi-Stage Flash (MSF)	Multi-Effect Distillation (MED)	Reverse Osmosis (RO)
Specific energy	26.29-83.06 kW/m^3	26.29-76.26 kW/m^3	3.05-8.33 kW/m^3
Thermal input temperature	90 °C	55-70 °C	ambient
Global deployment	8%	27%	60%
Cost	0.27-1.49 \$/m^3	0.80-1.50 \$/m^3	0.45-1.62 \$/m^3
Thermal energy input	High	High	Low
Electric energy input	Low	Low	High
Equipment size	Large	Large	Small
Membrane replacement or fouling	No	No	Yes

2.2.2 Directional solvent extraction

Directional solvent extraction can overcome limitations of thermal and membrane-based systems by efficiently separating high salinity feeds with low-grade waste heat (approximately 40 to 80 °C). DSE exploits thermoresponsive solvents that extract water from salty mixtures at elevated temperatures and release water (phase separate) when cooled. Directional Solvents (DS) have several features: (1) water can dissolve in the solvent, and the solubility increases with temperature; (2) the solvent is virtually insoluble in water; (3) the solvent does not dissolve salts. The DSE process, which is explained in Figure 2.1, is based on liquid-liquid extraction; the solubility of water increases in the directional solvent as temperature increases (thermoresponsiveness), which enables simple regeneration. These features give DSE several distinct advantages compared to existing technologies: (1) DSE is membrane-free and thus is not restricted by membrane fouling concerns for high salinity water; (2) DSE operates in the liquid state, which reduces the size and complexity of the equipment; (3) DSE can be paired with a low-temperature renewable heat source (e.g., low-cost thermal solar).

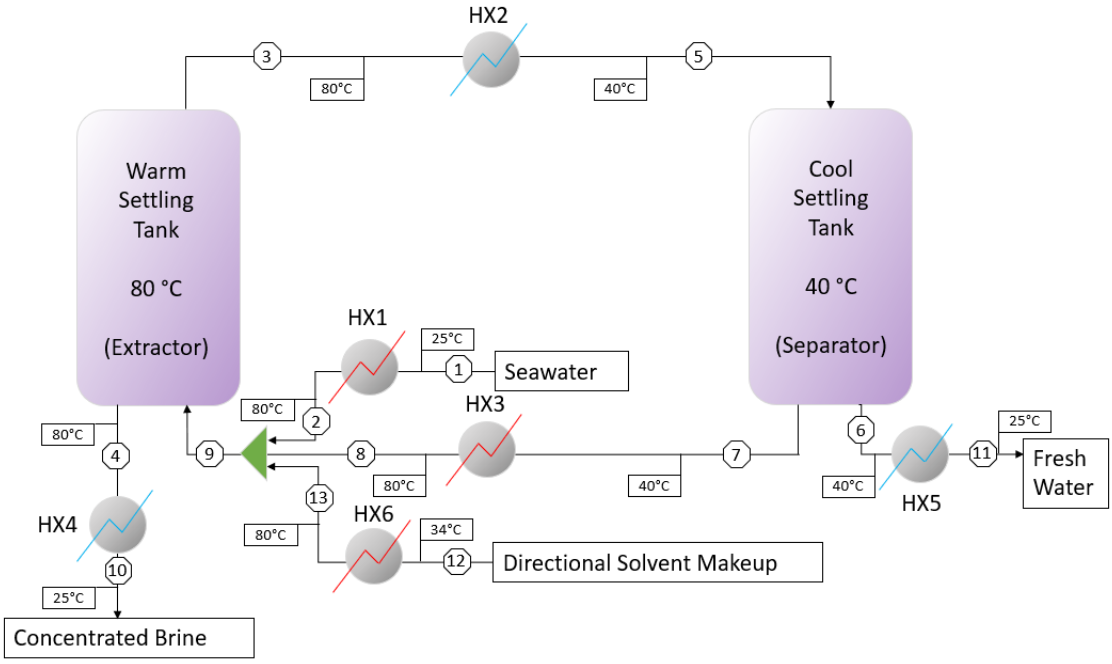

Figure 2.1. Illustration of the basic directional solvent extraction (DSE) process. Seawater (stream 1) is heated to the maximum allowable temperature (80°C is shown) in the process and mixed with the directional solvent (stream 8). The mixed emulsion of water and directional solvent (stream 9) settles in the warm settling tank. Water dissolves in the directional solvent, and concentrated brine (stream 4) is extracted from the mixture by gravity. The directional solvent and dissolved water (stream 3) are then cooled down. Freshwater is expelled from the mixture and decanted (stream 6). Decanoic acid is reheated and recycled (stream 8). A small amount of directional solvent dissolves in the freshwater and is lost (stream 6). Thus a small directional solvent make-up feed is added to the system (stream 12) to ensure steady-state operation.

Amines [39], and alcohols [71] were explored over fifty years ago as the first directional solvents for desalination. These solvents can only treat low salinity water (5000 ppm) and have a high solubility in water, leading to high solvent losses [48]. In the 1990s, The Puraq Company proposed a liquid polymers-based [80, 81] directional sol-

vent, which was commercially unsuccessful due to elevated solvent production costs [3], although recent work by Thanaplan *et al.* [139] reexamines the energetics of the Puraq Company's process. Recently, Luo and co-workers proposed fatty acids, including decanoic acid ($CH_3(CH_2)_8COOH$) and octanoic acid ($CH_3(CH_2)_6COOH$) as directional solvents. The highly polar C=0 and O−H groups in the fatty acids facilitate the formation of hydrogen bonds with water molecules, which enables carboxylic acids to dissolve water. The chain end is hydrophilic, however, the rest of the fatty acid molecule is hydrophobic, which helps ensure the solubility of the acids in water is negligible (30 - 150 ppm) [18]. In recent work, Guo *et al.* [62] proposed the use of ionic liquids, which have a greater thermoresponsivness ability compared to fatty acids. In this work, we will assess the technoeconomic potential of fatty acid and ionic liquid directional solvents in the context of an optimized DSE process.

2.2.2.1 Effectively utilize low-grade heat and no/limited membrane costs

Luo and co-workers [17, 18, 92, 9, 91, 10] recently demonstrated octanoic and decanoic acid can efficiently desalinate water. Specifically, they experimentally observed the solubility of water in decanoic acid changes from 3.8 wt% at 34°C to 5.9% at 80°C, with negligible solubility of fatty acid in water [9]. This thermoresponsive characteristic of the directional solvent enables thermal regeneration and is essential to the DSE process. Luo and co-workers then demonstrated the DSE concept in a continuous bench-scale process, successfully extracting 2.5 gallons of freshwater per day from a 700 ppm to 1100 ppm salinity feed (0.07-0.11 wt%) utilizing octanoic acid [9]. Based on these experiments, they estimated a total energy consumption of 184 kW/m^3 for decanoic acid and 101 kW/m^3 for octanoic acid, assuming heat integration with 90% heat exchanger efficiency[9].

2.2.2.2 Demonstrated performance for higher salinities

Bajpayee *et al.* [17] demonstrated the effectiveness of octanoic acid to treat salty brines from 3,667 ppm to 58,333 ppm TDS (total dissolved solids). Likewise, they successfully treated saturated brines show water extraction with DSE of brine with 290,000 ppm (NaCl) [17]. These results suggest DSE can treat produced water with high TDS from oil and gas extraction (up to 460,000 ppm).

2.2.2.3 Scope for molecular-to-systems optimization

There are vast unexplored opportunities to optimize DSE across molecular and process scales. Existing fatty solvents require approximately 90 m^3 of recycle per 1 m^3 of freshwater, which makes the processes remain energy-intensive. Alotaibi *et al.* [9] performed heat integration for a single-stage continuous process for DSE utilizing octanoic and decanoic acids using flowrates obtained from bench-scale experiments [9]. Their analysis used the transshipment heat integration model, which assumes fixed flowrates and temperatures [111]. While insightful, this analysis technique often overlooks opportunities to reduce energy intensity that are only realizable by simultaneously optimizing process conditions (flowrates, temperatures, compositions) and performing heat integration [26]. In this work, we show the benefits of more extensive process optimization. At the molecular scale, Guo *et al.* [62] recently measured the thermophysical properties of a handful of ionic liquids as candidate directional solvents. However, there are well over a billion candidate solvents to consider. In this work, we use rigorous process modeling and optimization to set quantitative solvent thermophysical property targets as a means to narrow the vast molecular design space.

2.3 Methods: Technoeconomic Optimization Framework

As a first step to realize molecular-to-system optimization of the DSE platform, we propose a computational framework for rapid bottom-up screening of candidate solvent and top-down identification of continuous solvent properties. In this section, we fully define the mathematical models and computational implementation.

2.3.1 Problem statement

Given inlet water salinity (e.g., 35,000 ppm NaCl), water rejection ratio (e.g., 50% water rejection rate, which is defined by the percentage of water that will become freshwater over the total water inlet), physical properties of the directional solvent, and a maximum temperature of the heat input, *manipulate* the temperature and material flows in the DSE process (streams in Figure 2.1) to *minimize* the specific energy of the problem. We formulate this as a nonlinear optimization problem (M1):

$$
\begin{aligned}
\min \quad & \text{Specific Thermal Energy} \\
\text{s.t.} \quad & \text{Unit Operation Models Table 2.3} \\
& \text{Embedded Heat Integration Eq.(2.2)} - \text{(2.11)} \\
& \text{Physical Bounds} \\
& \text{50\% Water RejectionRate} \\
& \text{Inlet Water Specification (Seawater)}
\end{aligned}
$$

We use variations of the optimization problem (M1) for both bottom-up screening and top-down analysis. We adopt an equation-oriented (EO) approach, wherein all of the process specifics and governing engineering phenomena (e.g., thermodynamics, equipment performance, energy costs, etc.) are expressed as mathematical equations that are simultaneously converged during optimization. This approach is extremely flexible. It naturally accommodates variable bounds and facilitates embedded heat

integration during the optimization procedure. (M1) is a nonconvex optimization problem with 77 linear equality constraints, 26 nonlinear equality constraints, 6 linear inequality constraints, 6 nonlinear equality constraints, 30 quadratic equality constraints, and 136 variables. Using the Julia [25] and JuMP [44] computational environment, we can efficiently solve (M1) using IPOPT solver [147] and HSL (MA27) [1] in approximately 0.2 seconds after thoughtful initialization. The remainder of this section describes all of the mathematical equations and input data used in (M1).

2.3.2 Unit operation models

The DSE process is a collection of tanks, heat exchangers, splitters, and mixers, as shown in Figure 2.1, connected by thirteen streams contained in set $\mathcal{S}$. Variables flowrate F and temperature T are indexed by set $\mathcal{S}$. The mole fraction variable is indexed by the set of streams ($\mathcal{S}$) and the set of components ($\mathcal{C}$), which includes the directional solvent, water, and salt. Mass and energy balances and liquid-liquid equilibria equations, shown in Table 2.3, relate these variables for inlet and outlet streams. We assume the entire process operates at a steady-state, and there are no chemical reactions.

TABLE 2.3

MASS AND ENERGY BALANCES PER UNIT

Equation	Tanks	Isothermal mixer	Single phase heat exchanger
Overall mass balance	$F_{in} = \sum_{j \in \mathcal{O}} F_j$	$\sum_{i \in \mathcal{I}} F_i = F_{out}$	$F_{in} = F_{out}$
Overall component balance	$F_{in} x_{in,c} = \sum_{j \in \mathcal{O}} F_j x_{j,c} \quad \forall c \in \mathcal{C}$	$\sum_{i \in \mathcal{I}} F_i x_{i,c} = F_{out} x_{out,c} \quad \forall c \in \mathcal{C}$	$x_{in,c} = x_{out,c} \quad \forall c \in \mathcal{C}$
Chemical equilibrium	Water: $x_{o_1,w} = A + BT_{o_1}$ Salt: $x_{o_1,s} = \kappa_s$ Directional Solvent: $x_{o_2,d} = \kappa_d$		
Summation equation	$\sum_{c \in \mathcal{C}} (x_{o_1,c} - x_{o_2,c}) = 0$		
Energy Balance	$T_{in} = T_{o_1} = T_{o_2}$	$T_i = T_{out} \quad \forall i \in \mathcal{I}$	$Q = C_p F_{in} (T_{out} - T_{in})$

Each unit operation is modeled as a collection of equations that relate the inlet and outlet streams. The following variables are indexed over the set of streams $\mathcal{S}$: the molar flow F (kmol/s), the temperature T (K), and the heat capacity C_p (J/mol-K). The molar fractions x are indexed over both $\mathcal{S}$ and the components $\mathcal{C}$ which include the solvent, water, and salt. The sets $\mathcal{I} \subset \mathcal{S}$ and $\mathcal{O} \subset \mathcal{S}$ are the inlet and outlet streams of each unit operation. For simplicity, the index *in* or *out* is used if there is only one inlet or outlet, respectively. The settling tank outlets have indices o_1 and o_2 for the aqueous and solvent phases, respectively, such that $\{o_1, o_2\} = \mathcal{O}$. We assume salt has a fixed solubility of κ_s (mole fraction) in the solvent phase and the directional solvent has a fixed solubility of κ_d (mole fraction) in the aqueous phase

2.3.2.1 Liquid-liquid phase separation

The DSE process relies on temperature varying solubility of water in the directional solvent. Unfortunately, temperature-dependent ternary phase data for water, solvent, and salt are not available in the literature. For preliminary process analysis, we assume the solubility of water in the solvent is linearly dependent on temperature shown in Eq. (2.1). We fit A and B via regression analysis using experimental data for the mixture decanoic acid, water, and salt from Bajpayee *et al.* [17] and Oliveira *et al.* [108] for the mixture decanoic acid and water. Figure 2.2 shows this simple model fits the data well. Fitted parameters are reported in Table 2.4. We assume the direction solvent has a fixed solubility in the aqueous phase, denoted κ_d. Values are given in Table 2.5. Likewise, we assume salt has a solubility of $\kappa_s = 0.000003$ mol/mol in the solvent at 35°C and a solubility of $\kappa_s = 0.00030$ mol/mol in the solvent at 80°C

$$x_w = A + BT \tag{2.1}$$

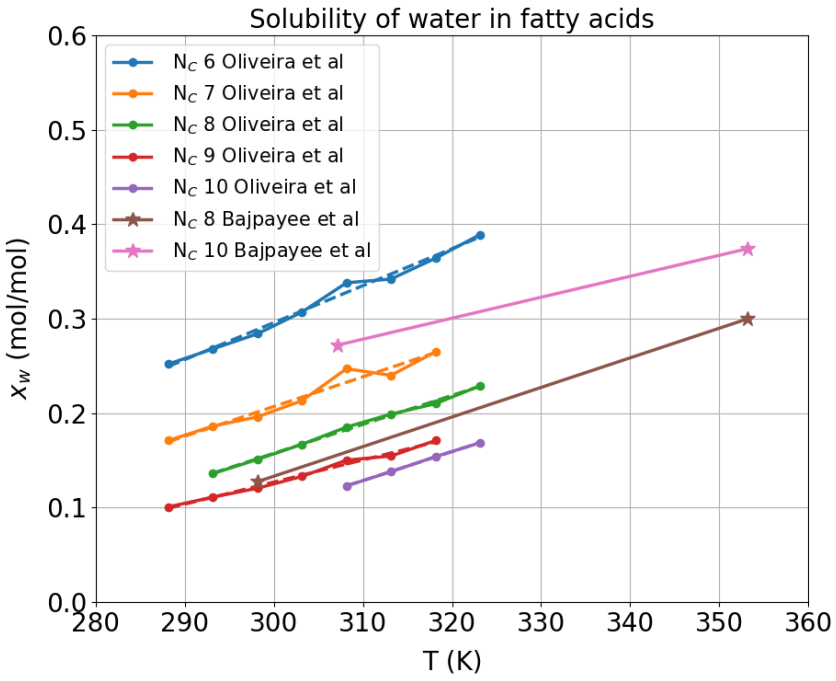

Figure 2.2. We perform linear regression on solubility to calculate the temperature swing (thermoresponsiveness) of the solubility of water in the carboxylic acid (solvent phase) using two sets of experimental data. Bajpayee *et al.* [17] provides data for ternary mixtures C_8 and C_{10} fatty acids, water, and salt. Oliveira *et al.* [108] provides data for binary mixtures of C_6 to C_{10} fatty acids and water.

TABLE 2.4

COEFFICIENTS FOR THE EQUATION $x_w = A + BT$ FOR SOLUBILITY CORRELATION FOR CARBOXYLIC ACIDS AND [EMIM][TF_2N][62]

Bajpayee *et al.* [17]		
Number of carbons	**A (mol/mol)**	**B (mol/mol K)**
8	-0.8304	0.0032
10	-0.4091	0.0022
Oliveira *et al.* [108]		
Number of carbons	**A (mol/mol)**	**B (mol/mol K)**
6	-0.8784	0.0039
7	-0.7367	0.0031
8	-0.7618	0.0031
9	-0.5743	0.0023
10	-0.8187	0.0036
Ionic liquid	**A (mol/mol)**	**B (mol/mol K)**
[emim][Tf_2N]	-1.3417	0.0063

TABLE 2.5

SOLUBILITY OF CARBOXYLIC ACIDS AND IONIC LIQUID IN WATER [22, 62]

Acid	**N_c**	**Solubility in water (mol/mol)**	**Solubility in water [ppm]**
Hexanoic	6	1.678E-3	10,820
Heptanoic	7	3.348E-4	2,419
Octanoic	8	8.495E-5	680
Nonanoic	9	3.416E-5	300
Decanoic	10	1.339E-5	128
Ionic Liquid		**Solubility in water (mol/mol)**	**Solubility in water [ppm]**

2.3.2.2 Single-phase heat exchanger

The heat duty in the heat exchanger is $Q = C_p F_{in}(T_{out} - T_{in})$, where C_p is the heat capacity, F_{in} is the flowrate, and $T_{out} - T_{in}$ is the temperature difference. We calculate C_{pi} for the organic solvent i with the capacity group contribution method [106]:

$$C_{pi} = \sum_{k \in \mathcal{G}} N_k (A_k + B_k t) \qquad t = T/1000 \tag{2.2}$$

Eq. (2.2) captures the influence of N_k times of functional group k appears in the organic component i. For water we use coefficients given in Table 2.7[106]:

$$C_{pi} = A + Bt + Ct^2 + Dt^3 + E/t^2, \qquad t = T/1000 \tag{2.3}$$

and for the ionic liquid, we use coefficients given in Table 2.7 and Eq. (2.4) [56].

$$C_{pi} = A + BT \tag{2.4}$$

We then calculate the C_p of each stream (mixtures) using the the component heat capacities C_{pi} and the mole fractions x_i:

$$C_p = \sum_{i \in C} C_{pi} x_i \tag{2.5}$$

The heat capacity of NaCl is considered constant with a value of 15.058 J/mol-K [106]. Coefficients for Eqs. (2.2)-(2.4) are given in Tables 2.6 and 2.7.

TABLE 2.6

HEAT CAPACITY PARAMETERS FOR GROUP CONTRIBUTION METHOD [106]

Functional group	**A**	**B**
	J/molK	J/mol-K^2
CH_3	14.5504	54.060
CH_2	19.539	32.21
COOH	-49.7595	421.11

TABLE 2.7

HEAT CAPACITY PARAMETERS FOR

$C_{pi} = A + Bt + Ct^2 + Dt^3 + E/t^2$, $t = T/1000$ (J/MOL-K)[106, 56]

Component	**A**	**B**	**C**	**D**	**E**
	(J/mol-K)	(J/mol-K*kK)	(J/mol-K*kK^2)	(J/mol-K*kK^3)	(JkK^2/molK)
H_2O	-203.6060	1583.29	- 3196.43	2474.455	3.855326
[emim][Tf_2N]	430.39	0.315	0	0	0

2.3.3 Embedded heat integration

We embed the Duran-Grossmann heat integration equations [45] directly into the process optimization problem. This allows us to simultaneously optimize the process operating conditions (flowrates, compositions, temperatures) while minimizing the thermal energy input per unit of freshwater product. This analysis goes beyond that of Alotaibi *et al.* [9] which only considers heat integration for fixed process operating conditions. Our approach optimizes more degrees of freedom. The optimizer manipulates flowrates, compositions, and temperatures to balance complex interdependencies between temperature-dependent phase equilibria and the pinch point, which limits heat integration. For completeness, we now summarize the heat integration model.

Each single-phase heat exchanger half is designated as a hot stream (requires cooling) or a cold stream (requires heating), denoted with sets $\mathcal{S}_\mathcal{H}$ and $\mathcal{S}_\mathcal{C}$, respectively. We then consider the inlet of each heat exchanger as a pinch candidate temperature T^p and add the minimum driving force ΔT_{min} to the cold stream temperatures:

$$T^p = \begin{cases} T_p^{in} & \forall \quad p \quad \in \mathcal{S}_\mathcal{H} \\ T_p^{in} + \Delta T_{min} & \forall \quad p \quad \in \mathcal{S}_\mathcal{C} \end{cases} \tag{2.6}$$

We use the set $\mathcal{P} = \mathcal{S}_\mathcal{C} \cup \mathcal{S}_\mathcal{H}$ to denote all pinch candidate temperatures. For each pinch candidate $p \in \mathcal{P}$, we calculate the heat content above pinch temperature T^p:

$$QA_H^p = \sum_{i \in \mathcal{S}_\mathcal{H}} FC_{pi}[\tilde{\max}(T_i^{in} - T^p) - \tilde{\max}(T_i^{out} - T^p)], \quad \forall p \in \mathcal{P} \tag{2.7}$$

Similarly, we calculate the heat content below pinch temperature T^p:

$$QA_C^p = \sum_{i \in \mathcal{S}_\mathcal{C}} FC_{pi}[\tilde{\max}(T_j^{out} - T^p + \Delta T_{min}) - \tilde{\max}(T_i^{in} - T^p - \Delta T_{min})], \quad \forall p \in \mathcal{P} \tag{2.8}$$

The minimum hot utility duty Q_S must be larger than the difference between the heat contents below and above each pinch candidate.

$$\underbrace{Q_S}_{\text{heating utility}} \geq \underbrace{QA_C^p}_{\substack{\text{heat content above} \\ \text{pinch candidate}}} - \underbrace{QA_H^p}_{\substack{\text{heat content below} \\ \text{pinch candidate}}} \quad \forall \quad p \in \mathcal{P} \tag{2.9}$$

Finally, we use an energy balance to calculate the minimum cold utility duty Q_W:

$$\underbrace{Q_W}_{\text{cooling utility}} = \underbrace{Q_S}_{\text{heating utility}} + \underbrace{\sum_{j \in \mathcal{S}_\mathcal{C}} Q_j^{in}}_{\text{internal heating}} - \underbrace{\sum_{i \in \mathcal{S}_\mathcal{H}} Q_i^{out}}_{\text{internal cooling}} \tag{2.10}$$

To ensure optimization problem is differentiable, we use a smoothed approximation for the max operator:

$$\tilde{\max}(x) = \frac{1}{2}\left(\sqrt{x^2 + \epsilon^2}\right) \approx \max(x, 0), \qquad \epsilon^2 = 10^{-6} \tag{2.11}$$

This model is effective because the combinatorial search for the pinch candidate is cast as the inequality constraint Eq. (2.9), which is efficiently handled in equation oriented process optimization.

2.3.4 Cost model

After solving (M1), we estimate equipment and operating costs and then calculate the price per unit of freshwater production.

The heat integration model described above only computes the minimum hot and cold utilities when solving (M1). As a post-processing step, we perform sequential optimization to design the heat exchanger network. We first solve a mixed integer linear program to predict matches to minimize the number of heat exchangers. We then solve a nonlinear program to calculate the heat exchanger areas.[111, 26]. Fi-

nally, we use Guthrie's Method [26] to calculate the equipment costs. We used the present cost index of December 2018 (613.6) and assumed a salvage value of 20% of the cost of the assets after the useful life of the plant.

Eq. (2.12) calculates the annualized capital cost C_{anm} in which CRF is the capital recovery factor, C_{NPC} is the net present cost (calculated thorugh Guthrie's Method), i is the real discount rate, i' is the nominal discount rate, and f is the expected inflation rate. We used a nominal discount rate of 8%, and an expected inflation rate of 3.5% over a 20 year period obtaining a real discount rate of 4.5%. Utilizing the previous values, we calculate a CRF of 0.077.

$$C_{anm} = (CRF) \times (C_{NPC}) \tag{2.12}$$

$$CRF = \frac{i(1+i)^N}{(1+i)^N - 1} \tag{2.13}$$

$$i = \frac{i' - f}{1+f} \tag{2.14}$$

We assume a cost of electricity of 0.05 \$/kW (average price of Texas, Oklahoma, Lousiana, New Mexico, Georgia, and Utah) [6]. We assume a 2 psi pressure drop every 100 feet, and the heigh of the tanks is calculated for every process solution for pumping electricity. We assume a cost of heating utilities of 2.778 \$/GJ from waste heat, a similar cost to solid waste, coal, or nuclear energy [141]. We assume the system has a useful life of 20 years for cost calculations, and we selected stainless steel for the material of the equipment because the plant handles saline brines and freshwater. The cost of decanoic acid is set to 12 \$/kg [4]. Finally, we calculate levelized cost of water (LCOW) as:

$$\text{LCOW} = \frac{\text{Equipment costs} + \text{Utility costs} + \text{Solvent Costs}}{\text{Total lifetime freshwater generation}} \tag{2.15}$$

2.4 Results: Bottom-up Process Optimization

We now solve the optimization problem (M1) in several bottom-up case studies to predict the best possible performance of candidate directional solvents in a fully optimized process. We first compare our optimized reference design with Alotaibi *et al.* [9]. Then, we perform a sensitivity analysis to quantify the impact of ΔT_{min} (heat exchanger size) and the maximum temperature (heat source quality). Finally, we compare candidate organic acid solvents.

2.4.1 Reference design for decanoic acid directional solvent

We set the temperature bounds between 34°C and 80°C, specify a 50% reject ratio, and set $\Delta T_{min} = 6°C$[1] to match Altoabi *et al.* [9]. (See Section 5.2 for bound and ΔT_{min} sensitivity analysis.) Results from solving (M1) are shown in Tables 2.8, 2.9, 2.10 and Figure 2.3. From the results, we draw five observations:

Observation A1. A considerable portion of the decanoic acid (128 ppm) is solubilized in the outlet of freshwater and salty brine. We calculate that, at steady-state, the process requires 10^{-4} kmol/s of make-up directional solvent. We emphasize this make-up was not considered by Alotaibi *et al.*[9], who based their process analysis on pseudo-steady-state experimental data.

Observation A2. Our approach finds the same pinch point, 50°C, as Altoabi *et al.* [9].

Observation A3. Solving (M1) predicts specific (thermal) energy of 191 kW_t/m^3 of freshwater with decanoic acid as a solvent, whereas Alotaibi *et al.* [9] report 180 kW_t/m^3 of freshwater. We highlight two differences that can explain our 9% larger specific energy: first, the addition of a feed (make-up) stream of decanoic acid. Second, we cool down the solvent-water emulsion stream to 34°C (limiting

[1]Altoabi *et al.* [9] report a heat exchanger effectiveness of 90%, which we convert to $\Delta T_{min} = 6°C$.

temperature due to solvent crystallization) in contrast to the 40°C used by Alotaibi *et al.* [9].

Observation A4. Solving the cost analysis for treating 1 m^3 of water results in a cost of \$3.31 /m^3 of freshwater. The cost is high compared to modern technologies: between \$0.27 /m^3 and \$1.62 /m^3 of freshwater. Solvent loss has a significant influence on the cost of DSE desalination.

Observation A5. To validate the heat capacities, we repeated the analysis with C_p experimental data [152, 124] and found that this leads to a 7% difference in specific energy. Due to the lack of data for other species, we will use the correlation in Eqs. (2.2) throughout the analysis to be consistent.

TABLE 2.8

STREAM RESULTS FOR REFERENCE DESIGN WITH DECANOIC ACID AS SOLVENT USING 80°C AS MAXIMUM ALLOWABLE TEMPERATURE ΔT_{min}=6°C.

Stream	**Flow**	**Temperature**	x_d	x_w	x_s
	kmol/s	°C	%mol	%mol	%mol
1	0.5	25	0.00	98.89	1.11
2	0.5	80	0.00	98.89	1.11
3	1.81	80	63.18	36.78	10^{-4}
4	0.25	80	10^{-3}	97.97	1.99
5	1.81	34	63.18	36.78	10^{-4}
6	0.25	34	10^{-4}	99.78	0.21
7	1.56	34	73.33	26.66	10^{-4}
8	1.56	80	73.33	26.66	10^{-4}
9	2.06	80	55.50	44.22	0.26
10	0.25	25	10^{-3}	97.97	1.99
11	0.25	25	10^{-4}	99.78	0.21
12	10^{-4}	34	100	0.00	0.00
13	10^{-4}	80	100	0.00	0.00

See Figure 2.1 for schematics. Flowrates are comparable to Table 3 in Alotaibi *et al.* [9]

TABLE 2.9

HEAT EXCHANGER SIZES AND TEMPERATURES FOR THE REFERENCE DESIGN (DECANOIC ACID AS SOLVENT, 80°C AS MAXIMUM ALLOWABLE TEMPERATURE).

Heat exchanger	**Stream**		**Temp (°C)**		**Q (kW)**
	Inlet	Outlet	Inlet	Outlet	
HX1	S1	S2	25	80	2.09
HX2	S3	S5	80	34	-23.44
HX3	S7	S8	34	80	23.00
HX4	S4	S10	80	25	-1.045
HX5	S6	S11	34	25	-0.17
HX6	S12	S13	34	80	3.2E-3

More than 90% of the heating and cooling occurs in heat exchangers HX3 and HX2, respectively. This is due to the large amount of decanoic acid that must be recycled to a achieve an overall 50% extraction ratio. For practical considerations, one may choose not to add HX6 due to the low heat duty of the heat exchanger and the small flow of solvent

TABLE 2.10

HEAT INTEGRATION RESULTS FOR THE REFERENCE DESIGN.

Heat exchanger	**Exchanger Inlet**	**Type of Stream**	**QA$_h$ (kW)**	**QA$_c$ (kW)**	**QA$_c$-QA$_h$ (kW)**
HX1	S1	Cold	24.03	24.31	0.28
HX2	S3	Hot	0.01	3.12	3.11*
HX3	S7	Cold	20.77	23.88	3.10
HX4	S4	Hot	0.01	3.12	3.11*
HX5	S6	Hot	23.88	24.17	0.28
HX6	S12	Cold	20.77	23.88	3.10

* Pinch temperature

QA$_h$ is the heat exchanged above the pinch temperature and QA$_c$ is the heat below the pinch temperature. Both streams S3 and S4 are at the pinch temperature of 50°C

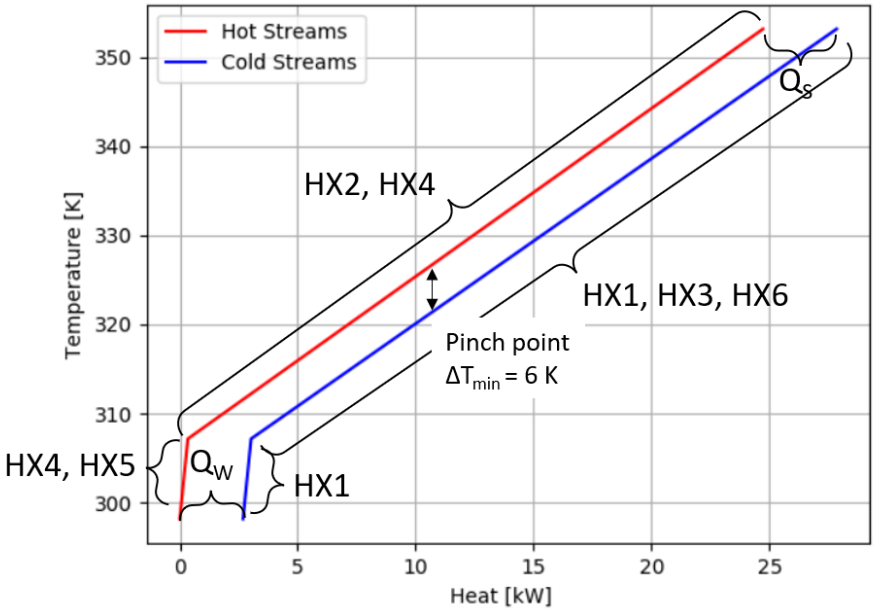

Figure 2.3. Composite curves for the reference design, including utilities. Most of the heat exchange is done in HX2 and HX3, which have the largest temperature difference and the highest flowrates. Recall HX1 heats inlet seawater to the temperature of the warm settling tank, HX2 cools the water-decanoic acid emulsion, and HX3 heats the recycled directional solvent. HX4 and HX5 cool the outlet concentrated brine and freshwater, respectively. Q_S and Q_W are defined as the minimum heating and cooling utility duties, respectively.

TABLE 2.11

LCOW FOR THREE DIFFERENT DIRECTIONAL SOLVENTS

WITHOUT CONSIDERING SOLVENT RECOVERY.

Directional solvent	LCOW	Solvent cost		Electricity cost		Thermal energy cost		Equipment cost	
	$	$	%	$	%	$	%	$	%
Decanoic acid	3.30	1.03	31.21	0.31	9.39	1.92	58.18	0.04	1.21
Octanoic acid	4.13	2.48	60.05	0.20	4.85	1.42	34.38	0.03	0.73
[emim][Tf_2N]	43.03	42.60	99.02	0.07	0.17	0.34	0.78	0.01	0.03

Costs of thermal energy, pumping electricity and equipment are lower using ionic liquid. However the cost of the solvent make-up increases considerably

2.4.2 Sensitivity analysis: Maximum temperature and ΔT_{min}

Next, we considered the sensitivity of process designs to both the maximum temperature and ΔT_{min}, which controls the heat exchanger size and effectiveness. We solve (M1) with three different sets of experimental data as the LLE correlation input: decanoic acid-water data form Oliveira *et al.* [108], decanoic acid-water-salt data from Bajpayee *et al.* [18], and [emim][Tf_2N]-water-salt data from Guo *et al.* [62]. Figure 2.4 shows specific energy at six maximum temperature between 40 °C and 90 °C and ten different ΔT_{min} between 1 °C and 10 °C. Figure 2.5 shows specific energy at five maximum temperature between 35 °C and 75 °C and ten different ΔT_{min} between 1 °C and 10 °C. Solving (M1) 169 times to generate Figures 2.4 and 2.5 took less than 1 minute. Table 2.12 gives the stream information for a single design from the sensitivity analysis (T_{max} =50°C, ΔT_{min} =6 °C). From these results, we observe:

Observation B1. We find consistent trends with both sets of solubility data. Bajpayee *et al.* data[18] showed 2.6% more solubility of water in the solvent phase, which leads to 2 times lower energy insensity because the recycle ratio is decreased. The difference between the solubilities is because Oliveira *et al.* only considered binary water-acid mixtures.

Observation B2. As expected, higher maximum temperatures enable higher per pass extraction, which allows for a lower recycle flowrate (1.81 kmol/s for T_{max}= 80°C versus 4.91 kmol/s for T_{max}=50°C) and lower energy intensity (191.84 kW_t/m^3 for T_{max}= 80°C verus 551.90kW_t/m^3 for T_{max}=50°C). This suggests that manipulating the solvent chemistry to increase the per pass extraction at a lower temperature will decrease the energy intensity.

Observation B3. The specific energy difference between temperature ≤80°C and ≤90°C is negligible. This is because increasing the pass per extraction increases the fraction of water in the solvent-water emulsion, which decreases the C_p of the mixture. As the amount of heat required to heat the mixture de-

creases at a higher maximum allowable temperature, so does the specific energy of the process. This result emphasizes little benefit for heat sources greater than 80°C for off-the-shelf organic acid solvents.

Observation B4. Heat exchangers with a temperature difference of less than 3°C are likely required to achieve less than $50\text{kW}_\text{t}/\text{m}^3$ and 4°C to achieve less than $100\text{kW}_\text{t}/\text{m}^3$ utilizing decanoic acid as a solvent. The heat exchangers would need to have an effectiveness of approximately 96% or higher to achieve the $50\text{kW}_\text{t}/\text{m}^3$ goal utilizing decanoic acid.

Observation B5. We observe the IL the solvent [emim][Tf_2N] can achieve 50 $\text{kW}_\text{t}/\text{m}^3$ using maximum allowable temperature of 65°C and ΔT_{min} of 6°C. Our analysis shows that, from an energetics perspective, ILs are a more promising class of directional solvents.

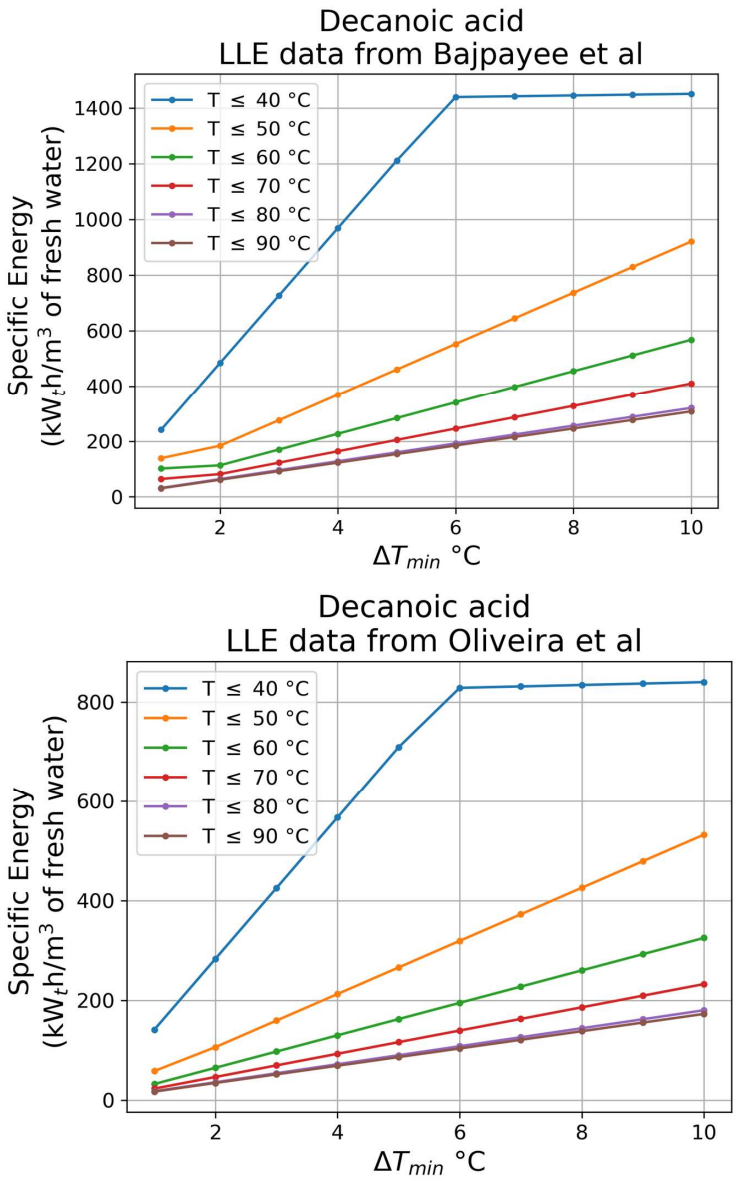

Figure 2.4. Sensitivity of specific energy to maximum temperature (heat source quality) and ΔT_{min} (heat exchanger size). Bajpayee *et al.* [18] data showed 2.6% more solubility of water in the solvent phase from Oliveira *et al.* [108]. The difference may be explained by the interaction of salt in the mixture. Higher maximum temperatures enable higher per pass extraction, which allows for a lower recycle flowrate and lower energy intensity. Solvents that enables higher per pass extraction at a lower temperature, the decrease in energy intensity would be higher. The specific energy difference between allowing (M1) to reach 80°C and 90°C is negligible. Heat exchangers with a temperature difference of less than 3°C are to achieve less than 50 kW_t/m^3.

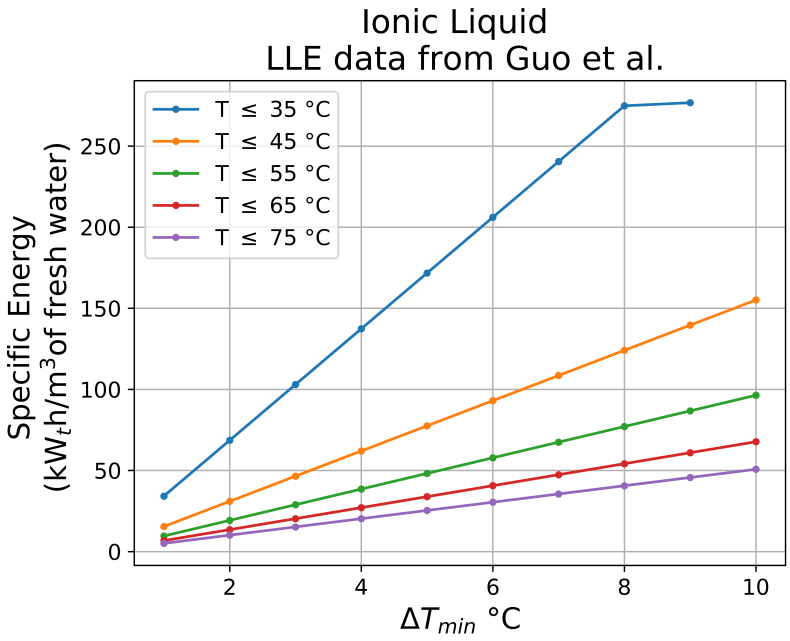

Figure 2.5. Effects of maximum temperature allowed for the process utilizing [emim][Tf_2N] as solvent. The specific energy of the process is greatly reduced compared to carboxylic acids.

TABLE 2.12

STREAM RESULTS FOR REFERENCE DESIGN WITH DECANOIC ACID AS SOLVENT USING 50°C AS MAXIMUM ALLOWABLE TEMPERATURE ΔT_{min}=6°C.

Stream	**Flow**	**Temperature**	x_d	x_w	x_s
	kmol/s	°C	%mol	%mol	%mol
1	0.5	25	0.00	98.89	1.11
2	0.5	50	0.00	98.89	1.11
3	5.16	50	69.79	30.18	0.03
4	0.25	50	10^{-3}	98.41	1.58
5	5.16	34	69.79	30.18	0.03
6	0.25	34	10^{-4}	99.37	0.62
7	4.91	34	73.33	26.66	10^{-4}
8	4.91	50	73.33	26.66	10^{-4}
9	5.16	50	66.56	33.33	0.10
10	0.25	25	10^{-3}	98.41	1.58
11	0.25	25	10^{-4}	99.37	0.63
12	10^{-4}	34	100	0.00	0.00
13	10^{-4}	50	100	0.00	0.00

See Figure 2.1 for stream numbers

2.4.3 Sensitivity analysis: Length of the chain of carboxylic acids

We now rapidly screen five carboxylic acids as directional solvents. We solve (M1) using acid-water mixture data for Oliveira *et al.* [108]. We set the amount of acid dissolved in the aqueous phase as the solubility of the fatty acid at 20°C, shown in Table 2.5. The minimum temperature for the process is set as the larger of the melting temperature of the acid or 25°C at ambient temperature. The 120 instances of (M1) shown in Figure 2.6 were solved in approximately 25 seconds total. From the results, we observe:

Observation C1. In Figure 2.2, we see there is not a clear relationship between the solubility of water in organic acid and the length of the carbon chain. However, we find the slope B, i.e., the thermoresponsiveness of solubility, is most influential on specific energy.

Observation C2. For solvent selection, the three most important factors are i) the change in water solubility for a fixed temperature change (thermoresponsiveness); ii) the melting temperature of the fatty acid, which limits the minimum operating temperature; and iii) the solubility of the directional solvent in freshwater.

Observation C3. Similar to observation B4, high-performance heat exchangers are required to achieve less than 50 kW_t/m^3 using C_6 to C_{10} fatty acids

Observation C4. The cost of the process decreases with the length of the carboxylic acid chain. The solvent solubility in water decreases as the carbon chain increases, diminishing the amount of solvent loss and the solvent make-up cost in the process.

Observation C5. DSE process using fatty acids are not economically viable, with a best-case scenario of \$1.29 per m^3 of freshwater for decanoic acid with heat exchangers with ΔT_{min} of 1°C.

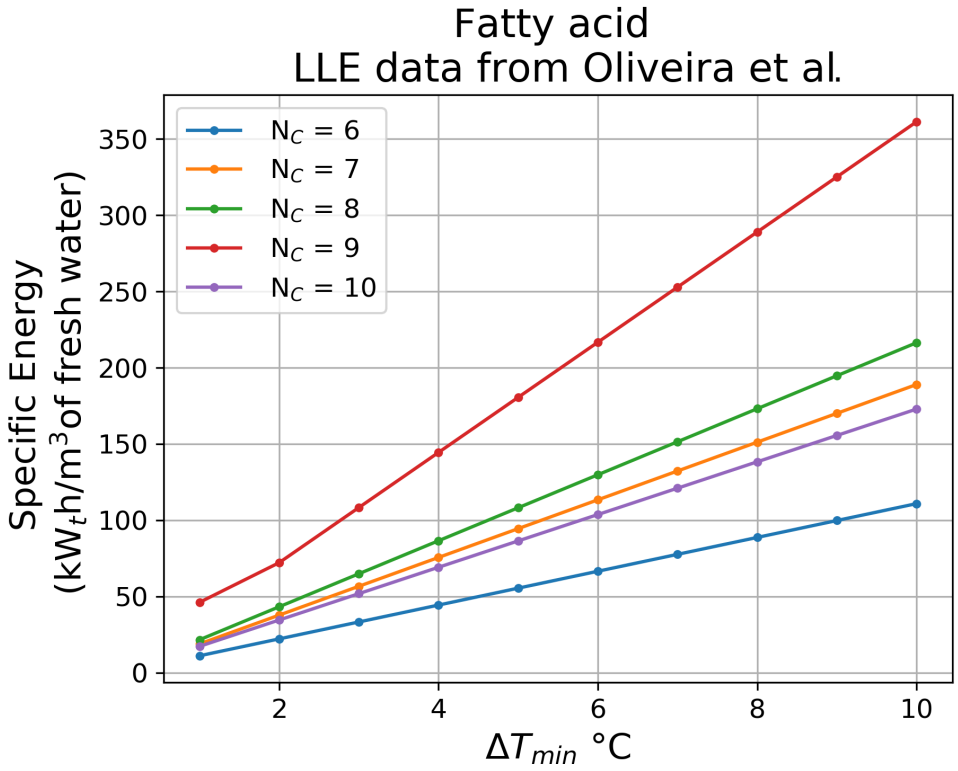

Figure 2.6. Effects on specific energy using different carboxylic acids as the DS. There is not a clear influence in the length of the chain of carbons (N_c) in the energy required for the process. DSE remains energy intensive utilizing any C_6 to C_{10} carboxylic acid and suffers from solvent loss.

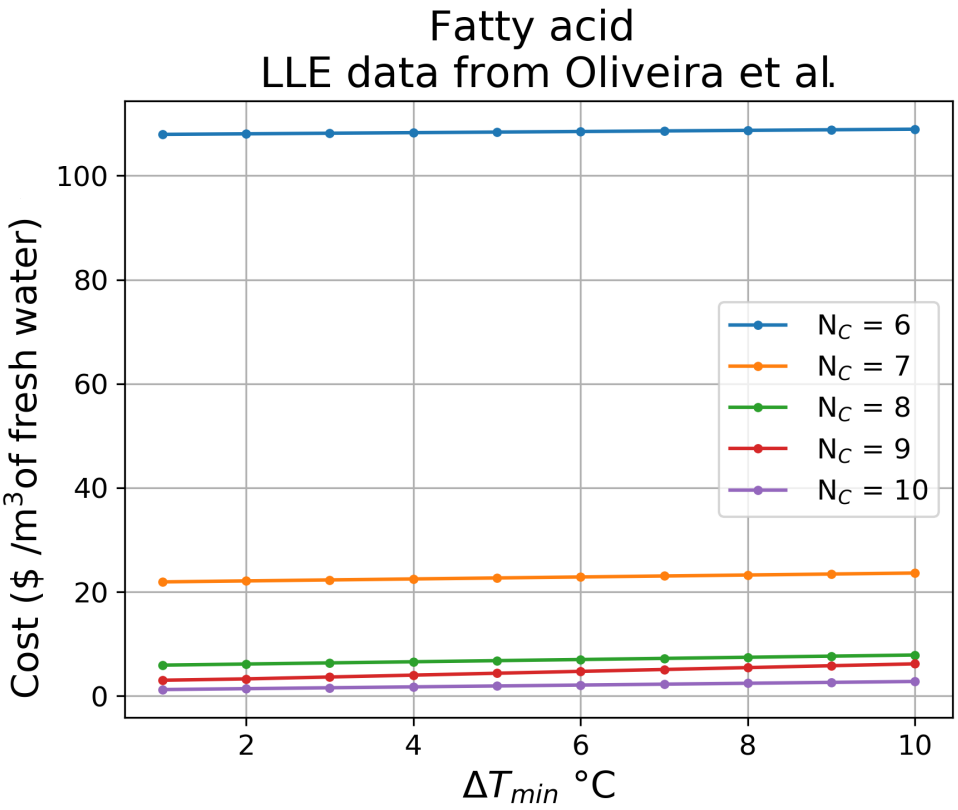

Figure 2.7. Effects on the cost of the DSE process utilizing C_6 to C_{10} fatty acids. The cost of the process increases with the increase of solubility of the solvent in water. The LCOW for ΔT_{min} from 1°C to 10°C for different carboxylic acids are 107.91-108.99 \$/m^3 for $N_c = 6$, 21.91-23.55 \$/m^3 for $N_c = 7$, 5.90-7.86 \$/m^3 for $N_c = 8$, 3.00-6.18 \$/m^3 for $N_c = 9$, and 1.29-3.79 \$/m^3 for $N_c = 10$. See Table 2.5 for specific quantities of solvent loss.

2.5 Results: Top-Down Solvent Property Targets

Based on the bottom-up analysis in Section 5, we conclude that known carboxylic acids are not an economical solution for directional solvent extraction. Although [emim][Tf_2N] is, from an energetic perspective, a more promising directional solvent, limited data for IL-water-salt mixtures prevents bottom-up screening of more candidate IL solvents.

In this section, we generalize the optimization problem (M1) to consider hypothetical directional solvent molecule parameterized by three continuous properties: solubilities in the aqueous and solvent phases and cost of the solvent. Thus we perturb four parameters in the technoeconomic analysis: A, B, solvent cost, and κ_d. We then perform top-down sensitivity analysis to identify **idealized directional solvent property targets** to aid in molecular discovery. These continuous physical property targets are a precursor to discrete molecular optimization [19].

2.5.1 Top-down analysis: Carboxylic acids

We start by performing a sensitivity analysis for hypothetical carboxylic acid solvents over a grid for three properties: 1) the thermoresponsiveness of the solubility of the solvent (B), 2) the amount of water that solubilizes in the solvent at a reference temperature (A), and 3) the amount of solvent dissolved in the freshwater at the outlet of the DSE process (κ_d). Each candidate set of properties is first checked to ensure the solubility correlation Eq. (2.1) predicts a valid mole fraction between 0 and 1 at the process temperature bounds (T_{min} and T_{max}):

$$0 \leq A + BT_{max}, \quad 1 \geq A + BT_{max}, \quad 0 \leq A + BT_{min}, \quad 1 \geq A + BT_{min} \tag{2.16}$$

We found Eq. (2.16) is extremely effective at predicting if (M1) will be infeasible. For each set of properties that satisfy Eq. (2.16), we solve (M1) to compute flowrates and

temperatures that minimize specific energy. For each solution of (M1), we estimate LCOW for a few solvent costs. From the results shown in Figure 2.8, we conclude:

Observation D1. For a directional solvent similar to a fatty acid, increasing thermoresponsive ability (B) and decreasing solubility of the solvent in water (κ_d) would cause the greatest reduction in LCOW. Likewise, increasing the solubility of water in the solvent at a reference temperature (B) reduces the recycle ratio by decreasing the amount of solvent needed for water to dissolve. We calculate LCOW of \$3.30/m^3 and \$4.13/m^3 for decanoic and octanoic acids, respectively. Even though the energy contribution to LCOW is lower from octanoic acid (\$1.62/m^3 versus \$2.20/m^3), the overall LCOW is larger because the higher solubility of the solvent κ_d is larger (128 ppm for decanoic acid versus 300 ppm for octanoic acid), which causes larger solvent make-up costs (\$1.03/m^3 of freshwater for decanoic acid versus \$2.48/m^3 of freshwater for octanoic acid).

Observation D2. Figure 2.8 gives quantitive targets to reduce LCOW for a fatty acid-like directional solvent. For example, doubling the thermoresponsive ability (B) and reducing the solubility of the solvent in water by 10-fold (κ_d=128 ppm to 12.8ppm) relative to decanoic would give a LCOW less than \$0.50/m^3.

Observation D3. The recycle ratio is reduced as the thermoresponsive ability (B) of the solvent and the base solubility of water in the solvent (A) increase. This reduces the thermal and electric energy required to heat, pump, and cool the recycle of the DSE-water emulsion. Reducing the recycle ratio also drastically shrinks the size of the equipment. For example, increasing the thermoresponsiveness of the solvent by a factor of 2 decreases the recycle ratio by a factor of 20, which decreases the heat and electricity costs from \$2.20 per m^3 of freshwater to \$0.21 per m^3 of freshwater and decreases equipment sizes by 400%.

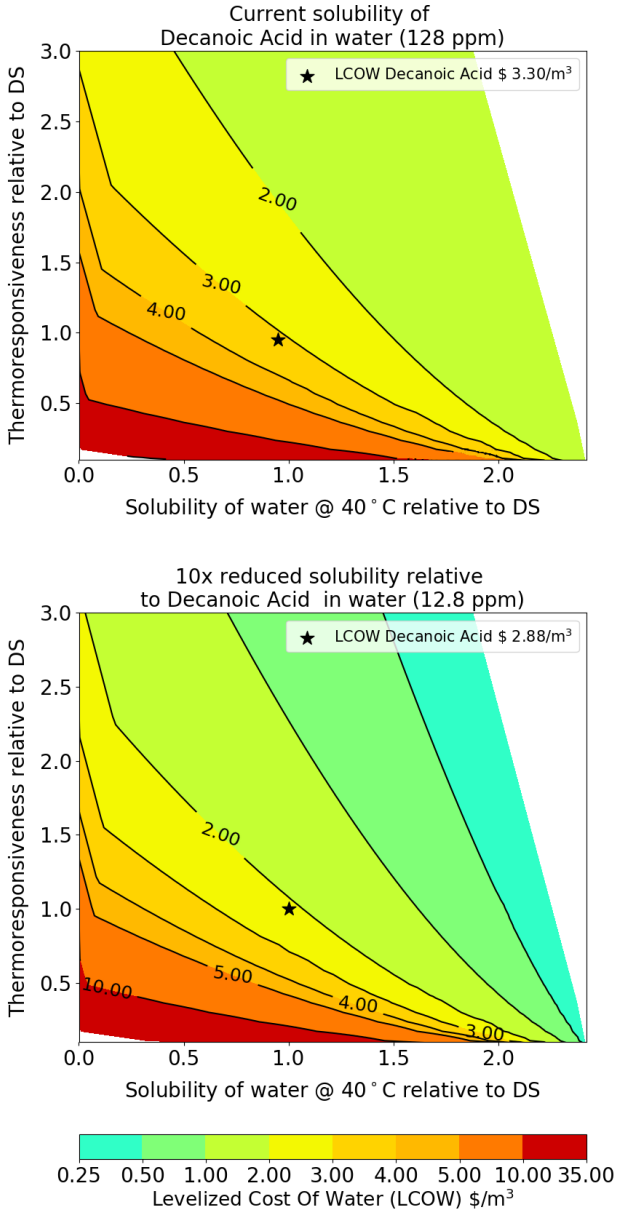

Figure 2.8. The colored contours show LCOW calculated using \$12/kg cost of decanoic acid as a function of thermoresponsivness (A, vertical axis) and the solubility of water at 40 °C(B, horizontal axis). Both axes are scaled such that 1.0, which is marked with a $\star$, corresponds to decanoic acid. (Top) Using the current solubility of the solvent in water (κ_d=128 ppm), a 2-fold improvement in both properties A and B result in a LCOW above \$1/m^3. (Bottom) Reducing the solubility of the solvent in water by 10-fold (κ_d=12.8 ppm) reduces the LCOW to \$2.88/m^3. Even with this improvement, A and B both need to increase by 1.5-fold to reach the \$0.5/m^3 LCOW goal.

2.5.2 Top-down analysis: Ionic liquids

Next, we perform a sensitivity analysis for hypothetical IL directional solvents. Compared to carboxylic acids, ILs are a less mature chemical technology. We consider a current benchmark price of \$1,000/kg of [emim][Tf_2N] [5]. However, many expect economies of scale to dramatically reduce the cost of ILs as the market for these solvents grows. For example, Shiflett *et al.* [128] shows a price reduction of 92% for $[C_2MIM]^+[Ace]^-$ and 90% for $[C_2MIM]^+[BF_4]^-$. For the sensitivity analysis, we consider three IL costs - \$1,000/kg, \$100/kg, and \$10/kg - to quantify order of magnitude changes. Due to these comparatively high costs, solvent loss is especially important for ILs compared to carboxylic acids. Thus, it is desirable to consider solvent recovery systems, such as a membrane for post-treatment.[2] For simplicity, we consider the complete recovery of the solvent from the freshwater feed product, which can be recovered with a nanofiltration polishing step.

Observation E1. The sensitivity analysis assumes a perfect recovery of the solvent with nanofiltration on the freshwater side. For [emim][Tf_2N] we found a LCOW of \$22.11/m^3. If only 90% of the IL on the freshwater side is recovered, we predict a LCOW of \$24.28/m^3. This suggests that the highest cost is the solvent loss in the salty brine, where nanofiltration is not viable due to membrane fouling.

Observation E2. [emim][Tf_2N] is approximately 2 times more thermoresponsive (A) than decanoic acid (0.0063 mol/mol/°C vs. 0.0022 mol/mol/°C). However, at the current price of the ionic liquid, the solvent loss (κ_d) is critical. Figure 2.9 predicts that a ten-fold decrease in κ_d decrease LCOW to only 12% of the original cost. Improving the thermoresponsiveness (B) alone is insufficient for ILs to

[2]We anticipate IL recovery from the freshwater stream is achievable with off-the-shelf filtration systems. Post-treatment for the brine reject is much more challenging due to concerns of membrane fouling. Full costing of the freshwater post-treatment system is beyond the scope of this work. Instead, we neglect capital costs and energy usage. As such, the property targets are optimistic but informative.

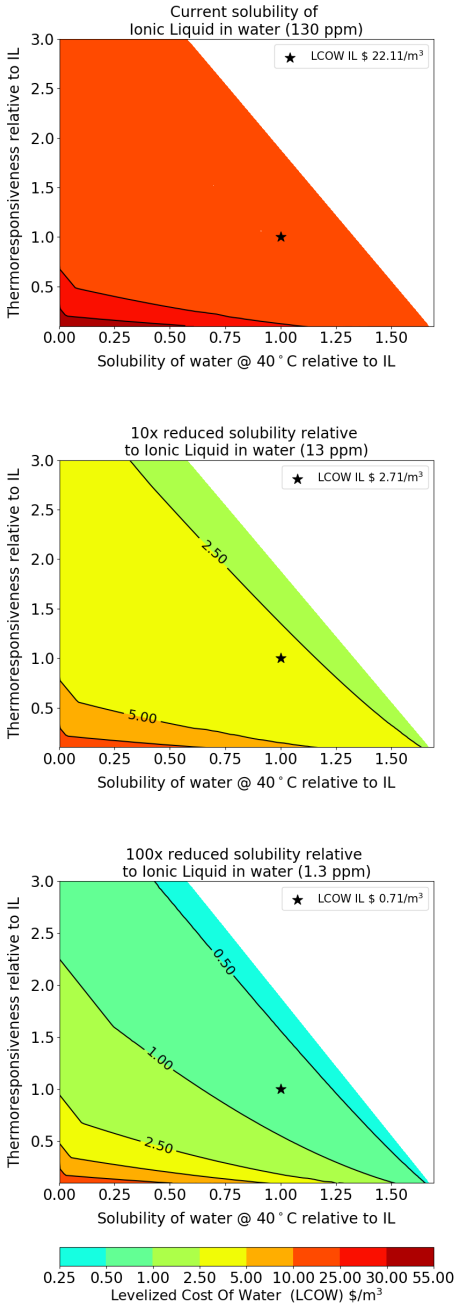

Figure 2.9. The colored contours show LCOW calculated using \$1,000/kg cost of [emim][Tf_2N] as a function of thermoresponsivness (A, vertical axis) and the solubility of water at 40 °C (B, horizontal axis). Both axes are scaled such that 1.0, which is marked with a $\star$, corresponds to [emim][Tf_2N]. Three scenarios for the solubility of IL in water κ_d are considered: (top) baseline, (middle) 10-fold decrease, and (bottom) 100-fold decrease.

be LCOW-competitive with carboxylic acids. Assuming the current price of IL, the solvent would still require a 100 fold reduction of the solvent solubility ($x_{o_1,d}$).

Observation E3. Assuming a 90% cost reduction, the thermoresponsivness would need to be increased 1.5 times or the solubility of water 1.25 times. However, the solvent's solubility in water would need to be reduced by a ten-fold, as shown in Figure 2.9.

Observation E4. For a cost of [emim][Tf_2N] of \$10/kg, the solvent solubility in water should be 10 times lower to achieve the goal of \$0.50/m^3 LCOW. However, it is also possible to reach this goal by increasing the solubility of water in the solvent by 1.2 times or increasing the thermoresponsiveness by 1.5 times.

Observation E5. For solvent with a cost as high as [emim][Tf_2N], the thermoresponsivness (B) and the solubility of water in the solvent (κ_d) are the most important properties. With the current solvent solubility data, one would need to reduce the solvent loss at least ten-fold for ILs to be LCOW-competitive, even with a solvent cost reduction of 99%.

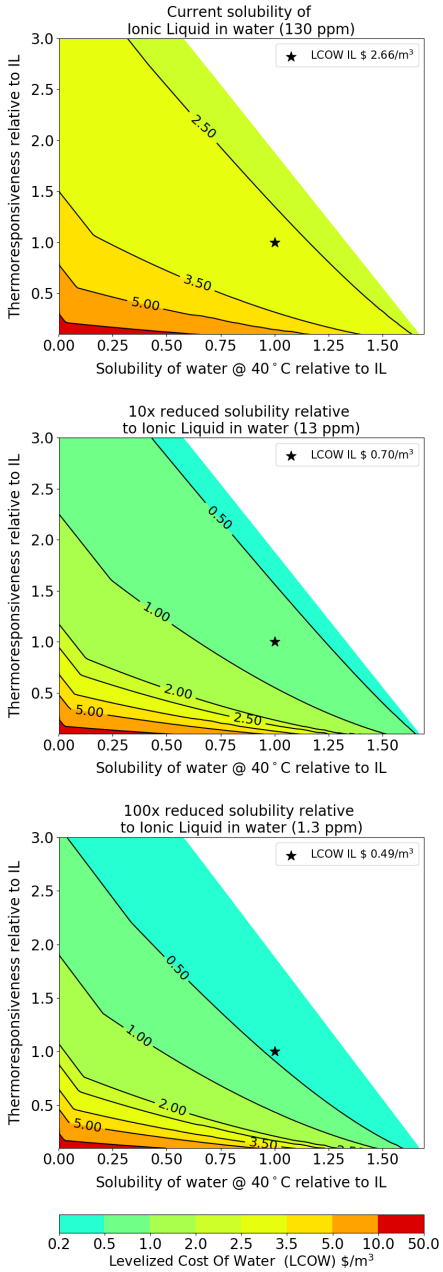

Figure 2.10. Colored contours show LCOW calculated using \$100/kg of [emim][Tf_2N]. (Top) Assuming κ_d=130 ppm, the solvent loss severely raises LCOW. (Middle) Assuming a ten-fold decrease in κ_d, only a 1.25-fold increase in A or a 1.5-fold increase in B is needed to achieve a LCOW less than \$0.50/m^3. New unpublished data suggest these low solubility scenario is reasonable for a salty brine. (Bottom) A 100-fold decrease in κ_d alone gives a LCOW of \$0.49/m^3 under this low IL cost scenario.

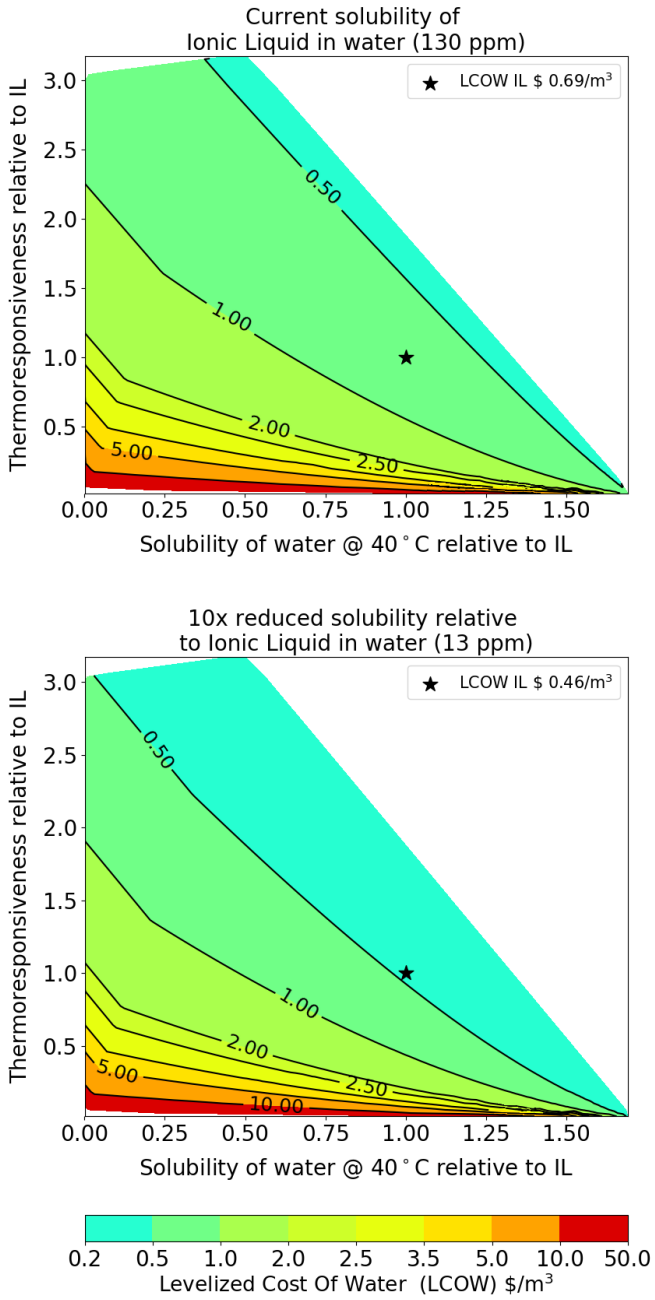

Figure 2.11. Sensitivity of LCOW (contours) assuming a cost of \$10/kg of [emim][Tf_2N]. (Top) With current solubility, either the thermoresponsivness needs to increase by 1.7-fold or the solubility of water needs to increase by 1.3-fold to decrease the LCOW from \$0.69/m^3 ($\star$) to the \$0.50/m^3 target. (Bottom) With a 10-fold reduction of the solubility of the solvent in water, we predict a LCOW of \$0.46/m^3 ($\star$) without improving thermoresponsivness or the solubility of water in the DS.

2.6 Conclusions and Future Work

Directional solvent extraction is a membrane-free desalination technology that can treat high salinity water resources using low-grade heat. DSE can be paired with other technologies, e.g., renewable solar thermal collectors, to create hybrid sustainable systems. In this work, we created a computational framework that facilitates the optimization of the process and rapid sensitivity analysis. Through these analyses, we found that higher maximum temperatures enable higher per pass extraction, which allows for a lower recycle flowrate and lower energy intensity. For solvent selection, we found that the length of the carbon chain has no apparent influence and that the most critical factors are the change in water solubility for a low-temperature swing (40°C-80°C), the melting temperature of the fatty acid, which limits the minimum operating temperature and the solubility of DS in freshwater. Technoeconomic optimization was performed for five candidate fatty directional solvents ranging, giving LCOW predictions between \$1.3/m^3 and \$109/m^3. Sensitivity analysis shows significant improvements in three solubility properties are needed for the hypothetical fatty acid-like DS to achieve less than \$0.5/m^3. In contrast, ILs show much greater promise as directional solvents. Using newly published data from [emim][Tf_2N] and assuming a moderate solvent price of \$100/kg, we predict a modest \$2.65/m^3 LCOW. Sensitivity analysis shows the required combination of thermophysical properties necessary to achieve LCOW to below \$0.5/m^3. These results emphasize the potential of IL directional solvents to desalinate high salinity water, which is currently challenging with existing technologies.

As future work, we plan to set quantitive thermophysical property targets over a wide-range of feed salinity conditions, which will better characterize the potential competitive advantage of DSE versus other desalination technologies. We also plan to explore process intensification opportunities (stage configuration, nanofiltration for solvent loss, electrocoalescer) and consider more detailed equipment models (nanofil-

tration to recovery solvent, electrocoalescer to replace settling tanks). Computer-aided molecular design (CAMD) approaches [14, 57, 105] offer promise to systematically search the billions of possible ionic liquids or other solvent chemistries. We ultimately see computational molecular, and process scale modeling greatly accelerate the search for economically viable directional solvents. We also plan to explore the opportunities and costs of coupling DSE with inexpensive solar heating for sustainable and distributed desalination.

CHAPTER 3

WHAT DATA ARE MOST VALUABLE TO SCREEN IONIC LIQUID ENTRAINERS FOR HYDROFLUOROCARBON REFRIGERANT REUSE AND RECYCLING?

This chapter is based on work currently under review:

A. Garciadiego, B. J. Befort, G. Franco, M. Mazumder, and A. W. Dowling. What Data Are Most Valuable to Screen Ionic Liquid Entrainers for Hydrofluorocarbon Refrigerant Reuse and Recycling? *ChemRxiv.* doi:10.26434/chemrxiv-2022-b60nn. Cambridge: Cambridge Open Engage; 2022. (*Under Review*)

3.1 Introduction

Due to their high ozone depletion potential, chlorofluorocarbon (CFC) refrigerants were phased out under the 1987 Montreal Protocol and replaced by their close molecular relative, hydrofluorocarbons (HFCs), which had similar excellent refrigeration properties. However, more recently, many of these second generation HFC refrigerants have been shown to have high global warming potentials (GWPs), caused by their ability to block infrared radiation[93] and extended atmospheric lifetimes, ranging from five to forty-seven years[36, 153]. In fact, 2019 United States (US) industrial HFC emissions accounted for more than 175 million metric tons of carbon dioxide equivalents in the atmosphere[50]. This alarming environmental impact has sparked renewed global concern resulting in fresh mandates for environmentally detrimental refrigerant phase out. For example, the 2016 Kigali Amendment[142] to the Montreal

Protocol aims to cooperatively achieve an 85% reduction of HFC use by 2036 among industrialized countries. The American Innovation and Manufacturing (AIM) Act of 2020[51] authorized the U.S. Environmental Protection Agency (EPA) to limit HFC production to 15% of the present values by 2036[51]. In addition to environmental incentives, the EPA estimates this future reduction of fluorinated gas emissions can have an annual social benefit of up to $2.8 billion [49]. Also important to consider is the huge economic value of HFCs. For example, there are approximately 100 million kilograms of HFC-32, a low GWP HFC used in many refrigerant mixtures, in global circulation worth around half a billion dollars[38].

The combined environmental, social, and economic impact of HFC refrigerants makes it imperative to develop a sustainable path forward for their phaseout. Fortunately, there remain new opportunities to reuse low GWP HFCs, either as pure refrigerants[38] or in next generation refrigerant mixtures[29], and recycle high GWP HFCs into new products. However, complicating this phaseout and transition to more environmentally-friendly chemicals is the fact that most refrigerants are manufactured and deployed as azeotropic mixtures of HFCs. While this azeotropic nature creates an ideal refrigerant with a single boiling point that will not separate in a leak, conventional technologies, i.e., distillation, become impractical when separating the components of these mixtures at the end of their utility.

Ionic liquid (IL) entrainers can effectively separate HFC mixtures, overcoming the energy costs of traditional separation technologies[83, 84, 127]. Over the past eighteen years, IL and HFC systems have been studied in a variety of contexts including the characterization of their individual and mixture physical properties[87, 88, 89, 132, 133, 130, 131, 134, 157, 158, 159] and their use in extractive distillation, membrane, and adsorption separation processes[84]. More recent work has used data generated from these studies to regress thermodynamic models then perform process design, optimization, technoeconomic analyses, and life cycle assessments for IL-enabled HFC

separation schemes[127, 55, 102, 58]. However, because millions of theoretical ILs are available, each with unique properties, trial-and-error molecular and process design is intractable since each HFC within a refrigerant blend exhibits a different boiling point and solubility with an IL[115]. This necessitates a framework which integrates experiments, mathematical models, and computational optimization to concurrently design ILs and separation processes for azeotropic HFC refrigerant mixtures. Thus, several opportunities remain to explore the intersection between IL discovery and design, thermophysical property measurements, and process engineering.

Here, we integrate published HFC/IL solubility data and process systems engineering approaches to answer the question: *what data are most valuable to screen IL entrainers for HFC reuse and recycling?* We investigate the use of first-of-their-kind thermophysical property measurements of ternary mixtures of HFCs and ILs, i.e., two HFCs mixed with an IL[15], within an HFC separation process design framework, determining how to best incorporate these new measurements to effectively screen ILs for use as entrainers. This enables us to begin to bridge the gap between experimental thermophysical property characterization, which is often driven by scientific goals, and process design decisions, which are guided by engineering principles, by addressing the following questions:

- What is the best way to use the new HFC/IL ternary mixture data to accelerate the design of HFC separation systems and the screening of IL entrainers?
- What is the uncertainty in property predictions for regressed thermodynamic models using various types of HFC/IL mixture data (e.g., binary versus ternary mixture data at single versus multiple temperatures)? How does this uncertainty propagate through process design calculations?
- What experimental precision for HFC/IL mixture data is sufficient to screen IL entrainers?

We propose an open-source, equation-oriented modeling framework to rapidly translate HFC/IL mixture data into regressed thermodynamic models for rapid IL

screening. In contrast to prior work, this framework propagates uncertainty in experimental data to process-level physical properties. This allows us to evaluate precision between experimental measurements versus model predictions, providing the opportunity to systematically guide laboratory and simulation experiments on the data types and accuracy that are needed for HFC separation process design and IL screening.

3.2 Literature rReview

3.2.1 Azeotropic distillation process design and entrainer screening

Separating mixtures with very close boiling points, such as azeotropic HFC mixtures, using conventional distillation requires a large number of trays, making the separation energy intensive and uneconomical[95]. To overcome this challenge, azeotropic and extractive distillation schemes have been used to separate these types of mixtures for more than 90 years[84]. Introducing an entrainer, i.e., a mass separating agent, to a close-boiling mixture creates a new mixture comprised of the entrainer and one of the original azeotropic mixture components. This new mixture, which may form its own azeotrope, has a different boiling point, breaking the original azeotrope to allow separation[116]. Techniques to identify ideal entrainers include using the molecular structure [24], residue curve maps[114], volatilities[86], process simulations[34], and entrainer selection rules developed by Rodrıguez-Donis *et al.* [121]. Yet, the search for entrainers is challenging and time consuming. For example, optimization of entrainers for separating water and ethanol has been ongoing since the 1930s[149, 61, 118]. However, for HFC systems especially, environmental regulations and global economics necessitate rapid innovation within the next decade.

3.2.2 Ionic liquids as entrainers

ILs are generally defined as organic salts with melting points below 100°C that are soluble with a wide range of organic compounds[54, 94]. ILs exhibit many traits which make them ideal entrainers. For example, ILs have tunable structure-property relationships such that the cation and anion which comprise the molecule can be selected from among a variety of options to achieve a specific chemical purpose. ILs have negligible vapor pressure which leads to easy recovery and essentially no contamination of products within a separation scheme, allowing ILs to be recycled in a separation process, reducing material demands and improving the separation economics[163]. ILs also have been shown to have excellent ability to separate a wide range of azeotropic and close-boiling mixtures[74, 127, 165, 145]. Other convenient properties of ILs include their existence in a liquid state over a wide temperature range and their high thermal and chemical stability[85, 162, 164, 125]. Since the feasibility of using ILs in extractive distillation schemes[83, 84] was shown in the early 2000s, many studies have evaluated their properties in mixtures with fluorinated refrigerants[87, 88, 89, 132, 133, 130, 131, 134, 157, 158, 159] and examined their use in HFC separations[127, 55]. ILs have also been the subject of computer-aided molecular design research, which has aimed to take advantage of their tunability to simultaneously design IL entrainers and optimize the separation processes in which they are used[112, 122].

3.2.3 Regression of thermodynamic models

Because equations of state (EoS) are continuous and differentiable functions, they are well-suited for computer-aided process design and optimization[42, 41, 43]. EoS models, including van der Waals[160, 103], Peng-Robinson[16], Redlich-Kong[130, 131], and soft-SAFT EoS[12], have been shown to reliably predict thermodynamic properties of HFC and IL mixtures. Yet, many of these models include parameters

which must be calibrated from data before they are used in process design. These parameters are often fitted using a minimizing least-squares approach [60, 59] involving the pressure of the system[160, 103, 130, 131, 16]. However, different objective functions, such as those involving liquid or vapor compositions, can be utilized in practice and may provide different parameter values[79].

There is a rich history of nonlinear parameter estimation within the chemical engineering discipline and, more specifically, thermodynamics community. It is well known that EoS parameter estimation is a nonconvex optimization problem and local optima are common and either multi-start initialization or rigorous global optimization methods are recommended[37, 53, 59, 11]. Besides local minima, spurious solutions are another key challenge for EoS calibration. Common mitigation strategies include bilevel optimization methods[28, 101], branch and bound methods[11], or the addition of penalty terms to the optimization problem[161]. Post regression tests can be implemented, including the Gibbs tangent plane method[100], which enforces a stable solution of the phase equilibrium problem if and only if the tangent plane lies below the Gibbs free energy surface for all compositions.

Once parameterized, EoS models are used for process design and optimization, yet thermodynamic model parameterization is often one of the most significant sources of uncertainty and risk in process design. For example, Hajipour and Satryo[64, 65] show how underestimating critical temperature by 2% while fitting binary interaction parameters may produce errors of 20% to 60% in vapor pressure predictions for petroleum engineering systems. However, out of the numerous thermodynamic modeling studies for HFC/IL systems, we are aware of only two papers, co-authored by us, which investigate EoS parameter uncertainties. In Morais *et al*[103], we use Monte Carlo techniques to calculate the uncertainty of parameters for the van der Waals EoS and describe the apparent over-parameterization of the model due to observed parameter sloppiness. In Baca *et al*[15], we report and interpret the covari-

ance matrix of estimated Peng-Robinson EoS parameters. However, there remains a need to understand how these uncertainties impact separation process design and IL screening decisions, which is a key contribution of this work.

3.3 Methods

To address the aforementioned gap, this paper presents an equation-oriented modeling framework to systematically translate binary or ternary vapor-liquid equilibrium (VLE) data into regressed thermodynamic and process models for rapid IL screening. Figure 3.1 depicts the workflow, which starts by specifying the system VLE data (Step 1) and EoS model (Step 2), which are inputs for parameter estimation (Step 3). The parameterized models are then used to make phase predictions (Step 4) and generate process designs, specifically flash calculations in this work (Step 5). Additionally, we use these parameters to calculate the pressure of the mixture to compare the quality of fit of our models (Step 6). Finally, ILs are screened for their HFC separations ability via a comparison of HFC relative volatility in the IL entrainer (Step 7) and uncertainty analysis is performed to inform experimental design (Step 8). The framework leverages tools from the open-source Institute for the Design of Advanced Energy Systems (IDAES) Integrated Platform[82] and the Pyomo Python library [31, 68]. Utilizing these open-source packages for modeling and optimization facilitates validation, reproducibility, and accountability, and allows for easy extension of the framework to other systems.

As a case study, we apply this workflow to screen six ILs for the separation of HFC-32 and HFC-125, which comprise the refrigerant R-410a. The remainder of this section describes the individual steps of the workflow.

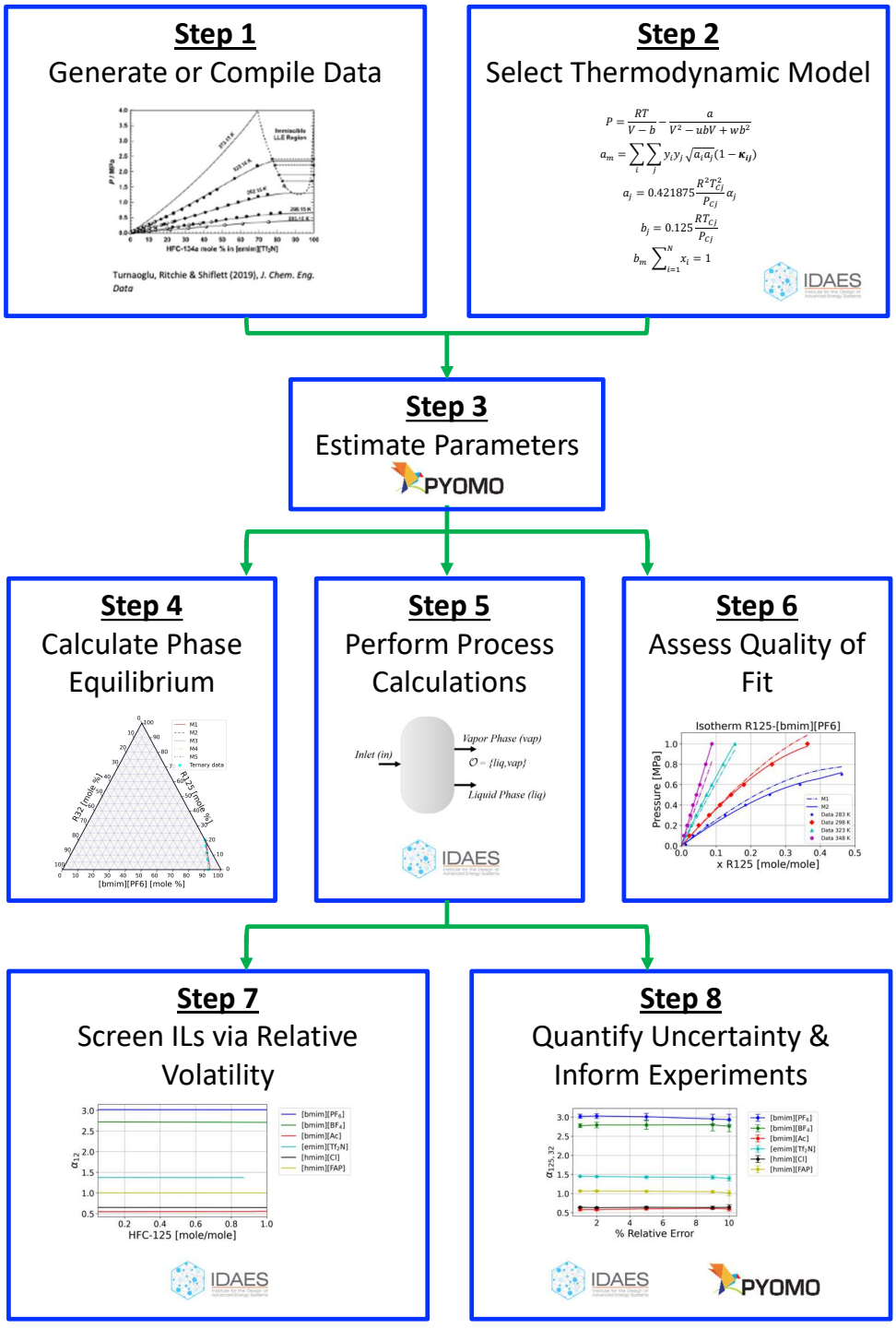

Figure 3.1. Open-source, equation-oriented modeling framework for HFC separation process design and IL entrainer screening.

3.3.1 Step 1. Generate or compile data

Based on previous studies from Morais *et al.* [103] and Baca *et al.* [16, 15], three types of data are considered in this work:

1. Binary HFC/IL solubility data for HFC-32 or HFC-125 in [bmim][PF_6], [bmim][BF_4], [emim][TF_2N], [bmim][Ac], [hmim][Cl], and [hmim][FAP] collected with a gravimetric microbalance[133, 131, 103, 16].
2. HFC-32/HFC-125 binary equilibrium data collected with gas chromatograph equipped with a flame ionization detector[67].
3. Ternary mixture data for HFC-32 and HFC-125 in [bmim][PF_6] and [bmim][BF_4] collected from XEMIS and IGA gravimetric microbalances with the integral mass balance method[15].

3.3.2 Step 2. Select thermodynamic model

3.3.2.1 Peng-Robinson EoS

We correlate experimental data utilizing the Peng-Robinson EoS:

$$P = \frac{RT}{V-b} - \frac{a_m}{V^2 - 2b_m V - b_m^2} \tag{3.1}$$

where pressure P is a function of temperature T, volume V, and the intermediate variables a_m and b_m. The substance-specific parameters a_j and b_j for each component j are calculated with:

$$a_j = 0.421875 \frac{R^2 T_{c,j}^2}{P_{c,j}} \alpha_j \tag{3.2}$$

$$\alpha_j = \left(1 + (1 - T_r^2)(0.37464 - 1.54226\omega_j - 0.26992\omega_j^2)\right)^2 \tag{3.3}$$

$$b_j = 0.125 \frac{RT_{c,j}}{P_{c,j}} \tag{3.4}$$

where R is the ideal gas constant, P_c and T_c are the pressure and temperature, respectively, at the critical point, and ω_j is the acentric factor. a_m and b_m are

calculated with the mixing rule recommended for cubic EoS [119]:

$$a_m = \sum_i \sum_j y_i y_j \sqrt{a_i a_j}\,(1 - \kappa_{i,j}(T)) \tag{3.5}$$

$$b_m \sum_{i=1}^{N} x_i = 1 \tag{3.6}$$

where $\kappa_{i,j}$ is the binary interaction parameter function:

$$\kappa_{i,j}(T) = \kappa_{Ai,j} + \kappa_{Bi,j} \cdot T \tag{3.7}$$

Specifying $\kappa_{Bi,j} = 0$ removes the temperature dependence for Eq. (3.7).

3.3.2.2 Regressed models

To study the differences between the use of different combinations of binary and ternary data sets, as well as to study the influence of temperature on fitted parameters in Eq. (3.7), we postulate five combinations of fitting data sets and models for comparison:

- M_B: EoS parameterized with binary data without binary interaction temperature dependence, i.e., $\kappa_{Bi,j} = 0$.
- $M_{B,K}$: EoS parameterized with binary data taking into account binary interaction temperature dependence.
- M_T: EoS parameterized with ternary data without binary interaction temperature dependence, i.e., $\kappa_{Bi,j} = 0$.
- M_{BT}: EoS parameterized with binary data and ternary data without binary interaction temperature dependence. Data are weighted based on the number of observations in each data set and normalized by the average pressure.
- $M_{BT,K}$: EoS parameterized with binary data and ternary taking into account binary interaction temperature dependence. Data are weighted the same as for M_{BT}.

Here, the subscript B denotes a model was parameterized with binary data, the sub-

TABLE 3.1

POSTULATED MODELS TO PREDICT HFC/IL PHASE EQUILIBRIUM

Model	$\kappa_{Bi,j}$	**Binary data**	**Ternary data**
M_B	0	Yes	No
$M_{B,K}$	Optimized	Yes	No
M_T	0	No	Yes
M_{BT}	0	Yes	Yes
$M_{BT,K}$	Optimized	Yes	Yes

script T denotes the model was parameterized with ternary data, and the subscript BT indicates a model was parameterized with both binary and ternary data. The subscript K (for Kelvin) denotes a temperature dependence of the binary parameters, i.e., $\kappa_{Bi,j}$ was calibrated. Table 3.1 compactly summarizes the models.

3.3.3 Step 3. Estimate parameters

Nonlinear least-squares optimization was performed in `Pyomo` using `parmest`[76] to calculate the binary parameters κ via Eq. (3.5):

$$\begin{aligned} \min_{\kappa^l \leq \kappa \leq \kappa^u} \quad & \sum_{d=1}^{D} \left[\frac{w_d}{n_d} \sum_{i=1}^{n_d} (\hat{P}(\kappa, T_{i,d}, x_{i,d}) - P_{i,d})^2 \right] \\ \text{s.t.} \quad & \text{Eqs.} \quad (3.1) - (3.10) \end{aligned} \tag{3.8}$$

Here P_i is the experimentally measured pressure value, $\hat{P}$ is the model prediction of pressure, D is the total number of data sets, n_d is the number of observations in data set d, and the weight w_d is the average pressure of the data set. Minimizing the least-squares error of the calculated pressure $\hat{P}$ and experimental pressure P is consistent with prior literature on EoS calibration for IL and HFC mixtures[160, 103, 130, 131].

The model is constrained by Eqs. (3.1) to (3.10). With $D = 1$ and $n = 32$,where n is the number of fitted points $n = \sum_{d=1}^{D} n_d$, the model contains 434 variables and 432 equality constraints for the case in which only $\kappa_{Ai,j}$ is fit. We can estimate parameters for the full [bmim][PF_6] data set using IPOPT[147] solver and HSL (MA27)[1] in approximately 30 seconds with thoughtfully chosen initial parameter values. The bounds κ^l and κ^u were set to -3 and 3, respectively. In all obtained optimal solutions these bounds were not active.

Alternatively, we can estimate the parameters by minimizing the least squares error of the composition:

$$\begin{aligned} \min_{\kappa^l \leq \kappa \leq \kappa^u} \quad & \sum_{d=1}^{D} \left[\frac{w_d}{n_d} \sum_{i=1}^{n_d} (\hat{x}(\kappa, T_{i,d}, P_{i,d}) - x_{i,d})^2 \right] \\ \text{s.t.} \quad & \text{Eqs.} \quad (3.1) - (3.10) \end{aligned} \tag{3.9}$$

Here $x_{i,d}$ is the experimentally measured liquid phase composition and, $\hat{x}(\kappa, T_{i,d}, P_{i,d})$ is the model prediction of the liquid composition. With $D = 1$ and $n = 32$ the model contains 434 variables and 432 equality constraints for the two-parameter $\kappa_{Ai,j}$ system. We can estimate parameters for the full [bmim][PF_6] data set using IPOPT[147] solver and HSL (MA27)[1] in approximately 31 seconds. Although both formulations are computationally tractable, Eq. (3.8) is predominatenly used in previous IL literature[160, 103, 130, 131, 15]. To be consistent, Eq. (3.8) is used throughout the remainder of the analysis.

3.3.4 Step 4. Calculate phase equilibrium

We use the *phi-phi* method[109] to calculate VLE at temperature T_{eq}:

$$\Phi_{vap,i}(T_{eq}) = \Phi_{liq,i}(T_{eq}) \tag{3.10}$$

Here the Peng-Robinson EoS is used to calculate the fugacities of both phases, $\Phi_{vap,i}$ and $\Phi_{liq,i}$[30]. However, Eq. (3.10) is only valid in the two-phase region. It is relaxed as follows as part of the smooth flash formulation[30]:

$$T_1 = \max(T_{bubble}, T) \tag{3.11}$$

$$T_{eq} = \min(T_1, T_{dew}) \tag{3.12}$$

where T_1 is an intermediate variable, and T is the outlet temperature. Thus if $T < T_{bubble}$, then the VLE is calculated at T_{bubble}. Likewise if $T > T_{dew}$, then the VLE is calculated at T_{dew}. The calculation is reformulated with smooth min and max operators to improve numerical performance with derivative-based equation solving and optimization algorithms.

$$T_1 = 0.5\big[T + T_{bubble} + \sqrt{(T - T_{bubble})^2 + \epsilon_1^2}\big] \tag{3.13}$$

$$T_{eq} = 0.5\big[T + T_{dew} + \sqrt{(T - T_{dew})^2 + \epsilon_2^2}\big] \tag{3.14}$$

where $\epsilon_1 = 0.01$ and $\epsilon_2 = 5.0 \times 10^{-5}$ are smoothing parameters[30].

3.3.5 Step 5. Perform process calculations

Shiflett and Yokozeki[127] presented an extractive distillation flowsheet uses an IL entrainer to separate R-410A, which is a 50/50 mol% mixture of HFC-32 and HFC-125. In this extractive distillation column, HFC-125 is the top product and HFC-32 and the IL are the bottom products. The HFC-32 and IL mixture is then sent to the recycling section of the flowsheet with two sequential flash vessels to separate HFC-32 from the IL entrainer. The IL is then recycled to the extractive distillation column. The first vessel is operated at 0.1 MPa and 371 K. With a feed composition x_{in} of 21.6 mol% of HFC-32, 0.3 mol% of HFC-125, and 78.1 mol% of [bmim][PF_6][127].

We simulate this flash vessel to illustrate the impact of data and model uncertainty on process modeling calculations. The flash is modeled as follows:

$$F_{in} = \sum_{l \in \mathcal{O}} F_l \tag{3.15}$$

$$F_{in} x_{in,c} = \sum_{l \in \mathcal{O}} F_l x_{l,c}, \quad \forall c \in \mathcal{C} \tag{3.16}$$

$$\sum_{c \in \mathcal{C}} (x_{vap,c} - x_{liq,c}) = 0 \tag{3.17}$$

Eq. (3.15) is a total mole balance that equates the inlet total molar flowrate, F_{in}, with the sum of the outlet, F_l. Eq. (3.16) is the component balance and equates the product of the inlet flow F_{in} and the inlet composition $x_{in,c}$ of a component c to the sum of the flow of the outlet streams F_l and the mole fraction $x_{l,c}$ of component c in the outlet streams l. Finally, Eq. (3.17), commonly known as the Rachford–Rice equation, ensures the sum of the differences between vapor and liquid fractions of the components, $x_{vap,c}$ and $x_{liq,c}$, must be equal to zero.

3.3.6 Step 6. Assess quality of fit

We utilize the mean absolute percent error (MAPE) metric to quantify the fit and the accuracy of our model predictions:

$$MAPE = \sum_{d=1}^{D} \left[\frac{1}{n_d} \sum_{i=1}^{n_d} \left| \frac{\hat{P}(\kappa, T_{i,d}, x_{i,d}) - P_{i,d}}{\hat{P}(\kappa, T_{i,d}, x_{i,d})} \right| \right] \tag{3.18}$$

Here we compare the accuracy of the calculated pressure $\hat{P}$ and experimental pressure P, normalizing by the number of observations n_d in data set d for all the data sets D. We calculate two types of MAPE: in-sample, which corresponds to data used for parameter calibration, and out-of-sample, which corresponds to data not used for the parameter calibration.

3.3.7 Step 7. Screen ILs via relative volatility

Relative volatility is a good indicator of an IL's potential as an entrainer and is a popular screening metric[86]. We screen prospective ILs by calculating the relative volatility, $\alpha_{i,j}(T, P, x_{in})$, for species i relative to species j at different compositions of the species:

$$\alpha_{i,j} = \frac{y_i/x_i}{y_j/x_j} \tag{3.19}$$

Here, x_i and x_j are the predicted molar compositions of the liquid phase in the flash calculation, and y_i and y_j are the predicted molar compositions of the vapor phase. In this work, the relative volatility is calculated between HFC-32 and HFC-125 in a given IL.

3.3.8 Step 8. Quantify uncertainty to inform experiments

Finally, we quantify how experimental measurement uncertainty impacts relative volatility and similar calculations. We utilize two different uncertainty quantification methods: Monte Carlo sampling and bootstrap re-sampling. Algorithm 1 describes our Monte Carlo approach, a standard method for uncertainty quantification and propagation[99, 144]. The main idea is to simulate experimental uncertainty by adding normally distributed noise ϵ to the experimental composition. We choose to add this uncertainty to the compositions, as pressure and temperature are easier to control in laboratory experiments. We then resolve the flash calculation utilizing the newly regressed parameters and propagate this error to $\alpha_{i,j}$. Alternatively, we used `Parmest` bootstrap re-sampling of the data to quantify uncertainty. We eliminate two data points randomly, estimate the parameters, then re-sample and repeat the process to estimate the binary parameters. We draw 50 bootstrap samples from the data, with n-2 samples. For each instance of regressed parameters, the relative volatility

is computed. The key distinction between these approaches is that for Monte Carlo we must specify the measurement noise probability distribution; in contrast, with bootstrap, the measurement uncertainty is implicitly inferred from the data.

Algorithm 1 Monte Carlo Uncertainty Analysis

1: **for** $\epsilon = 1$–10% proportional to experimental composition **do**
2: **for** *iteration* $= 1, 2, \ldots, 100$ **do**
3: Add noise proportional to experimental composition, $x_{i,d}^{\epsilon} \leftarrow \mathcal{N}(x_{i,d}, x_{i,d} \cdot \epsilon)$
4: Enforce composition bounds of 0 and 1
5: Estimate parameters via Eq. (3.8) using $x_{i,d}^{\epsilon}$
6: Perform flash calculation via Eq. (3.15) –(3.17)
7: Calculate relative volatility via Eq. (3.19)
8: Store results
9: **end for**
10: Calculate and store average volatility
11: Calculate and store volatility standard deviation
12: **end for**
13: Plot the mean of the volatility and standard deviation vs. error %

3.4 Results

3.4.1 Peng-Robinson EoS accurately describes HFC/IL binary solubility data behavior

We begin our analysis by comparing the parameter regression results for the five postulated models. In Figure 3.2, we compare the predictions of solubility isotherms of HFC-32 and HFC-125 in [bmim][PF_6] as a function of composition computed using the regressed values for $\kappa_{i,j}$ with experimental binary solubility isotherm data. Table 3.2 shows the regressed parameters for the [bmim][PF_6] system. To assess the quality of fit, in Step 6, we utilize Eq. (3.18) to calculate the in-sample MAPE.

TABLE 3.2

BINARY INTERACTION PARAMETERS FOR THE FIVE POSTULATED MODELS FOR HFC-32 OR HFC-125 SOLUBILITY IN [BMIM][PF_6]

Model	M_B	$M_{B,K}$	$M_{B,K}$	M_T	M_{BT}	$M_{BT,K}$	$M_{BT,K}$
Parameter	$\kappa_{Ai,j}$	$\kappa_{Ai,j}$	$\kappa_{Bi,j}$	$\kappa_{Ai,j}$	$\kappa_{Ai,j}$	$\kappa_{Ai,j}$	$\kappa_{Bi,j}$
i = **HFC-32**, j = **[bmim][PF_6]**	-0.0261	0.0270	-0.0488	-0.0435	-0.0328	-0.0248	-0.0056
i = **[bmim][PF_6]**, j = **HFC-32**	-0.0704	0.2680	-0.3153	-0.3506	-0.1131	-0.0106	-0.0910
i = **HFC-125**, j = **[bmim][PF_6]**	0.0589	-0.1114	0.1703	0.0604	0.0595	-0.1612	0.2123
i = **[bmim][PF_6]**, j = **HFC-125**	0.3454	-1.6016	2.0860	1.6779	0.4138	-1.7646	2.1235
i = **HFC-32**, j = **HFC-125**	0.0093	0.3926	-0.3891	0.0093	0.0093	0.3926	-0.3891
i = **HFC-125**, j = **HFC-32**	0.0074	-0.3754	0.3892	0.0074	0.0074	-0.3754	0.3892

We first compare the models calibrated only using experimental binary solubility data (M_B, $M_{B,K}$). Figure 3.2(a) and 3.2(b) shows the pressure predictions of the models M_B and $M_{B,K}$ compared to the experimental data. We observe that the fit is more accurate at lower concentrations of the HFCs. For HFC-32/[bmim][PF_6], we calculate an in-sample MAPE between predicted and experimental pressures of 7% for M_B and 5% for $M_{B,K}$. We also observe that for HFC-125/[bmim][PF_6], the fit is considerably better for $M_{B,K}$ at 7% MAPE, as it accounts for temperature dependency for binary parameters, compared to a MAPE of 15% for M_B. We find the binary parameters are more dependent on temperature in the HFC-125/[bmim][PF_6] system than HFC-32/[bmim][PF_6] system. We hypothesize that temperature dependence is necessary because of the concave shape of the HFC-125 isotherm. We emphasize that the temperature dependence shown in Eq. (3.7) can only be regressed with data sets that contain measurements at two or more temperatures.

Next, we compare the models that are calibrated using only experimental ternary

solubility data (M_T) and both experimental binary and ternary solubilty data (M_{BT}, $M_{BT,K}$). Figure 3.2(c) and 3.2(d) shows that model M_T, calibrated only with experimental ternary solubility data has an out-of-sample MAPE of at least 30% when predicting solubility for binary HFC/IL systems. This is explained by two different features of the experimental ternary solubility data set. The first is that the data set contains only two binary HFC/IL data points for each HFC, one at each of the two experimental pressures. In other words, the experimental ternary solubility data set includes an HFC-32/IL data point at 0.1 MPa and an HFC-32/IL data point at 0.25 MPa, as well as two data points at the same pressures for HFC-125. Second, the availability of this experimental data at only two pressures and one temperature (298 K) necessitates extrapolation to higher pressures and different temperatures.

We calculate the in-sample MAPE between predicted and experimental pressures for HFC-32/[bmim][PF_6] as 7.5% for M_{BT} and 5.2% for $M_{BT,K}$. For HFC-125/[bmim][PF_6] the in-sample MAPE is 15.8% for M_{BT} and 7.4% for $M_{BT,K}$. We note that in-sample MAPE of the predicted pressure of M_B versus M_{BT} and $M_{B,K}$ versus $M_{BT,K}$ are almost identical, which is attributed to the exclusion or inclusion of temperature-dependent binary parameters. We can also observe from Table 3.2 the order of magnitude change in $\kappa_{Ai,j}$. M_{BT} and $M_{BT,K}$, calibrated with binary and ternary data, estimate binary solubility with higher accuracy than M_T, as the addition of binary data reduces the interpolation problem of M_T. None of the calibrated models using only ternary data or a combination of binary and ternary data, M_T, M_{BT}, and $M_{BT,K}$, have a significantly lower in-sample MAPE than M_B and $M_{B,K}$, the models calibrated only with experimental binary solubility data.

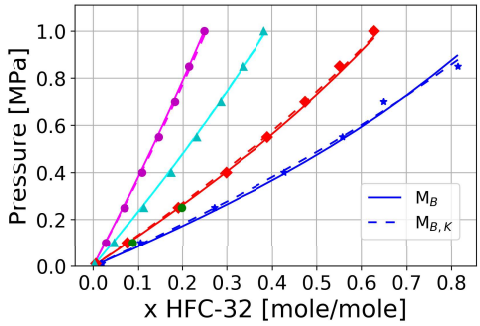

(a) Isotherms for HFC-32 solubility in [bmim][PF_6] predicted with M_B and $M_{B,K}$

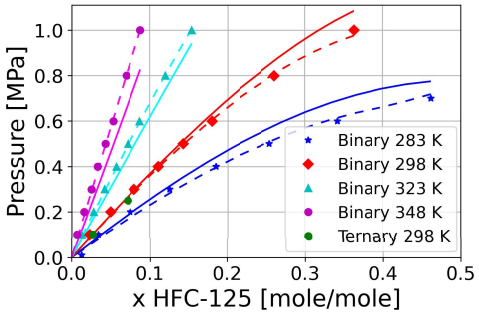

(b) Isotherms for HFC-125 solubility in [bmim][PF_6] predicted with M_B and $M_{B,K}$

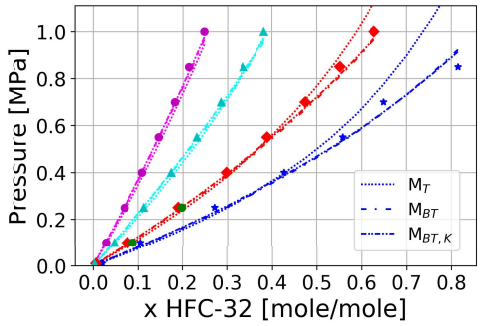

(c) Isotherms for HFC-32 solubility in [bmim][PF_6] predicted with M_T, M_{BT} and $M_{BT,K}$

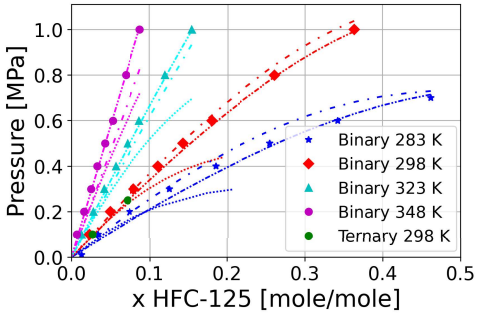

(d) Isotherms for HFC-125 solubility in [bmim][PF_6] predicted with M_T, M_{BT} and $M_{BT,K}$

Figure 3.2. Comparison of experimental solubility isotherms (points) and solubility predictions (dashed lines) made with models M_B (no κ temperature dependence, fitted to experimental binary data[133]), $M_{B,K}$ (κ temperature dependence, fitted to experimental binary data[133]), M_T (no κ temperature dependence, fitted to experimental ternary data[15]), M_{BT} (no κ temperature dependence, fitted to both experimental binary[133] and ternary data[15]) and $M_{BT,K}$ (κ temperature dependence, fitted to both experimental binary[133] and ternary data[15]).

3.4.2 EoS parameterized with binary or ternary data give accurate phase equilibrium predictions

Figure 3.3 compares ternary solubility predictions for models M_B to $M_{BT,K}$ against experimental ternary solubility of HFC-32/HFC-125/[bmim][PF_6] in a ternary phase diagram (Step 4) using the regressed parameters in Table 3.2. We calculate the vapor and liquid phase compositions with Eqs. (3.1) to (3.10) at 298 K and 1 MPa and compositions of the ternary mixture extracted from the ternary data set.

As expected, we find that the predictions utilizing M_T, which has no κ temperature dependence and was calibrated only with experimental ternary data, has a 1% in-sample MAPE. In contrast, we find that the predictions of M_B and $M_{B,K}$ (both models only calibrated with experimental binary solubility data) have an out-of-sample MAPE of 10.1% and 10.2%, compared to the ternary experimental compositions in Baca *et al.* [16]. The error is consistent with the difference observed between the data sets in Figure 3.3. We emphasize these measurements we obtained with different experimental methods and equipment (as described in the references), so a modest difference is to be expected.

Predictions made with models M_{BT} and $M_{BT,K}$ (models calibrated from both data sets) have an in-sample MAPE of 9.5% and 9.2%, respectively. The predictions are qualitatively consistent between models calibrated from experimental binary or ternary solubility data sets. The findings give us confidence in the EoS and provide a benchmark to compare the results of the binary prediction (see below). This significant result allows us to compare different IL behavior qualitatively as the ternary data now acts as an out-of-sample validation for the binary models M_B and $M_{B,K}$.

Similarly, Figure 3.4 shows the absorption of each HFC and the total absorption to the IL phase. We first note that the difference between the absorption predicted in both experimental data sets is consistent with the differences shown in Figure 3.2, i.e., the data sets have a better agreement with respect to HFC-32 than HFC-125. M_B

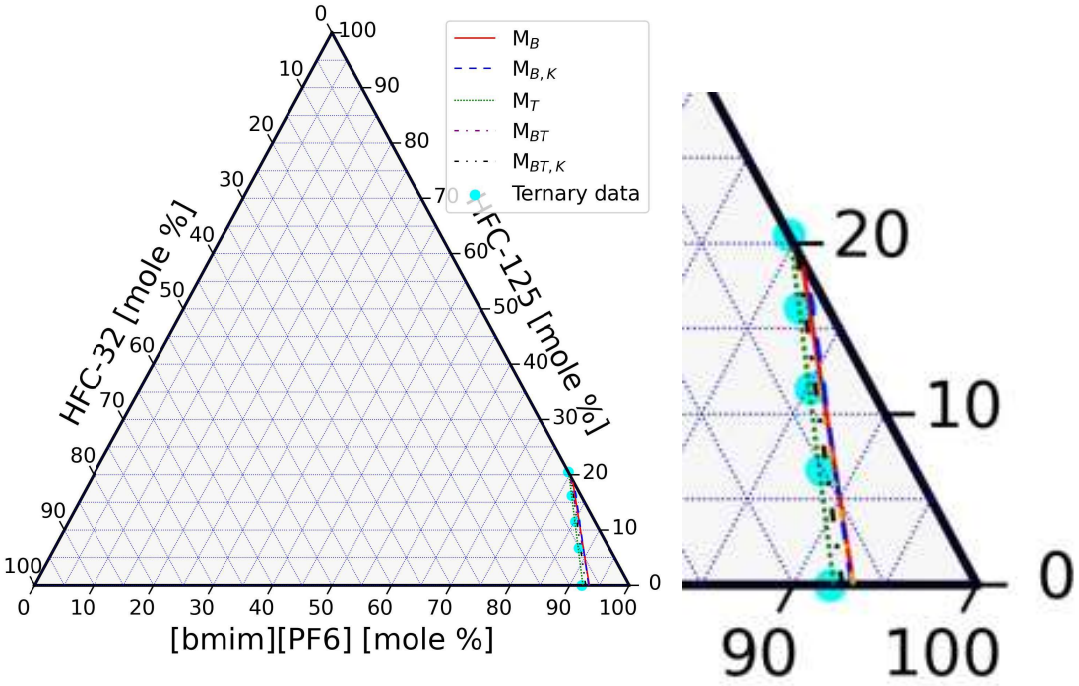

(a) Experimental and predicted liquid compositions for HFC-32/HFC-125/[bmim][PF_6] calculated utilizing M_B, $M_{B,K}$, M_T, M_{BT} and $M_{BT,K}$.

(b) A zoomed in look at the ternary composition results.

Figure 3.3. Ternary diagram liquid compositions calculated from two different data sets. M_B, $M_{B,K}$ were calibrated with binary data.

prediction is consistent with the binary data with a MAPE of 2.7%. However, $M_{B,K}$ prediction has a MAPE of 1% compared to the binary experimental data, consistent with the finding in the pressure prediction shown in Figure 3.2, as it accounts for the temperature dependency.

M_T gives an accurate prediction compared to the ternary experimental data, as it was calibrated with this data. In comparison, M_{BT} predicts approximately the average of the two data sets. We note how weighing the ternary data changes the behavior of the temperature dependence. $M_{B,K}$ predicted less absorption of HFC-32 than M_B while, $M_{BT,K}$ considers more absorption of HFC-32 than M_{BT}. This is explained by the addition in the weighted parameterization of the ternary data set, which contains more data at low pressures and 298 K. Although M_T predictions show the lower MAPE with respect to absorption, we caution against the use of the model at higher pressures: as shown in Figure 3.2(c) and 3.2(d), M_T does not have a good quality of fit at high pressures as it was only calibrated at a maximum of 0.25 MPa and 298 K.

3.4.3 Binary data and PR EoS models are sufficiently accurate to perform early process design and relative volatility estimation

We now quantify how the differences between the models M_B through $M_{BT,K}$ impact process design and IL screening calculations. We calculate a flash unit from Shiflett *et al.* [127] described in the Methods (Step 5), which is a proxy for the overall separation process design. In Figure 3.5, we systematically vary the outlet temperature from 280 K to 325 K to compare the predicted HFC-32 vapor recovery fraction. From the results, we observe a 4% to 20% difference between the vapor recovery fraction predictions from the models at low temperatures. The difference in models is consistent with Figure 3.4. M_B and $M_{B,K}$ show a maximum discrepancy of 10% of the vapor recovery fraction. Additionally, M_{BT} and $M_{BT,K}$ reconcile the

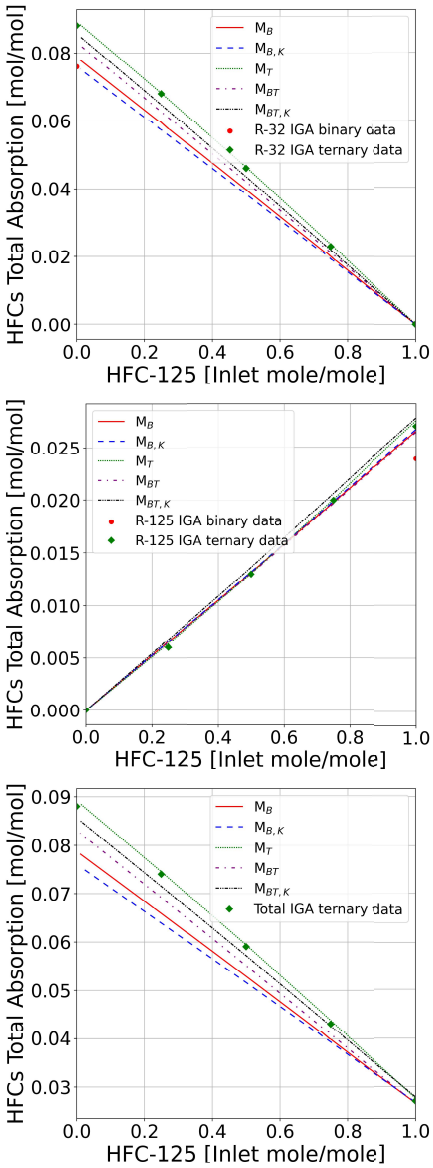

Figure 3.4. Predicted HFC-32/HFC-125/[bmim][PF_6] ternary absorption compared to experimental data from Baca *et al.* [15]. M_B and $M_{B,K}$ were only calibrated with experimental binary solubility data. M_T was calibrated with only with experimental ternary solubility data. M_{BT} and $M_{BT,K}$ where calibrated with both experimental binary and ternary solubility data.

models calibrated with binary data and M_T. The models that show the highest difference in predicted HFC-32 vapor recovery (20%) are $M_{B,K}$ and M_T. We also note that the flash vapor is enriched in HFC-32 (above 98 mol%), at which, as seen in Figures 3.2(a) and 3.2(c), M_T solubility predictions show a MAPE of only 5%. However, as shown in Figure 3.2(d), M_T should be used with caution when calculating equilibrium at pressures above 0.25 MPa and temperatures different than 298 K and in mixtures with concentrations of HFC-125 above 10 mol%. The fact that any of the models can qualitatively predict the vapor recovery fraction of the flash calculation shows that we can perform early process design with our models and one or both data sets. If multiple unique data sets are available, i.e., both binary and ternary solubility data, we recommend using the EoS model calibrated with the most data for process design. Leave-one-out (i.e., jackknife resampling) analysis can be used to estimate the out-of-sample prediction uncertainty which can be propagated through the process design analysis (as described below).

To determine if the qualitative results translate to relative volatility, we calculate the phase equilibrium of a 0 mol% HFC-125, 70 mol% HFC-32, and 30 mol% of [bmim][PF_6] mixture. We then increased the concentration of HFC-125 by 5 mol% and reduced the HFC-32 by the same amount until 70 mol% of HFC-125 had been reached and recalculated the relative volatility. We do this for all the models and plot the results in Figure 3.6. We observe the same qualitative trend of 2.8 to 3.4 relative volatility consistent across all the models, as the flash calculation results shown in Figure 3.5. We note the experimental relative volatility was calculated with ternary data and, as a consequence, M_T gives the best relative volatility prediction because it was calibrated with the same ternary data. However, these results suggest that M_B, the simplest model, is sufficient for ranking ILs as candidate entrainers.

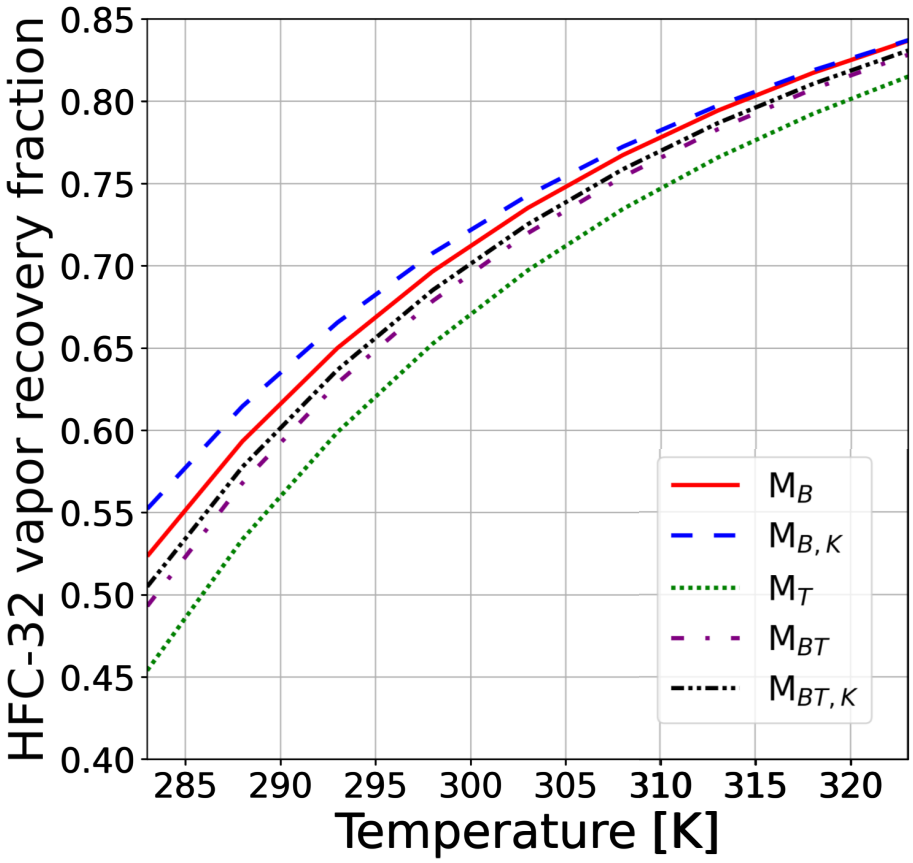

Figure 3.5. HFC-32 vapor phase recovery from [bmim][PF_6] versus temperature predicted with models M_B to $M_{BT,K}$.

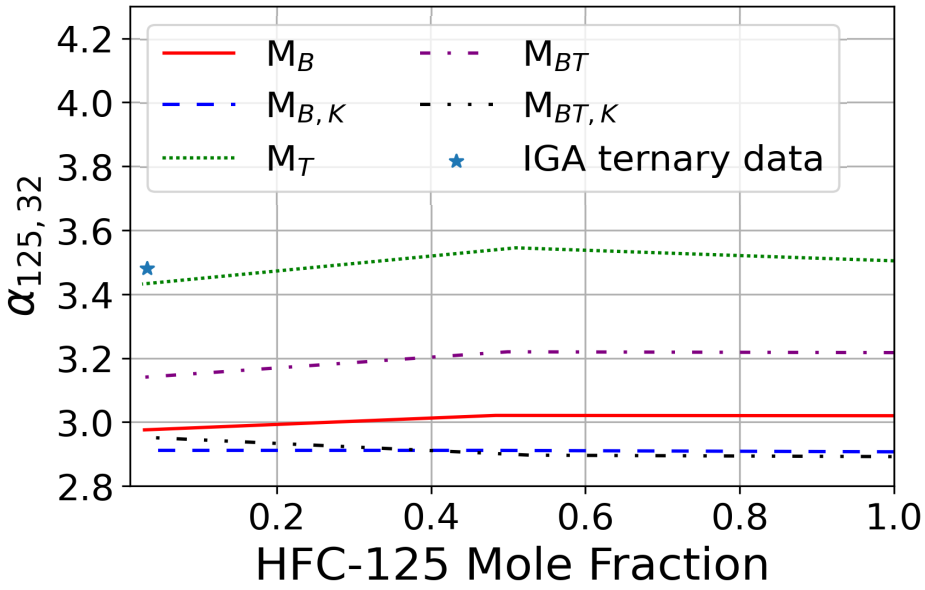

Figure 3.6. Relative volatility predictions for HFC-32 and HFC-125 in [bmim][PF_6] calculated with models M_B to $M_{BT,K}$.

3.4.4 The framework evaluates candidate IL entrainers in minutes

Ultimately, we envision using this framework to facilitate data-driven IL entrainer screening and selection (Step 7). To demonstrate this, we calculate the relative volatility of HFC-125 with respect to HFC-32 in six different ILs at varying liquid concentrations of HFC-125, shown in Figure 3.7(a). Visually, the relative volatility metric does not seem to vary with HFC-125 liquid composition. However, there is a 5% decrease in volatility as the HFC-125 liquid mole fraction increases, which is consistent across all of the six ILs studied. This result is on the same order of magnitude as findings from Li *et al.*[86] which showed that with a 30 mol% IL feed, relative volatility decreased by approximately 14% as the composition of the other mixture component changed. We hypothesize this small change in volatility as liquid HFC composition changes results from weak molecular-level interactions between HFCs in the liquid phase, i.e., if there were more interactions between the

liquid phase HFCs, there would be more significant relative volatility variations. This suggests that in the search for an IL entrainer, the focus should be given to ILs which interact more strongly with HFCs to prevent further HFC interactions. For IL screening, these results show that evaluating the relative volatility metric at a single composition is sufficient. These results guide us to select [bmim][PF_6] as the entrainer for separating R-410A from the set of ILs in this study. We note that even though the relative volatility is an essential factor in an HFC separation process, it is necessary to model other properties, such as the density, viscosity, and heat capacity of the ILs so that their impact on the economics of the process can be analyzed.

We profile computational times of the workflow using a Windows PC with Intel(R) Core(TM) i7-7500U CPU with 2.90 GHz and 16 GB of RAM. Overall, implementing the entire workflow to screen a single IL takes between 7 and 25 minutes, depending on the amount of available data and the thermodynamic model. The time requirements of Steps 1 and 2 is negligible. In Step 3, thermodynamic model parameter estimation, for a data set containing six data points (e.g., [bmim][Ac], [hmim][FAP], [hmim][Cl]), parameterization took two minutes, while for a data set containing sixty data points (e.g., [bmim][PF_6]), parameterization took twenty minutes. (The optimal parameters for each HFC/IL dataset are reported in Table 3.3). We believe there are opportunities to optimize the model initialization in IDAES-PSE and `parmest` to reduce this time significantly. Steps 4, 5, and 7, which are necessary for performing the relative volatility and screening analysis, took on average five minutes to complete. Thus, Step 3 is the most computationally demanding step of the workflow. We emphasize that this framework can be used for entrainer screening via other metrics, such as ternary diagram evaluation or selectivity analysis because phase equilibrium (Steps 4 and 5) can be computed in minutes. In total, we applied the complete framework to the six ILs in two hours, analyzing each IL sequentially. However, we note that the calculations in this workflow, which are independent for each IL, would

TABLE 3.3

BINARY INTERACTION PARAMETERS FOR MODEL M_B FOR HFC-32 OR HFC-125 SOLUBILITY IN VARIOUS ILS

IL	Model	Parameter	HFC-32/ IL	IL/ HFC-32	HFC-125/ IL	IL/ HFC-125	HFC-32/ HFC-125	HFC-125/ HFC-32
[bmim][BF_4]	M_B	$\kappa_{Ai,j}$	-0.0068	-0.0282	0.0645	0.5715	0.0093	0.0074
[bmim][Ac]	M_B	$\kappa_{Ai,j}$	-0.0254	-0.0313	-0.0214	-0.1105	0.0093	0.0074
[emim][Tf_2N]	M_B	$\kappa_{Ai,j}$	-0.0261	-0.0704	-0.0215	-0.1106	0.0093	0.0074
[hmim][Cl]	M_B	$\kappa_{Ai,j}$	0.0271	-0.2974	-0.0469	-0.0550	0.0093	0.0074
[hmim][FAP]	M_B	$\kappa_{Ai,j}$	-0.0254	-0.0155	-0.0418	-0.1354	0.0093	0.0074

be trivial to parallelize with multiple CPU cores or computers.

3.4.5 What experimental precision is adequate for IL screening?

To aid experimental design we estimate how measurement uncertainty impacts relative volatility calculations by applying the Monte Carlo and bootstrap algorithms (Step 8). In Figure 3.7(b), we plot the mean of the volatility calculated using M_B and the standard deviation versus the percentage of experimental error. Table 3 presents the mean and standard deviation of the regressed parameters, which are consistent using both uncertainty quantification techniques.

From Figure 3.7(b) and Table 3, we observe that a 5% error in experimental measurements translates 5% deviation in relative volatility. We also observe that the standard deviation is higher in systems where the volatility is higher and where data at different temperatures is available, as is the case for [bmim][PF_6] and [bmim][BF_4]. We observe that the error bars induced are more significant than the change in volatility compared to Figure 3.7(a). We note that the experimental precision required depends on the closeness of the volatilities of the mixtures and the type of data from

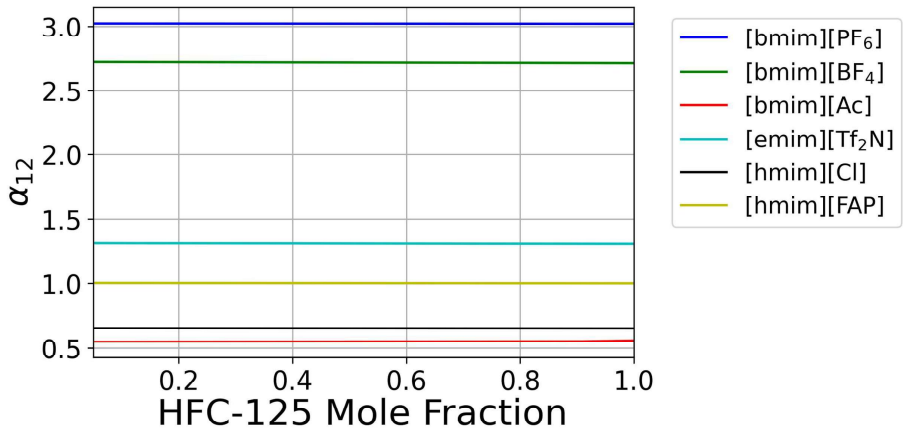

(a) Relative volatility calculate with experimental binary solubility data for HFC-32 and HFC-125 in six ILs.

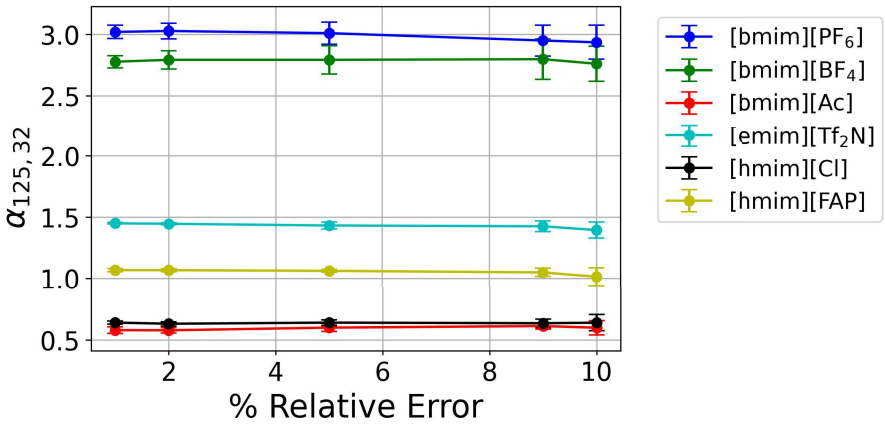

(b) Mean of the relative volatility versus relative error of the experimental data. Error bars are the standard deviation of the relative volatility.

Figure 3.7. Comparing the relative volatility of HFC-32 and HFC-125 in different ILs provides a qualitative reason for understanding which ILs may be optimal entrainers.

TABLE 3.4

UNCERTAINTY IN BINARY INTERACTION PARAMETERS FOR MODEL MONE FOR HFC-32 OR HFC-125 SOLUBILITY IN [BMIM][PF_6]

Model	**Stat**	$\mathbf{M}_B$ 1% error	$\mathbf{M}_B$ 2% error	$\mathbf{M}_B$ 5% error	$\mathbf{M}_B$ 9% error	$\mathbf{M}_B$ 10% error	$\mathbf{M}_B$ bootstrap
HFC-32/[bmim][PF_6]	mean	-0.0272	-0.0274	-0.0276	-0.0276	-0.0276	-0.0271
HFC-32/[bmim][PF_6]	standard dev.	0.0001	0.0004	0.0004	0.0006	0.0006	0.0022
[bmim][PF_6]/HFC-32	mean	-0.0781	-0.0757	-0.0751	-0.0724	-0.0724	-0.0886
[bmim][PF_6]/HFC-32	standard dev.	0.0007	0.0071	0.0139	0.0200	0.0201	0.0391
HFC-125/[bmim][PF_6]	mean	0.0584	0.0579	0.0534	0.0468	0.0470	0.0636
HFC-125/[bmim][PF_6]	standard dev.	0.0014	0.0019	0.0034	0.0043	0.0050	0.0074
[bmim][PF_6]/HFC-125	mean	0.3367	0.3331	0.3365	0.3320	0.3348	0.4941
[bmim][PF_6]/HFC-125	standard dev.	0.0163	0.0276	0.2338	0.2397	0.2440	0.2065

which the parameters are fitted. In the case of the ILs being compared in this study, only error values above 8% to 9% (when the error bars overlap) could change the decision from [bmim][PF_6] to [bmim][BF_4]. Recall, each error bar corresponds to one standard deviation in the relative volatility estimate. Thus the probability of experimental errors at the upper extreme for one IL candidate, e.g., [bmin][PF_6], and lower extreme for another, e.g., [bmin][BF_4], is low. Based on the results for these two ILs, we conclude a 10% experimental precision is adequate to rank ILs with a relative volatility difference of 0.3 ($\approx 3.03 - 2.74$ at 50 mol% HFC-125) based on Fig. 3.7(a). To our knowledge, this is one of the first studies to recommend a quantitative threshold for acceptable experimental error based on process metrics such as relative volatility for IL screening.

3.5 Conclusions and Future Work

We developed a data analysis toolkit, built upon the open-sourced IDAES-PSE framework and Pyomo ecosystem, to calculate the VLE of HFC and IL mixtures and then rapidly screen IL entrainers. The approach calibrates PR EoS binary interaction parameters to binary and first-of-their-kind ternary HFC and IL mixture data. We harness the fitted EoS to study phase predictions, flash calculations, and in-sample and out-of-sample error metrics. Next, relative volatility of HFCs is computed for IL screening. Finally, Monte Carlo and bootstrap methods are used to quantify and propagate uncertainty in the data and EoS models through process design calculations and to inform experimental design. We applied this framework to screen six ILs ([bmim][PF_6], [bmim][BF_4], [emim][Tf_2N], [bmim][Ac], [hmim][FAP], [hmim][Cl]) and found that [bmim][PF_6] is the ideal entrainer for HFC-32/HFC-125, which comprise the refrigerant R-410a, separations. This workflow can be implemented in minutes to hours to rapidly assess up to hundreds of IL entrainers, if data is available. We emphasize that the proposed framework is flexible and can be easily extended to consider additional thermophysical properties such as density, viscosity, and heat capacity, and other environmentally important systems in need of rapid evaluation techniques, such as CO_2 capture and biomass energy sources (tert-butanol/ethanol/water mixtures).

Using the proposed framework, we gained several insights regarding the search for IL entrainers to facilitate separations of HFC refrigerants for their reuse and recycle. We found that experimental binary HFC/IL solubility measurements taken at multiple temperatures are more valuable than the new ternary HFC/IL mixture measurements conducted at a single temperature. The reason for this is two-fold: a) accurate phase predictions, flash calculations, and ternary mixture predictions can be made using PR EoS models parameterized with binary solubility data; and b) the binary interaction parameters are influenced by temperature, indicating the need for data measured at a range of temperatures. Additionally, we show that binary data

is sufficient to show qualitative results for IL entrainer screening and preliminary process design. Finally, we found that for a given IL, the relative volatility between the two HFCs studied remains relatively constant as the HFC composition within the mixture changes. This implies that that qualitative screening of ILs can be rapidly accomplished via straightforward relative volatility calculations at a single HFC/IL mixture composition. Our results show that these IL screening decisions can be made with up to ten percent error in a given data sets.

Thus, moving forward, we recommend a multistage IL screening approach. First, relative volatility of HFCs in many ILs should be measured at a single composition to facilitate initial IL screening and down-selection. Second, binary HFC/IL data at multiple temperatures should be gathered for the most promising ILs. Third, using this data, thermodynamic and process modeling calculations with uncertainty analysis should be performed. Fourth, for the best IL entrainer separation systems, sparse ternary mixture measurements should be made to validate liquid phase predictions. Thus, for IL screening, emphasis should be placed on gathering a variety of data over experimental accuracy. While not essential for preliminary HFC separation process design and IL entrainer screening, ternary data is useful in the further validation and refinement of predictions made with models parameterized with binary data and can provide additional enrichment of a data set.

We note that our recommendations are pragmatically engineering focused and may be at odds with current practices of gathering full isotherm data for each HFC/IL mixture before considering process scale implications. Hence, this work highlights a possible tension between scientific goals, e.g., understanding mechanisms and publishing full HFC/IL solubility isotherms, and engineering needs. Our intention with these findings is to guide both laboratory and molecular simulation data generation efforts, which have been focusing in recent years more on studying ILs at a single temperature and creating new tools to gather increasingly complex data (e.g., ternary

mixture measurements), by understanding what data are sufficient for molecular and process design decisions. Within this context, there are several outstanding research questions which can be addressed in the future with extensions of our proposed framework: a) Which thermodynamic model is best in terms of fit and simplicity for a given HFC/IL mixture? b) Are alternate parameter temperature dependencies (beyond linear) supported by the data? c) How do properties other than relative volatility and phase equilibrium, such as density, viscosity, and heat capacity, affect the cost of an HFC separation process? d) How does uncertainty impact the optimal flowsheet configuration and detailed process design for each HFC/IL system? More broadly, these open questions are pertinent to practically all green solvent design applications.

CHAPTER 4

MODELING AND OPTIMIZATION OF IONIC LIQUID ENABLED EXTRACTIVE DISTILLATION OF TERNARY AZEOTROPIC MIXTURES

This chapter is based on previously published work:

A. Garciadiego, M. Mazumder, B. J. Befort, and A. W. Dowling. Modeling and optimization of ionic liquid enabled extractive distillation of ternary azeotrope mixtures. In Y. Yamashita and M. Kano editors, *14th International Symposium on Process Systems Engineering* volume 49 of *Computer Aided Chemical Engineering*, pages 307–312. Elsevier, 2022.

4.1 Introduction

Thousands of tons of HFC refrigerant mixtures, commonly used in industrial, commercial, and residential applications, are scheduled for phase-out worldwide under the 2016 Kigali amendment to the Montreal Protocol, the European Union F-Gas regulations (2015)[142], and the American Innovation and Manufacturing (AIM) Act of 2020[49]. The latter directs EPA to phase down production and consumption of HFCs in the US by 85 percent over the next 15 years. Common HFC mixtures such as R-410A (50 %mol R-32, 50 %mol R-125), R-404A (44 %mol R-125, 4 %mol R-134a, 52 %mol R-143a), and R-407C (23 %mol R-32, 25 %mol R-125, 52 %mol R-134a) are targeted for phase-out because of their high global warming potential (GWP): R-410A with 2088 GWP, R-404A with 3922 GWP, and R-407C with 2107 GWP, where CO_2 has a GWP of 1 by definition. However, R-32 and other HFCs have a low GWP and

could be reused as part of global phase-out. R-134a is used in R-450A, offering similar performance but with a lower GWP (547)[69]. Unfortunately, there is no means to easily separate HFC mixtures due to their azeotropic or near azeotropic nature. Without a new economically viable separation process, the phase-out will require all HFCs to be collected and incinerated. Extractive distillation, the most common method for separating azeotropic or close-boiling mixtures, is a promising approach to separate HFC mixtures. Moreover, tailored IL solvents can enable extractive distillation of near-azeotropic HFC mixtures. In 2003, Lei *et al.* [83]. first proposed extractive distillation with ILs as entrainers, and discussed the use of ILs in extractive distillation in detail[84]. ILs have exhibited high capacity as entrainers to separate azeotropic or close-boiling mixtures[113]. ILs can be recycled in separation processes, reducing the material demands and improving the economics[163, 164]. Shiflett and Yokozeki *et al.* [127] proposed extractive distillation to separate fluorinated refrigerant mixtures using ILs.

4.2 Methods

4.2.1 HFC separation process development and modeling

In this work, we design three extractive distillation processes to separate three ternary azeotrope mixtures, R-404A, R-407C, and a mixture of R-410A and R-22 using an IL entrainer. Table 4.1 summarizes these three case studies [55]. We use the Peng-Robison (PENG-ROB) equation of state to calculate thermodynamic properties. We fit the HFC binary interaction parameters similar to Shiflett and Yokozeki [132, 133, 130].

TABLE 4.1

COMPOSITIONS OF HFCS MIXTURES SEPARATED AND IL USED

	R-404A	R-407C	R-410A
HFC	mol/mol	mol/mol	mol/mol
R-32	0.00	0.23	0.45
R-125	0.44	0.25	0.45
R-134a	0.04	0.52	0.00
R-143a	0.52	0.00	0.00
R-22	0.00	0.00	0.10
IL used	[emim][Tf_2N]	[bmim][PF_6]	[bmim][PF_6]
IL (kg/h)	2000	400	750

4.2.2 Sensitivity analysis

We performed single-parameter sensitivity over eight variables. The base case used 20 theoretical stages, a flowrate of IL of 1000 kg/h, IL is feeding in stage 2, and the HFC mixture feeding stage is stage 15, the inlet temperature of 25°C, the pressure of 10 bar, a reboiler temperature of 130°C, and a reboiler ratio of 2.5. We found that the extractive distillation column's pressure and reflux ratio are most important to minimize energy consumption while obtaining 99.5 mol% purity of all HFC products. Through our sensitivity analysis, we look to obtain the desired purity (99.5 mol%) of R-134a in the distillate of the extractive distillation in the presence of [emim][Tf_2N] with moderate energy consumption. We found that it is impossible to reach the required purity without 25 theoretical stages and a flowrate of IL of 2000 kg/h, even though they significantly influence the capital cost. The IL is fed in stage 2, and the HFC mixture is fed in stage 20 at a temperature of 20°C. We selected

a pressure of 7 bar in the column and a reboiler temperature of 90°C to ensure the energy consumption was as low as possible while reaching the purity target. Finally, following the same analysis, we selected a reflux ratio of 3. Aspen equipment sizing tools were used to size the equipment.

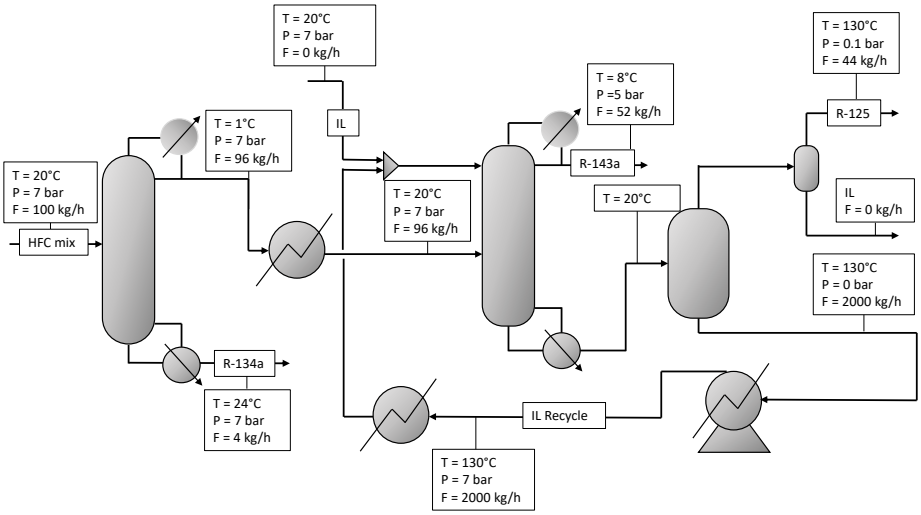

Figure 4.1. Process flow diagram of the developed HFC separation process

4.3 Economic Performance Evaluation

We now analyze the economics of the design HFC separation processes. We evaluate the capital cost, shown in Eq. (4.1), which includes equipment, installation cost, and the price of the IL as expressed in units of M$/y.

$$\text{Capital cost}\left(\frac{\text{M\$}}{\text{y}}\right) = \text{Equipment cost}\left(\frac{\text{M\$}}{\text{y}}\right) + \text{Installation cost}\left(\frac{\text{M\$}}{\text{y}}\right) + \text{IL price}\left(\frac{\text{M\$}}{\text{y}}\right) \tag{4.1}$$

We assume a 20-year (N) plant lifetime and a salvage value of 20 % of the cost of the plant assets (excluding the IL). We assume 24 hours a day workload for 330 days in a year for all calculations. We calculate the annualized capital cost (C_{anm}) using Eq. (4.2), in which CRF is the capital recovery factor, C_{NPC} is the net present cost estimated in AspenPlus. We assume a nominal discount rate ($i\prime$) of 8 % and an expected inflation rate (f) of 3.5 % to calculate the real discount rate (i). With the assumptions above, we calculate a capital recovery factor (CRF) of 0.077 using Eqs. (4.3) and (4.4). We estimate 2,000 kg/h of IL, which corresponds to a column fill of 65 %. We estimate operation costs using AspenPlus V.11 and the following utility costs: electricity (0.07\$/KW), cooling water (120 \$/MMGAL), and high-pressure steam (8.22 \$/Klb).

$$C_{anm} = (CRF) \times (C_{NPC}) \tag{4.2}$$

$$CRF = \frac{i(1+i)^N}{(1+i)^N - 1} \tag{4.3}$$

$$i = \frac{i\prime - f}{1+f} \tag{4.4}$$

As shown in Figure 4.2, the capital and operating costs (\$/kg of HFC feed) of the R-404A, R-407C, and R-410A separation increase as we decrease the mixture feed flow rate. We observe that the significant increase in the capital cost is due to the amount of IL necessary to achieve the 99.5 mol% purity of HFCs desired in the separation. The cost of equipment and installation have minor variations as the size of the equipment is nearly minimum or standard size. As observed in Figure 4.2, the

capital cost may increase to up to 60 % of the total cost. The rise in total capital cost is dependent on the ratio of IL/HFC mixture required for each process. 1 % to 2 % of IL degradation per year corresponds to an increase of the operating cost of 0.03 $/kg to 0.05 $/kg, respectively.

Currently, most ILs are only available in high purity for laboratory-scale experiments at high prices of $1,000/kg. Historically, after an IL is selected for a commercial application and production increases, the price decreases by 90-92 % [128]. In anticipation of a similar economy of scale, we consider five IL price scenarios: 1,000 $/kg, 750 $/kg, 500 $/kg, 250 $/kg, and 100 $/kg. Figure 4.3 shows the impact of IL price on capital costs. Specifically, the capital cost (M$/y) increases linearly with the IL flowrate (kg/h) at a given IL price. As expected, changing the IL price changes the slope of this relationship. Moreover, the capital cost is extremely sensitive to the IL price. For example, at 5000 kg/h IL flowrate, decreasing the IL price from 1000 $/kg (laboratory scale specialty chemical) to 100 $/kg (commercial IL) decreases the capital cost from 8 M$/y to 1.5 M$/y. We reiterate that previous commercialization of ILs suggests a 90 % reduction in IL price is reasonable[128].

$$\begin{aligned} &\text{Added value}\left(\frac{\$}{\text{kg}}\right) = \\ &\underbrace{\text{Sell price low GWP components}\left(\frac{\$}{\text{kg}}\right) - \text{Cost of recovered HFCs}\left(\frac{\$}{\text{kg}}\right)}_{\text{Price diferential}} \\ &\underbrace{- \text{Capital Cost}\left(\frac{\$}{\text{kg}}\right) - \text{Operating cost}\left(\frac{\$}{\text{kg}}\right)}_{\text{Costs}} \end{aligned} \tag{4.5}$$

Next, we propose added value, with units $/kg of HFC feed, as a metric to easily compare different hypothetical scenarios. Eq. (4.5) calculates added value from the price differential and costs. The selling price of low GWP components is the value of the recycled products, and the cost of recovery HFC mixture corresponds

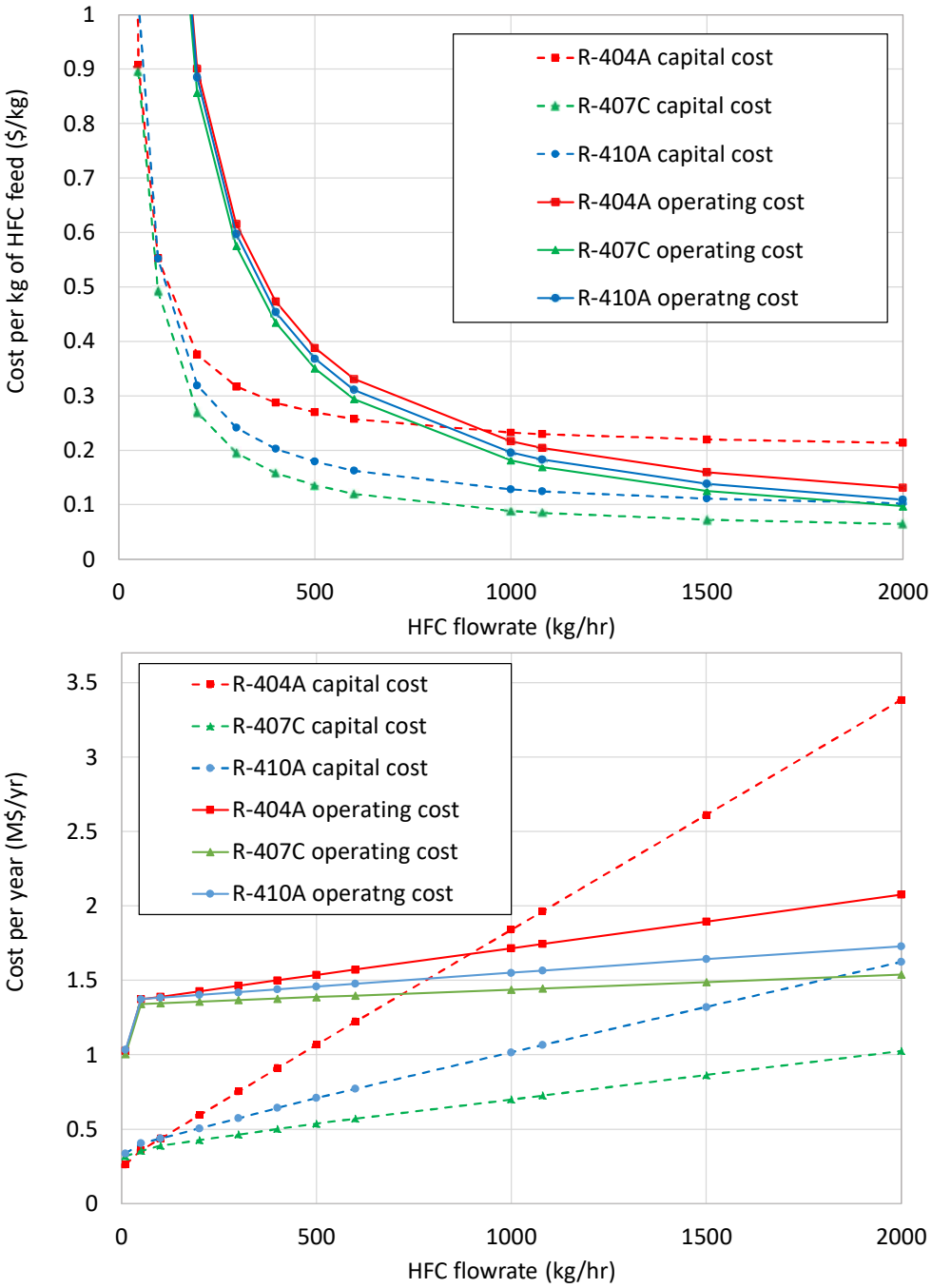

Figure 4.2. Capital and operating cost of the R-404A, R-407C, and R-410A AspenPlus model. The capital cost of the separation process increases rapidly as we increase the inlet flowrate.

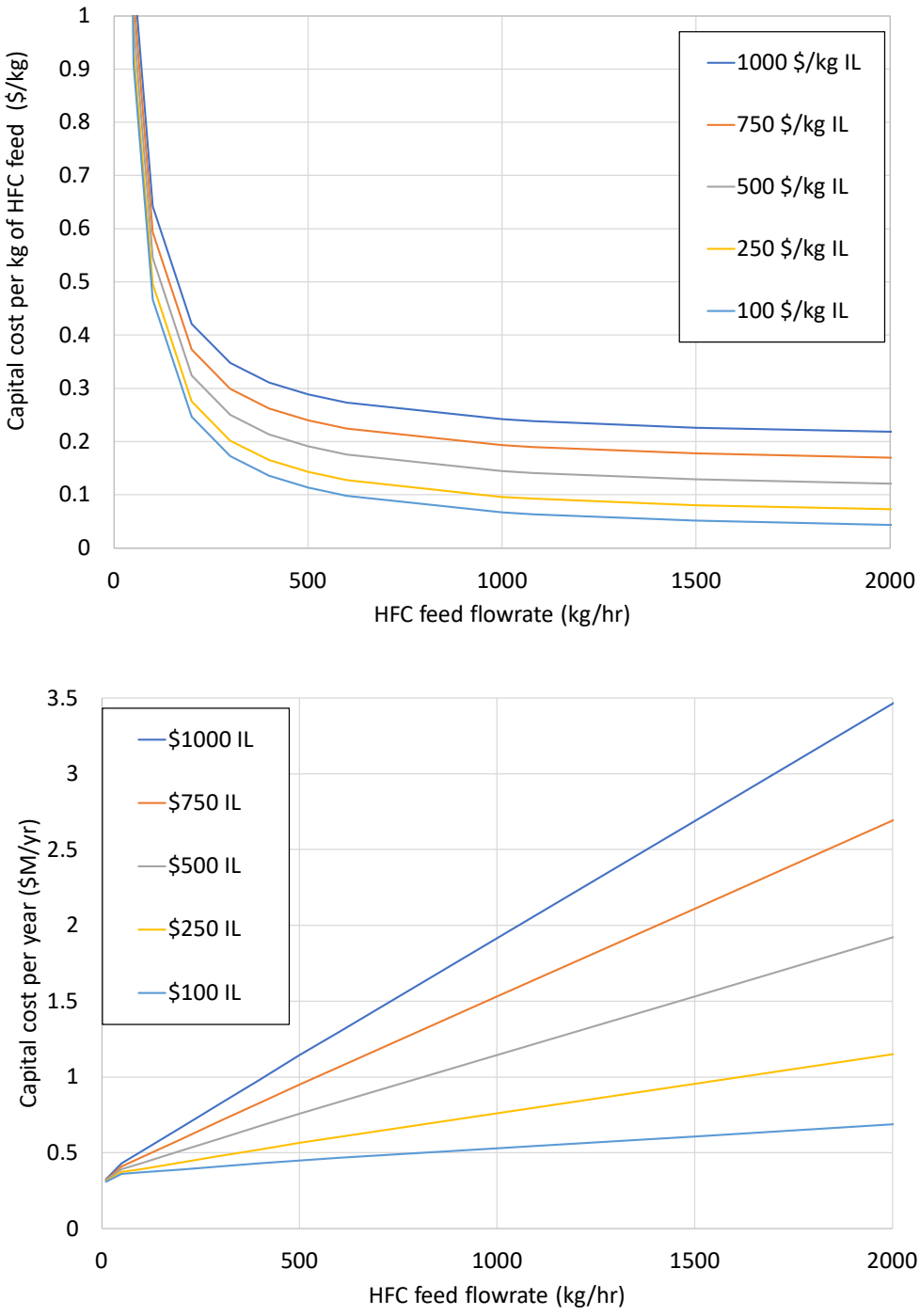

Figure 4.3. Influence of the ionic liquid price in capital cost for the separation of R-404A.

to the value of the used HFC refrigerant mixtures (half of the cost of production and transportation of the HFC mixture used as a base and worst-case scenario). A negative cost of recovery HFC mixture is possible with government subsidies incentivizing HFC recycling (instead of illegal venting). Figure 4.2 reports the operating and capital costs ($/kg) as a function of the HFC feed rate. Similarly, Figure 4.3 shows the dependence of capital cost ($/kg) on IL price. Because the added value metric represents profit per kilogram of HFC processed, it allows quick evaluation of different market scenarios (e.g., HFC and IL prices).

Using values from these plots, the added value metric can quickly evaluate the benefits of new ILs for the separation process; for example, if a new hypothetical IL required 20 % less mass than the analyzed ILs, the cost in Figure 3 can be proportionally reduced. Likewise, if a new hypothetic IL reduces the separation energy requirement by 50 %, the operating cost value used in Eq. (4.5) can be reduced by approximately 50 %. This metric gives valuable insights and enables fast "what if" analyses to guide IL and process design.

Under current market conditions, we found that R-410A separation has an added value of 0.55 to 0.72 $/kg with an IL price of 1000 $/kg and 100 $/kg, respectively. Under a futuristic scenario where phase-outs in production doubles the market price for R-32, the added value of the separation of R-410A could be as high as 5.60 $/kg to 5.78 $/kg with an IL price of 1000 $/kg and 100 $/kg respectively. If the price of R-32 increases by 50 %, the added value would reach 3.08 $/kg. We found that the price of ILs has the most significant impact on the capital cost, and the price differential between the HFC mixture and the pure HFC impacts the added value and the payback period.

4.4 Conclusions

In this paper, we show that separating and recycling HFCs with extractive distillation utilizing ILs is economically attractive, especially under anticipated future scenarios. It is important to note that ILs are viscous, and a rate base model is needed for rigorous design and more accurate technoeconomic analyses. The presented results are based on currently available ILs [bmim][PF_6] and [emim][Tf_2N]. However, ILs can be tailored for specific purposes due to the vast diversity of anions and cations available. For example, tailored ILs with higher selectivity would reduce the amount of IL required and thus capital costs. Tailoring other properties of the ILs, such as the density, viscosity, and thermal capacity could reduce the operating costs of the process. There are also unexplored opportunities to optimize the extractive distillation process. While the one and two-dimensional sensitivity analyses presented here show 25 theoretical stages and the amount of IL necessary for the separation, rigorous optimization may find additional opportunities for improvement by exploiting interactions across multiple design decision variables. Moreover, simultaneous process optimization (e.g., flowrates, temperatures) and heat integration may further reduce the energy intensity of the process by systematically balancing reboiler duty and compression costs (e.g., by changing column pressure).

CHAPTER 5

THESIS CONCLUSIONS AND RECOMMENDED FUTURE WORK

The main contribution of this thesis is to advance multi-scale modeling for solvent design by leveraging our open-source equation-oriented modeling framework to inform molecular design on properties, data, and accuracy necessary to design new tailored solvents for energy-intensive separations. This thesis presents frameworks for information transfer and uncertainty propagation from data to multi-scale process design.

In Chapter 2, through a non-intuitive informed collaboration with Prof. Luo, we found the most influential properties to make DSE an economically competitive technology in desalination. We found solubility and its swing with respect to temperature to be the focus of tailoring ILs to decrease costs and energy intensity. Additionally, we found specific quantitative targets for the properties required.

The framework in Chapter 3 gives pragmatically engineering-focused recommendations on experimental conditions to support rapid material screening for materials design and engineering needs. Chapter 3 intention is to guide laboratory and molecular simulation data generation efforts by understanding what data are sufficient for molecular and process design decisions.

Finally, the added value metric presented in Chapter 4 informs separation processes with little data on a process's economic viability due to lack of data or uncertainty due to changes in prices and regulations. The metric allows to compare the price differential of mixtures and pure products to capital and operations costs and to explore under what future market conditions a process would be profitable.

5.1 Contributions of the Thesis

The main contributions of this thesis are as follows:

- Creation of a technoeconomic framework for property target search for directional solvent extraction
- Creation of a rapid open-source framework for screening new ILs as HFC separation entrainers
- Demonstration of the importance of data selection for entrainer screening
- Demonstration of accuracy necessary for experimental or molecular simulation data for accurate screening selection
- Demonstration of added value metric concerning HFC separations

5.2 Recommendations for Future Work

The frameworks presented in this thesis have the ability and should be expanded in several directions. In both applications, the influence of viscosity is critical, as some ILs can have high viscosity, which is why the framework should be expanded to include Rate-based modeling. Additionally, optimization of properties other than relative volatility and phase equilibrium, such as density and heat capacity.

Ongoing work includes the ability of the framework to systematically select thermodynamic models based on fit and simplicity. The framework's planned expansion includes adding different thermodynamic models, such as activity coefficient models. And as more data become available on the system studied, predictive models should be included to predict ILs as entrainers. Additionally, the frameworks should be paired with model-based design of experiments[148] to maximize information gained from experiments and mathematically improve experimental design conditions. And finally, optimize the collection of simulation and experimental data.

Finally, ongoing work includes expanding the work to other systems. In collaboration with Kanishka Ghosh, a similar framework is utilized for model-form uncertainty

propagation and property target search for catalyst and separation methods for light hydrocarbons conversion.

BIBLIOGRAPHY

1. "HSL. A collection of Fortran codes for large scale scientific computation. http://www.hsl.rl.ac.uk/".

2. World Bank, The Role of Desalination in an Increasingly Water-Scarce World. *World Bank, Washington, DC.* doi: 10.1596/31416.

3. Lack of money to develop solvent extraction desalting plant. *Water Desalination Report*, 6(2), 1970.

4. *Foodchem International Corporation*, Date of Access: 2019. URL `https://foodchem.cn`.

5. *Proionic*, Date of Access: 2019. URL `https://www.proionic.com/bestseller/EMIM-TFSI-electronic-grade.php`.

6. Year 2019 Industrial Firm Power Rates. *Edison Electrical Institute.*, Date of Access: 2020. URL `https://www.consultbai.com/images/stories/publications/maps20_388251.pdf`.

7. C. S. Adjiman, A. Galindo, and G. Jackson. Molecules matter: The expanding envelope of process design. In M. R. Eden, J. D. Siirola, and G. P. Towler, editors, *Proceedings of the 8th International Conference on Foundations of Computer-Aided Process Design*, volume 34 of *Computer Aided Chemical Engineering*, pages 55–64. Elsevier, 2014. doi: 10.1016/B978-0-444-63433-7.50007-9.

8. E. Ahmetović and I. E. Grossmann. Global superstructure optimization for the design of integrated process water networks. *AIChE Journal*, 57(2):434–457, feb 2011. doi: 10.1002/aic.12276.

9. S. Alotaibi, O. Ibrahim, S. Luo, and T. Luo. Modeling of a continuous water desalination process using directional solvent extraction. *Desalination*, 420:114–124, 10 2017. doi: 10.1016/j.desal.2017.07.004.

10. S. Alotaibi, O. Ibrahim, Y. Wang, and T. Luo. Exergy analysis of directional solvent extraction desalination process. *Entropy*, 321:321, 04 2019. doi: 10.3390/e21030321.

11. S. Amaran and N. V. Sahinidis. Global optimization of nonlinear least-squares problems by branch-and-bound and optimality constraints. *TOP*, 20(1):154–172, 2012. doi: 10.1007/s11750-011-0178-8.

12. S. Asensio-Delgado, D. Jovell, G. Zarca, A. Urtiaga, and F. Llovell. Thermodynamic and process modeling of the recovery of R410A compounds with ionic liquids. *International Journal of Refrigeration*, 118:365–375, 2020. doi: 10.1016/j.ijrefrig.2020.04.013.

13. L. Atkinson and L. Bass. Produced Water Report: Regulations, Current Practices, and Research Needs. *Groundwater Protection Council*, 2019. URL `https://www.gwpc.org/sites/gwpc/uploads/documents/Research/Produced_Water_Full_Report___Digital_Use.pdf`.

14. N. D. Austin, N. V. Sahinidis, and D. W. Trahan. Computer-aided molecular design: An introduction and review of tools, applications, and solution techniques. *Chemical Engineering Research and Design*, 116:2–26, 2016. doi: 10.1016/j.cherd.2016.10.014.

15. K. R. Baca, M. G. R. Broom, Darren P., M. J. Benham, and M. B. Shiflett. First measurements for the simultaneous sorption of difluoromethane and pentafluoroethane mixtures in ionic liquids using the integral mass balance method. *Industrial & Engineering Chemistry Research*, 61(27):9774–9784, 2022. doi: 10.1021/acs.iecr.2c00497.

16. K. R. Baca, G. M. Olsen, L. Matamoros Valenciano, M. G. Bennett, D. M. Haggard, B. J. Befort, A. Garciadiego, A. W. Dowling, E. J. Maginn, and M. B. Shiflett. Phase equilibria and diffusivities of HFC-32 and HFC-125 in ionic liquids for the separation of R-410A. *ACS Sustainable Chemistry & Engineering*, 10(2):816–830, 2022. doi: 10.1021/acssuschemeng.1c06252.

17. A. Bajpayee. Directional Solvent Extraction Desalination (PhD thesis). *Massachusetts Institute of Technology (MIT)*, 2012.

18. A. Bajpayee, T. Luo, A. Muto, and G. Chen. Very low temperature membrane-free desalination by directional solvent extraction. *Energy & Environmental Science*, 4:1672–1675, 2011. doi: 10.1039/C1EE01027A.

19. A. Bardow, K. Steur, and J. Gross. Continuous-molecular targeting for integrated solvent and process design. *Industrial & Engineering Chemistry Research*, 49(6):2834–2840, 2010. doi: 10.1021/ie901281w.

20. T. V. Bartholomew and M. S. Mauter. Computational framework for modeling membrane processes without process and solution property simplifications. *Journal of Membrane Science*, 573:682–693, 2019. doi: 10.1016/j.memsci.2018.11.067.

21. T. V. Bartholomew, L. Mey, J. T. Arena, N. S. Siefert, and M. S. Mauter. Osmotically assisted reverse osmosis for high salinity brine treatment. *Desalination*, 421:3–11, 2017. doi: 10.1016/j.desal.2017.04.012.

22. R. Battino and P. Seybold. Solubility correlations. Part 1. *Chemistry & Biodiversity*, 4(11):2547–2554, 2007. doi: 10.1002/cbdv.200790208.

23. J. Bedia, J. Palomar, M. Gonzalez-Miquel, F. Rodriguez, and J. J. Rodriguez. Screening ionic liquids as suitable ammonia absorbents on the basis of thermodynamic and kinetic analysis. *Separation and Purification Technology*, 95: 188–195, 2012. doi: 10.1016/j.seppur.2012.05.006.

24. L. Berg. Azeotropic and extractive distillation: Selecting the agent for distillation. *Chemical Engineering Progress*, 65(9):52–57, 1969.

25. J. Bezanson, A. Edelman, S. Karpinski, and V. B. Shah. Julia: A fresh approach to numerical computing. *SIAM Review*, 59(1):65–98, 2017.

26. L. Biegler, I. Grossmann, and A. Westerberg. *Systematic Methods for Chemical Process Design*. Prentice Hall, 1997. ISBN 9780134924229.

27. M. Bier and S. Dietrich. Vapour pressure of ionic liquids. *Molecular Physics*, 108(2):211–214, 2010. doi: 10.1080/00268971003604609.

28. G. M. Bollas, P. I. Barton, and A. Mitsos. Bilevel optimization formulation for parameter estimation in vapor–liquid(–liquid) phase equilibrium problems. *Chemical Engineering Science*, 64(8):1768–1783, 2009. doi: 10.1016/j.ces.2009.01.003.

29. J. S. Brown. HFOs new, low global warming potential refrigerants. *ASHRAE Journal*, 51(8):22–29, 2009.

30. A. P. Burgard, J. P. Eason, J. C. Eslick, J. H. Ghouse, A. Lee, L. T. Biegler, and D. C. Millerr. A smooth, square flash formulation for equation-oriented flowsheet optimization. In M. Eden, G. Towler, and M. Ierapetritou, editors, *Proceedings of the 13th International Symposium on Process Systems Engineering - PSE 2018*, volume 44 of *Computer Aided Chemical Engineering*, pages 871–876. Elsevier, 2018. doi: 10.1016/B978-0-444-64241-7.50140-3.

31. M. L. Bynum, G. A. Hackebeil, W. E. Hart, C. D. Laird, B. L. Nicholson, J. D. Siirola, J.-P. Watson, and D. L. Woodruff. *Pyomo–optimization modeling in python*, volume 67. Springer Science & Business Media, third edition, 2021. ISBN 978-3-319-58821-6.

32. H. Chao, Z. Song, H. Cheng, L. Chen, and Z. Qi. Computer-aided design and process evaluation of ionic liquids for n-hexane-methylcyclopentane extractive distillation. *Separation and Purification Technology*, 196:157–165, 2018. doi: 10.1016/j.seppur.2017.06.054.

33. N. G. Chemmangattuvalappil, D. K. S. Ng, L. Y. Ng, J. Ooi, J. W. Chong, and M. R. Eden. A review of process systems engineering (PSE) tools for the design of ionic liquids and integrated biorefineries. *Processes*, 8(12), 2020. doi: 10.3390/pr8121678.

34. J. Cho and J. Jeon. Optimization study on the azeotropic distillation process for isopropyl alcohol dehydration. *Korean Journal of Chemical Engineering*, 23: 1–7, 2006. doi: 10.1007/BF02705684.

35. L. M. Chávez-Islas, R. Vasquez-Medrano, and A. Flores-Tlacuahuac. Optimal molecular design of ionic liquids for high-purity bioethanol production. *Industrial & Engineering Chemistry Research*, 50(9):5153–5168, 2011. doi: 10.1021/ie101791t.

36. C. Clerbaux, R. Colin, P. C. Simon, and C. Granier. Infrared cross sections and global warming potentials of 10 alternative hydrohalocarbon. *Journal of Geophysical Research*, 98(D6):10,491–10,497, 1993. doi: /10.1029/93JD00390.

37. A. L. H. Costa, F. P. T. da Silva, and F. L. P. Pessoa. Parameter estimation of thermodynamic models for high-pressure systems employing a stochastic method of global optimization. *Brazilian Journal of Chemical Engineering*, 2000. doi: 10.1590/S0104-66322000000300011.

38. Daikin. 32 reasons why R-32 is the right answer. Date of Access: 04/07/2022. URL `https://www.r32reasons.com/resources`.

39. R. R. Davidson, W. H. Smith, and D. W. Hood. Structure and amine-water solubility in desalination by solvent extraction. *Journal of Chemical & Engineering Data*, 5(4):420–423, 1960. doi: 10.1021/je60008a005.

40. S. E. Davis, S. Hada, R. H. Herring, and M. R. Eden. Characterization based reverse design of ionic liquids. In M. R. Eden, J. D. Siirola, and G. P. Towler, editors, *Proceedings of the 8th International Conference on Foundations of Computer-Aided Process Design*, volume 34 of *Computer Aided Chemical Engineering*, pages 285–290. Elsevier, 2014. doi: 10.1016/B978-0-444-63433-7.50032-8.

41. A. W. Dowling and L. T. Biegler. A framework for efficient large scale equation-oriented flowsheet optimization. *Computers & Chemical Engineering*, 72:3–20, 2015. doi: 10.1016/j.compchemeng.2014.05.013.

42. A. W. Dowling, S. R. R. Vetukuri, and L. T. Biegler. Large-scale optimization strategies for pressure swing adsorption cycle synthesis. *AIChE Journal*, 58(12): 3777–3791, 2012. doi: doi.org/10.1002/aic.13928.

43. A. W. Dowling, C. Balwani, Q. Gao, and L. T. Biegler. Optimization of sub-ambient separation systems with embedded cubic equation of state thermodynamic models and complementarity constraints. *Computers & Chemical Engineering*, 81:323–343, 2015. doi: 10.1016/j.compchemeng.2015.04.038.

44. I. Dunning, J. Huchette, and M. Lubin. JuMP: A modeling language for mathematical optimization. *SIAM Review*, 59(2):295–320, 2017. doi: 10.1137/15M1020575.

45. M. A. Duran and I. E. Grossmann. Simultaneous optimization and heat integration of chemical processes. *AIChE Journal*, 32(1):123–138, 1986. doi: 10.1002/aic.690320114.

46. R. S. El-Emam and I. Dincer. Thermodynamic and thermoeconomic analyses of seawater reverse osmosis desalination plant with energy recovery. *Energy*, 64: 154–163, 2014. doi: 10.1016/j.energy.2013.11.037.

47. M. Elimelech and W. A. Phillip. The future of seawater desalination: Energy, technology, and the environment. *Science*, 333(6043):712–717, 2011. doi: 10.1126/science.1200488.

48. C. B. Ellis. *Fresh water from the ocean for cities, industry, and irrigation*. Ronald Press Co, 1954. ISBN 9780598912572.

49. EPA. Draft regulatory impact analysis for phasing down production and consumption of hydrofluorocarbons HFCs. EPA-HQ-OAR-2021-0044-0046-attachment-2, Date of Access: 04/07/2022. URL `https://www.epa.gov/sites/default/files/2021-05/documents/ria_omb_043021_0.pdf`.

50. EPA. Greenhouse gas inventory data explorer. Date of Access: 04/07/2022. URL `https://cfpub.epa.gov/ghgdata/inventoryexplorer/#allsectors/allsectors/fluorinatedgases/gas/all`.

51. EPA. Phasedown of hydrofluorocarbons: Establishing the allowance allocation and trading program under the american innovation and manufacturing act. Date of Access: 04/07/2022. URL `https://www.epa.gov/climate-hfcs-reduction/final-rule-phasedown-hydrofluorocarbons-establishing-allowance`.

52. EPA. How we use water. Date of Access: 2020. URL `https://www.epa.gov/watersense/how-we-use-water#Daily%20Life`.

53. W. R. Esposito and C. A. Floudas. Parameter estimation in nonlinear algebraic models via global optimization. *Computers & Chemical Engineering*, 22:S213–S220, 1998. doi: 10.1016/S0098-1354(98)00217-8.

54. J. Figueroa, B. H. Lunelli, R. M. Filho, and M. W. Maciel. Improvements on anhydrous ethanol production by extractive distillation using ionic liquid as solvent. *Procedia Engineering*, 42:1016–1026, 2012. doi: 10.1016/j.proeng.2012.07.493.

55. E. A. Finberg and M. B. Shiflett. Process designs for separating R-410A, R-404A, and R-407C using extractive distillation and ionic liquid entrainers. *Industrial & Engineering Chemistry Research*, 60(44):16054–16067, 2021. doi: 10.1021/acs.iecr.1c02891.

56. C. P. Fredlake, J. M. Crosthwaite, D. G. Hert, S. N. V. K. Aki, and J. F. Brennecke. Thermophysical properties of imidazolium-based ionic liquids. *Journal of Chemical & Engineering Data*, 49(4):954–964, 2004. doi: 10.1021/je034261a.

57. R. Gani. Computer-aided methods and tools for chemical product design. *Chemical Engineering Research and Design*, 82(11):1494 – 1504, 2004. doi: 10.1205/cerd.82.11.1494.52032.

58. A. Garciadiego, M. Mazumder, B. J. Befort, and A. W. Dowling. Modeling and optimization of ionic liquid enabled extractive distillation of ternary azeotrope mixtures. In Y. Yamashita and M. Kano, editors, *14th International Symposium on Process Systems Engineering*, volume 49 of *Computer Aided Chemical Engineering*, pages 307–312. Elsevier, 2022.

59. C.-Y. Gau, J. F. Brennecke, and M. A. Stadtherr. Reliable nonlinear parameter estimation in vle modeling. *Fluid Phase Equilibria*, 168(1):1–18, 2000. doi: 10.1016/S0378-3812(99)00332-5.

60. J. Gmehling. Vapor-liquid equilibrium data collection. *Main, Germany: DECHEMA*, chemistry data series: vol. i. Frankfurt, 1977.

61. F. Guinot, H. & Clark. Azeotropic distillation in industry. *Chemical Engineering Research and Design*, 16:189–199, 1938.

62. J. Guo, Z. D. Tucker, Y. Wang, B. L. Ashfeld, and T. Luo. Task-Specific Ionic Liquid Enables Highly Efficient Low Temperature Desalination by Directional Solvent Extraction. *chemrxiv.org*, 2020. doi: 10.26434/chemrxiv.11840025.v1.

63. S. Hada, R. H. Herring, and M. R. Eden. Design of ionic liquids using property clustering and decomposition techniques. In A. Kraslawski and I. Turunen, editors, *23rd European Symposium on Computer Aided Process Engineering*, volume 32 of *Computer Aided Chemical Engineering*, pages 955–960. Elsevier, 2013. doi: 10.1016/B978-0-444-63234-0.50160-3.

64. S. Hajipour and M. A. Satyro. Uncertainty analysis applied to thermodynamic models and process design – 1. pure components. *Fluid Phase Equilibria*, 307 (1):78–94, 2011.

65. S. Hajipour, M. Satyro, and M. Foley. Uncertainty analysis applied to thermodynamic models and process design — 2. binary mixtures. *Fluid Phase Equilibria*, 364:15–30, 2014.

66. J. P. Hallett and T. Welton. Room-temperature ionic liquids: Solvents for synthesis and catalysis. 2. *Chemical Reviews*, 111(5):3508–3576, 2011. doi: 10.1021/cr1003248.

67. X. Han, G. Chen, X. Cui, and Q. Wang. Vapor-liquid equilibrium data for the binary mixture difluoroethane (HFC-32) + pentafluoroethane (HFC-125)

of an alternative refrigerant. *Journal of Chemical & Engineering Data*, 52(6): 2112–2116, 2007. doi: 10.1021/je700011a.

68. W. E. Hart, J.-P. Watson, and D. L. Woodruff. Pyomo: modeling and solving mathematical programs in python. *Mathematical Programming Computation*, 3 (3):219–260, 2011.

69. Honeywell. Honeywell, Solstice® N13 (R-450a). Date of Access: 08/07/2021. URL `https://www.honeywell-refrigerants.com/europe/wp-content/uploads/2015/03/Solstice-N13-TDS-141027-LR-vF.pdf`.

70. S. H. Huang and M. Radosz. Equation of State for Small, Large, Polydisperse, and Associating Molecules. *Industrial and Engineering Chemistry Research*, 29 (11):2284–2294, 1990. doi: 10.1021/ie00107a014.

71. G. C. Johnson. Recovery of potable water from sea and brackish. *U.S. Patent 3,823,000A*, July 09, 1974.

72. E. Jones, M. Qadir, M. van Vliet, V. Smakhtin, and S.-m. Kang. The state of desalination and brine production: A global outlook. *Science of The Total Environment*, 657:1343–1356, 2019. doi: 10.1016/j.scitotenv.2018.12.076.

73. E. Jones, M. Qadir, M. T. van Vliet, V. Smakhtin, and S. mu Kang. The state of desalination and brine production: A global outlook. *Science of The Total Environment*, 657:1343 – 1356, 2019. doi: 10.1016/j.scitotenv.2018.12.076.

74. C. Jork, M. Seiler, Y.-A. Beste, and W. Arlt. Influence of ionic liquids on the phase behavior of aqueous azeotropic systems. *Journal of Chemical & Engineering Data*, 49(4):852–857, 2004. doi: 10.1021/je034183r.

75. N. Kakalis, A. Kakhu, and C. Pantelides. Implementing SAFT-based thermodynamics in process modelling tools. *Proc. 6th International Conf. on Foundations of Computer Aided Process Design, CACHE Publications*, V:537–540, 2004.

76. K. A. Klise, B. L. Nicholson, A. Staid, and D. L. Woodruff. Parmest: Parameter estimation via Pyomo. In S. G. Muñoz, C. D. Laird, and M. J. Realff, editors, *Proceedings of the 9th International Conference on Foundations of Computer-Aided Process Design*, volume 47 of *Computer Aided Chemical Engineering*, pages 41–46. Elsevier, 2019. doi: 10.1016/B978-0-12-818597-1.50007-2.

77. S. Kossack, K. Kraemer, R. Gani, and W. Marquardt. A systematic synthesis framework for extractive distillation processes. *Chemical Engineering Research and Design*, 86(7):781–792, 2008. doi: 10.1016/j.cherd.2008.01.008. ECCE-6.

78. M. Kummu, J. H. Guillaume, H. De Moel, S. Eisner, M. Flörke, M. Porkka, S. Siebert, T. I. Veldkamp, and P. J. Ward. The world's road to water scarcity: Shortage and stress in the 20th century and pathways towards sustainability. *Scientific Reports*, 6(December):1–16, 2016. doi: 10.1038/srep38495.

79. J. Labarta, M. D. M. Olaya, R. Velasco, M. Serrano, and A. Gomis. Correlation of the liquid–liquid equilibrium data for specific ternary systems with one or two partially miscible binary subsystems. *Fluid Phase Equilibria*, 278:9–14, 04 2009. doi: 10.1016/j.fluid.2008.12.002.

80. L. Lazare. The Puraq seawater desalination process. *Desalination*, 42(1):11–16, 1982. doi: 10.1016/S0011-9164(00)88736-6.

81. L. Lazare. The Puraq seawater desalination process - an update. *Desalination*, 85(3):345–360, 1992. doi: 10.1016/0011-9164(92)80016-3.

82. A. Lee, J. H. Ghouse, J. C. Eslick, C. D. Laird, J. D. Siirola, M. A. Zamarripa, D. Gunter, J. H. Shinn, A. W. Dowling, D. Bhattacharyya, L. T. Biegler, A. P. Burgard, and D. C. Miller. The idaes process modeling framework and model library—flexibility for process simulation and optimization. *Journal of Advanced Manufacturing and Processing*, 3(3):e10095, 2021. doi: 10.1002/amp2.10095.

83. Z. Lei, C. Li, and B. Chen. Extractive distillation: A review. *Separation & Purification Reviews*, 32(2):121–213, 2003. doi: 10.1081/SPM-120026627.

84. Z. Lei, B. Chen, and Z. Ding. *Special Distillation Processes*. Elsevier Science, Amsterdam, 2005. doi: 10.1016/B978-044451648-0/50003-3.

85. Z. Lei, C. Dai, and B. Chen. Gas solubility in ionic liquids. *Chemical Reviews*, 114(2):1289–1326, 2014. doi: 10.1021/cr300497a.

86. Q. Li, J. Zhang, Z. Lei, J. Zhu, J. Zhu, and X. Huang. Selection of ionic liquids as entrainers for the separation of ethyl acetate and ethanol. *Industrial & Engineering Chemistry Research*, 48(19):9006–9012, 2009. doi: 10.1021/ie8017127.

87. X. Liu, M. He, N. Lv, X. Qi, and C. Su. Solubilities of R-161 and R-143a in 1-hexyl-3-methylimidazolium bis(trifluoromethylsulfonyl)imide. *Fluid Phase Equilibria*, 388:37–42, 2015. doi: 10.1016/j.fluid.2014.12.026.

88. X. Liu, M. He, N. Lv, X. Qi, and C. Su. Vapor–liquid equilibrium of three hydrofluorocarbons with [hmim][Tf_2N]. *Journal of Chemical & Engineering Data*, 60(5):1354–1361, 2015. doi: 10.1021/je501069b.

89. X. Liu, X. Qi, N. Lv, and M. He. Gaseous absorption of fluorinated ethanes by ionic liquids. *Fluid Phase Equilibria*, 405:1–6, 2015.

90. S. Loutatidou and H. A. Arafat. Techno-economic analysis of med and ro desalination powered by low-enthalpy geothermal energy. *Desalination*, 365:277–292, 2015. doi: 10.1016/j.desal.2015.03.010.

91. S. Luo, J. C. Eng, P. Technol, S. Luo, Y. Pang, and T. Luo. A Continuous Directional Solvent Extraction Desalination Process Realized with the Aid of Electro-coalescence. *Journal of Chemical Engineering*, 9(4):Article 1000392, 2018. doi: 10.4172/2157-7048.1000392.

92. T. Luo, A. Bajpayee, and G. Chen. Directional solvent for membrane-free water desalination—a molecular level study. *Journal of Applied Physics*, 110(5):Article 054905, 2011. doi: 10.1063/1.3627239.

93. R. S. M. Ko, N. Sze, H. Magid, and R. G. Bray. Atmospheric lifetime and global warming potential of HFC-245fa. *Journal of Geophysical Research*, 104 (D7):8173–8181, 1999.

94. K. Marsh, J. Boxall, and R. Lichtenthaler. Room temperature ionic liquids and their mixtures—a review. *Fluid Phase Equilibria*, 219(1):93–98, 2004. doi: 10.1016/j.fluid.2004.02.003. Molecular Thermodynamics and Molecular Simulation.

95. J. J. McKetta. *Unit Operations Handbook*. CRC Press, 1992. ISBN 9780203734643.

96. S. E. McLeese, J. C. Eslick, N. J. Hoffmann, A. M. Scurto, and K. V. Camarda. Design of ionic liquids via computational molecular design. *Computers & Chemical Engineering*, 34(9):1476–1480, 2010. doi: 10.1016/j.compchemeng.2010.02.017.

97. M. M. Mekonnen and A. Y. Hoekstra. Sustainability: Four billion people facing severe water scarcity. *Science Advances*, 2(February):1–7, 2016. doi: 10.1126/sciadv.1500323.

98. J. E. Miller. Review of water resources and desalination technologies, 2003-0800. *Sandia National Laboratories*, (March):1–54, 2003. doi: 10.2172/809106.

99. M. H. Millett G. Morgan. *Uncertainty: A Guide to Dealing with Uncertainty in Quantitative Risk and Policy Analysis*. Cambridge University, Cambridge, U.K., 1990. ISBN 9780521427449.

100. A. Mitsos and P. I. Barton. A dual extremum principle in thermodynamics. *AIChE Journal*, 53(8):2131–2147, 2007. doi: 10.1002/aic.11230.

101. A. Mitsos, G. M. Bollas, and P. I. Barton. Bilevel optimization formulation for parameter estimation in liquid–liquid phase equilibrium problems. *Chemical Engineering Science*, 64(3):548–559, 2009.

102. M. S. Monjur, A. Iftakher, and M. M. F. Hasan. Separation process synthesis for high-gwp refrigerant mixtures: Extractive distillation using ionic liquids. *Industrial & Engineering Chemistry Research*, 61(12):4390–4406, 2022. doi: 10.1021/acs.iecr.2c00136.

103. A. R. C. Morais, A. N. Harders, K. R. Baca, G. M. Olsen, B. J. Befort, A. W. Dowling, E. J. Maginn, and M. B. Shiflett. Phase equilibria, diffusivities, and equation of state modeling of HFC-32 and HFC-125 in imidazolium-based ionic liquids for the separation of R-410A. *Industrial & Engineering Chemistry Research*, 59(40):18222–18235, 2020. doi: 10.1021/acs.iecr.0c02820.

104. K. C. Ng, K. Thu, S. J. Oh, L. Ang, M. W. Shahzad, and A. B. Ismail. Recent developments in thermally-driven seawater desalination: Energy efficiency improvement by hybridization of the med and ad cycles. *Desalination*, 356: 255–270, 2015. doi: 10.1016/j.desal.2014.10.025.

105. L. Y. Ng, F. K. Chong, and N. G. Chemmangattuvalappil. Challenges and opportunities in computer-aided molecular design. *Computers & Chemical Engineering*, 81:115 – 129, 2015. doi: 10.1016/j.compchemeng.2015.03.009.

106. NIST. *National Institute of Standards and Technology*, Date of Access: 2018. URL `https://www.nist.gov`.

107. none. Materials for separation technologies. Energy and emission reduction opportunities. United States: N. p., 2005. Web. doi: 10.2172/1218755.

108. M. B. Oliveira, M. J. Pratas, I. M. Marrucho, A. J. Queimada, and J. A. P. Coutinho. Description of the mutual solubilities of fatty acids and water with the CPA EoS. *AIChE Journal*, 55(6):1604–1613, 2009. doi: 10.1002/aic.11766.

109. J. P. O'Connell and J. M. Haile. Thermodynamics: Fundamentals and Applications, Cambridge University Press, New York, USA, 2005. ISBN 9781139443173.

110. K. Paduszyński, M. Królikowski, M. Zawadzki, and P. Orzeł. Computer-aided molecular design of new task-specific ionic liquids for extractive desulfurization of gasoline. *ACS Sustainable Chemistry & Engineering*, 5(10):9032–9042, 2017. doi: 10.1021/acssuschemeng.7b01932.

111. S. A. Papoulias and I. E. Grossmann. A structural optimization approach in process synthesis -ii: Heat recovery networks. *Computers & Chemical Engineering*, 7(6):707–721, 1983. doi: 10.1016/0098-1354(83)85023-6.

112. D. Peng, J. Zhang, H. Cheng, L. Chen, and Z. Qi. Computer-aided ionic liquid design for separation processes based on group contribution method and cosmosac model. *Chemical Engineering Science*, 159:58–68, 2017. doi: 10.1016/j.ces.2016.05.027.

113. A. Pereiro, J. Araújo, J. Esperança, I. Marrucho, and L. Rebelo. Ionic liquids in separations of azeotropic systems – a review. *The Journal of Chemical Thermodynamics*, 46, 03 2012. doi: 10.1016/j.jct.2011.05.026.

114. H. N. Pham and M. F. Doherty. Design and synthesis of heterogeneous azeotropic distillations—ii. residue curve maps. *Chemical Engineering Science*, 45(7):1837–1843, 1990. doi: 10.1016/0009-2509(90)87059-2.

115. N. V. Plechkova and K. R. Seddon. Applications of ionic liquids in the chemical industry. *Chemical Society Reviews*, 37:123–150, 2008. doi: 10.1039/B006677J.

116. G. J. Prokopakis and W. D. Seider. Feasible specifications in azeotropic distillation. *AIChE Journal*, 29(1):49–60, 1983. doi: https://doi.org/10.1002/aic.690290107.

117. N. J. A. Rahman, N. A. Yunus, and A. A. B. Mustaffa. Ionic liquid solvent design framework for extraction of phytochemicals using microwave-assisted method. *Chemical Engineering Transactions*, 78:577–582, 2020. doi: 10.3303/CET2078097.

118. N. Ramírez-Corona, A. Schramm-Flores, and S. Reyes-Lombardo. Effect of ionic liquids as entrainers on the dynamic behavior of ethanol-water extractive columns. *BMC Chemical Engineering*, 1:23, 2019. doi: 10.1186/s42480-019-0023-7.

119. R. C. Reid. *The properties of gases and liquids*. McGraw-Hill, New York, 4th ed. edition, 1987. ISBN 0-07-05-051799-1.

120. H. Ritchie. Water use and stress. *Our World in Data*, Date of Access: 2020. URL `https://ourworldindata.org/water-use-stress`.

121. I. Rodríguez-Donis, V. Gerbaud, and X. Joulia. Entrainer selection rules for the separation of azeotropic and close-boiling-temperature mixtures by homogeneous batch distillation process. *Industrial & Engineering Chemistry Research*, 40(12):2729–2741, 2001. doi: 10.1021/ie000429z.

122. B. C. Roughton, B. Christian, J. White, K. V. Camarda, and R. Gani. Simultaneous design of ionic liquid entrainers and energy efficient azeotropic separation processes. *Computers & Chemical Engineering*, 42:248–262, 2012. doi: 10.1016/j.compchemeng.2012.02.021. European Symposium of Computer Aided Process Engineering - 21.

123. B. C. Roughton, B. Christian, J. White, K. V. Camarda, and R. Gani. Simultaneous design of ionic liquid entrainers and energy efficient azeotropic separation processes. *Computers & Chemical Engineering*, 42:248 – 262, 2012. doi: 10.1016/j.compchemeng.2012.02.021. European Symposium of Computer Aided Process Engineering - 21.

124. R. M. R. Saeed. Thermal characterization of phase change materials for thermal energy storage. *Masters Theses*, 27521, 2016. URL `https://scholarsmine.mst.edu/masters_theses/7521`.

125. M. Seiler, C. Jork, A. Kavarnou, W. Arlt, and R. Hirsch. Separation of azeotropic mixtures using hyperbranched polymers or ionic liquids. *AIChE Journal*, 50(10):2439–2454, 2004. doi: 10.1002/aic.10249.

126. J. Shakun, P. Clark, and F. He. Global warming preceded by increasing carbon dioxide concentrations during the last deglaciation. *Nature*, 484:49–54, 2012. doi: 10.1038/nature10915.

127. M. Shiflett and A. Yokozeki. Separation of difluoromethane and pentafluoroethane by extractive distillation using ionic liquid. *Chimica Oggi-chemistry Today*, 24:28–30, 2006.

128. M. B. Shiflett, editor. *Commercial Applications of Ionic Liquids*. Springer, 2020. ISBN 978-3-030-35245-5. doi: 10.1007/978-3-030-35245-5.

129. M. B. Shiflett and E. J. Maginn. The solubility of gases in ionic liquids. *AIChE Journal*, 63(11):4722–4737, 2017.

130. M. B. Shiflett and A. Yokozeki. Solubility differences of halocarbon isomers in ionic liquid [emim][Tf_2N]. *Journal of Chemical & Engineering Data*, 52(5): 2007–2015, 2007. doi: 10.1021/je700295e.

131. M. B. Shiflett and A. Yokozeki. Binary vapor–liquid and vapor–liquid–liquid equilibria of hydrofluorocarbons (HFC-125 and HFC-143a) and hydrofluoroethers (HFE-125 and HFE-143a) with ionic liquid [emim][Tf_2N]. *Journal of Chemical & Engineering Data*, 53(2):492–497, 2008. doi: 10.1021/je700588d.

132. M. B. Shiflett, M. A. Harmer, C. P. Junk, and A. Yokozeki. Solubility and diffusivity of 1,1,1,2-tetrafluoroethane in room-temperature ionic liquids. *Fluid Phase Equilibria*, 242(2):220–232, 2006. doi: 10.1016/j.fluid.2006.01.026.

133. M. B. Shiflett, M. A. Harmer, C. P. Junk, and A. Yokozeki. Solubility and diffusivity of difluoromethane in room-temperature ionic liquids. *Journal of Chemical & Engineering Data*, 51(2):483–495, 2006. doi: 10.1021/je050386z.

134. M. B. Shiflett, A. D. Shiflett, and A. Yokozeki. Separation of tetrafluoroethylene and carbon dioxide using ionic liquids. *Separation and Purification Technology*, 79(3):357–364, 2011. doi: 10.1016/j.seppur.2011.03.023.

135. D. S. Sholl and R. P. Lively. Seven chemical separations to change the world. *Nature News*, 532(7600):435, 2016. doi: 10.1038/532435a.

136. C. Snyder. Evolution of global temperature over the past two million years. *Nature*, 538:226–228, 2016. doi: 10.1038/nature19798.

137. Z. Song, C. Zhang, Z. Qi, T. Zhou, and K. Sundmacher. Computer-aided design of ionic liquids as solvents for extractive desulfurization. *AIChE Journal*, 64(3): 1013–1025, 2018. doi: 10.1002/aic.15994.

138. K. S. Spiegler and Y. M. El-Sayed. *A Desalination Primer: Introductory Book for Students and Newcomers to Desalination*. Balaban Desalination Publications, 1994. ISBN 0866890343.

139. K. Thanapalan and V. Dua. Using low-grade heat for solvent extraction based efficient water desalination. In E. Pistikopoulos, M. Georgiadis, and A. Kokossis, editors, *21st European Symposium on Computer Aided Process Engineering*,

volume 29 of *Computer Aided Chemical Engineering*, pages 1703–1707. Elsevier, 2011. doi: /10.1016/B978-0-444-54298-4.50119-7.

140. G. Thiel, E. Tow, L. Banchik, H. W. Chung, and J. Lienhard. Energy consumption in desalinating produced water from shale oil and gas extraction. *Desalination*, 366:94–112, 06 2015. doi: 10.1016/j.desal.2014.12.038.

141. G. Ulrich. *Chemical Engineering Process Design and Economics: A Practical Guide*. ISBN 9780866890342.

142. UN. Amendment to the montreal protocol on substances that deplete the ozone layer. Date of Access: 04/07/2022. URL `https://treaties.un.org/doc/Publication/CN/2016/CN.872.2016-Eng.pdfl`.

143. UNDESA. International Decade for Action "Water for Life" 2005-2015. Date of Access: 2019. URL `https://www.un.org/waterforlifedecade/scarcity.shtml`.

144. V. R. Vasquez and W. B. Whiting. Effect of data type on thermodynamic model parameter estimation: A monte carlo approach. *Industrial & Engineering Chemistry Research*, 37(3):1122–1129, 1998. doi: 10.1021/ie970444c.

145. V. K. Verma and T. Banerjee. Ionic liquids as entrainers for water+ethanol, water+2-propanol, and water+thf systems: A quantum chemical approach. *The Journal of Chemical Thermodynamics*, 42(7):909–919, 2010. doi: 10.1016/j.jct.2010.03.001.

146. N. Voutchkov. Energy use for membrane seawater desalination – current status and trends. *Desalination*, 431:2–14, 2018. doi: 10.1016/j.desal.2017.10.033.

147. A. Wächter and L. T. Biegler. On the Implementation of a Primal-Dual Interior Point Filter Line Search Algorithm for Large-Scale Nonlinear Programming. *Mathematical Programming*, 106(1):25–57, 2007.

148. J. Wang and A. W. Dowling. Pyomo.DOE: An open-source package for model-based design of experiments in python. *AIChE Journal*, page e17813. doi: 10.1002/aic.17813.

149. W. Webb. Industrial alcohol. *Chemical Engineering Research and Design*, 15: 243–252, 1937.

150. H. Weingärtner. Understanding ionic liquids at the molecular level: Facts, problems, and controversies. *Angewandte Chemie International Edition*, 47(4): 654–670, 2008. doi: 10.1002/anie.200604951.

151. D. C. Weis and D. R. MacFarlane. Computer-aided molecular design of ionic liquids: An overview. *Australian Journal of Chemistry*, 65:1478–1486, 2012. doi: 10.1071/CH12344.

152. J. A. Wilson. Chemistry and thermochemistry of selected fatty acids using correlation gas chromatography. *Dissertations*, 236, 2014. URL `https://irl.umsl.edu/dissertation/236`.

153. Y. Xu, D. Zaelke, G. J. M. Velders, and V. Ramanathan. The role of hfcs in mitigating 21st century climate change. *Atmospheric Chemistry and Physics*, 13(12):6083–6089, 2013. doi: 10.5194/acp-13-6083-2013.

154. L. Yang, I. E. Grossmann, and J. Manno. Optimization models for shale gas water management. *AIChE Journal*, 60(October):3490–3501, 2014. doi: 10.1002/aic.14526.

155. L. Yang, R. Salcedo-Diaz, and I. E. Grossmann. Water network optimization with wastewater regeneration models. *Industrial & Engineering Chemistry Research*, 53(45):17680–17695, 2014. doi: 10.1021/ie500978h.

156. H. Yeomans and I. E. Grossmann. A systematic modeling framework of superstructure optimization in process synthesis. *Computers and Chemical Engineering*, 23(6):709–731, 1999. doi: 10.1016/S0098-1354(99)00003-4.

157. A. Yokozeki and M. B. Shiflett. Global phase behaviors of trifluoromethane in ionic liquid [bmim][PF_6]. *AIChE Journal*, 52(11):3952–3957, 2006. doi: 10.1002/aic.11007.

158. A. Yokozeki and M. B. Shiflett. Vapor–liquid equilibria of ammonia+ionic liquid mixtures. *Applied Energy*, 84(12):1258–1273, 2007. doi: 10.1016/j.apenergy.2007.02.005.

159. A. Yokozeki and M. B. Shiflett. Separation of carbon dioxide and sulfur dioxide gases using room-temperature ionic liquid [hmim][Tf_2N]. *Energy & Fuels*, 23 (9):4701–4708, 2009. doi: 10.1021/ef900649c.

160. A. Yokozeki and M. B. Shiflett. Gas solubilities in ionic liquids using a generic van der Waals equation of state. *Journal of Supercritical Fluids*, 55(2):846–851, 2010. doi: 10.1016/j.supflu.2010.09.015.

161. C. Y. Yu and D. W. Arnold. Improved algorithm for obtaining liquid-liquid equilibrium parameters by use of a penalty term. *Industrial & Engineering Chemistry Process Design and Development*, 24(2):494–498, 1985. doi: 10.1021/i200029a045.

162. G. Zarca Lago, I. Ortiz Uribe, and A. M. Urtiaga Mendia. Novel solvents based on thiocyanate ionic liquids doped with copper(I) with enhanced equilibrium selectivity for carbon monoxide separation from light gases. *Separation and Purification Technology*, 196:47–56, 2018.

163. H. Zhao, S. Xia, and P. Ma. Use of ionic liquids as 'green' solvents for extractions. *Journal of Chemical Technology & Biotechnology*, 80(10):1089–1096, 2005. doi: 10.1002/jctb.1333.

164. Y. Zhao, R. Gani, R. M. Afzal, X. Zhang, and S. Zhang. Ionic liquids for absorption and separation of gases: An extensive database and a systematic screening method. *AIChE Journal*, 63(4):1353–1367, 2017. doi: 10.1002/aic.15618.

165. Z. Zhu, Y. Ri, M. Li, H. Jia, Y. Wang, and Y. Wang. Extractive distillation for ethanol dehydration using imidazolium-based ionic liquids as solvents. *Chemical Engineering and Processing - Process Intensification*, 109:190–198, 2016. doi: 10.1016/j.cep.2016.09.009.

166. K. R. Zodrow, Q. Li, R. M. Buono, W. Chen, G. Daigger, L. Dueñas-Osorio, M. Elimelech, X. Huang, G. Jiang, J.-H. Kim, B. E. Logan, D. L. Sedlak, P. Westerhoff, and P. J. J. Alvarez. Advanced materials, technologies, and complex systems analyses: Emerging opportunities to enhance urban water security. *Environmental Science & Technology*, 51(18):10274–10281, 2017. doi: 10.1021/acs.est.7b01679.